National Library of Canada
Bibliothèque nationale du Canada

Canadian Theses Service
Service des thèses canadiennes

Ottawa, Canada
K1A 0N4

NOTICE

The quality of this microform is heavily dependent upon the quality of the original thesis submitted for microfilming. Every effort has been made to ensure the highest quality of reproduction possible.

If pages are missing, contact the university which granted the degree.

Some pages may have indistinct print especially if the original pages were typed with a poor typewriter ribbon or if the university sent us an inferior photocopy.

Reproduction in full or in part of this microform is governed by the Canadian Copyright Act, R.S.C. 1970, c. C-30, and subsequent amendments.

AVIS

La qualité de cette microforme dépend grandement de la qualité de la thèse soumise au microfilmage. Nous avons tout fait pour assurer une qualité supérieure de reproduction.

S'il manque des pages, veuillez communiquer avec l'université qui a conféré le grade.

La qualité d'impression de certaines pages peut laisser à désirer, surtout si les pages originales ont été dactylographiées à l'aide d'un ruban usé ou si l'université nous a fait parvenir une photocopie de qualité inférieure.

La reproduction, même partielle, de cette microforme est soumise à la Loi canadienne sur le droit d'auteur, SRC 1970, c. C-30, et ses amendements subséquents.

NL-339 (r. 88/04) c

Canada

National Library of Canada
Bibliothèque nationale du Canada

Canadian Theses Service
Service des thèses canadiennes

Ottawa Canada
K1A 0N4

The author has granted an irrevocable non-exclusive licence allowing the National Library of Canada to reproduce, loan, distribute or sell copies of his/her thesis by any means and in any form or format, making this thesis available to interested persons.

L'auteur a accordé une licence irrévocable et non exclusive permettant à la Bibliothèque nationale du Canada de reproduire, prêter, distribuer ou vendre des copies de sa thèse de quelque manière et sous quelque forme que ce soit pour mettre des exemplaires de cette thèse à la disposition des personnes intéressées.

The author retains ownership of the copyright in his/her thesis. Neither the thesis nor substantial extracts from it may be printed or otherwise reproduced without his/her permission.

L'auteur conserve la propriété du droit d'auteur qui protège sa thèse. Ni la thèse ni des extraits substantiels de celle-ci ne doivent être imprimés ou autrement reproduits sans son autorisation.

ISBN 0-315-55482-7

Canada

THE UNIVERSITY OF ALBERTA

PULSATILE FLOW ARTIFACTS IN 2DFT NMR IMAGING

BY

AL-KARIM A. DAMJI

A THESIS

SUBMITTED TO THE FACULTY OF GRADUATE STUDIES AND RESEARCH

IN PARTIAL FULFILLMENT OF THE REQUIREMENTS FOR THE DEGREE

OF MASTER OF SCIENCE.

DEPARTMENT OF APPLIED SCIENCES IN MEDICINE.

EDMONTON, ALBERTA

FALL 1989

UNIVERSITY OF ALBERTA

RELEASE FORM

NAME OF AUTHOR: AL-KARIM A. DAMJI

TITLE OF THESIS: PULSATILE FLOW ARTIFACTS IN 2DFT NMR IMAGING

DEGREE: MASTER OF SCIENCE

YEAR THIS DEGREE GRANTED: 1989

Permission is hereby granted to THE UNIVERSITY OF ALBERTA LIBRARY to reproduce single copies of this thesis and to lend or sell such copies for private, scholarly or scientific research purposes only.

The author reserves other publication rights, and neither the thesis nor extensive extracts from it may be printed or otherwise reproduced without the author's written permission.

#103 10624 78th Avenue

Edmonton, Alberta. T6E-1P5

Date: 12th Oct 1989

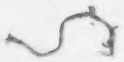

In the name of Allah, most Gracious, most Merciful ...

Proclaim! And thy Lord is most Bountiful,
He who taught the use of the Pen,
Taught man that which he knew not ...

Holy Quran

96:1,4-5

THE UNIVERSITY OF ALBERTA

FACULTY OF GRADUATE STUDIES AND RESEARCH

The undersigned certify that they have read, and recommend to the Faculty of Graduate Studies and Research for acceptance, a thesis entitled PULSATILE FLOW ARTIFACTS IN 2DFT NMR IMAGING submitted by AL-KARIM A. DAMJI in partial fulfillment of the requirements for the degree of MASTER OF SCIENCE.

Richard B. Smyth
(supervisor)

P. S. Allen
(supervisor)

Grant Nelson

D. G. Hughes

Date: 12th Oct 1989

Dedicated with all my love to my family. To my parents, whose sacrifices made this work possible, and to my brother.

ABSTRACT

The presence of motional artifacts in thoracic 2DFT NMR images has hindered the use of NMR imaging in assessing edema and clearance of fluid in the lung. This thesis is concerned with the study of pulsatile flow artifacts in 2DFT NMR images, and development and implementation of techniques to reduce these artifacts.

A simple mathematical model for pulsatile flow was assumed, and the effect of this flow on 2DFT NMR images was evaluated analytically. This analysis suggested the occurrence of four types of image artifacts due to pulsatile flow: ghosting, streaking, blurring and translational artifacts. Pulsatile flow in any direction will lead to ghosting and/or streaking. Additionally, pulsatile flow in a direction parallel to the defined slice will also cause blurring and translational artifacts.

Flow phantom experiments demonstrated ghosting and streaking due to pulsatile flow. In these experiments, it was shown that synchronization of the imaging pulse sequence to pulsatile flow eliminated ghosting and streaking artifacts. The dependence of the translational artifact caused by flow in the read encoding direction on the echo number was also manifested in the results of the flow phantom experiments. Thoracic cross-section images of cats showed ghosting and streaking artifacts due to pulsatile flow in the major blood vessels. Synchronization of the NMR image data acquisition to the diastolic phase of the cardiac cycle minimized the ghosting and streaking artifacts. Blurring and translational artifacts were not a significant factor in the degradation of the thoracic cat images.

Thoracic cat images also showed the presence of a broad low-intensity band of artifactual signal spanning the entire image in the phase-encoding direction. It

was postulated that cardiac and respiratory motions were the major cause of this artifact. It was found that the intensity of this artifact was reduced by either cardiac synchronization (to diastole), or respiratory gating. Despite synchronization and/or gating, a significant level of this low-intensity artifact remained. Imperfect 180° RF pulses were identified as a major cause of this remaining artifact.

ACKNOWLEDGEMENT

I would like to acknowledge and thank Dr. R. E. Snyder and Dr. P. S. Allen for their supervision over the course of this project. Dr. Snyder's advice during the course of this work and the preparation of this manuscript has been very helpful. His questions have often induced me to a better understanding of scientific methodology and NMR. Dr. Allen's excellent teaching and the opportunity he provided me to work in his laboratory, has greatly increased my understanding and appreciation of NMR.

The success of this work has been, in part, due to the assistance of several people who deserve acknowledgement: Dan Doran for his help with all aspects of the in-vivo animal facility, David Ellinger for his assistance with the RF interference problem and the design of the respiratory gating system, Narc Ouellette for his aid in technical problems, Ivy Ho for her image processing software, and Bob Morse for support in all manner of problems.

I would also like to recognize Raman Paranjape of his invaluable friendship and advice in all matters, great and small. From outside the department, three friends from whom I have learned many valuable lessons deserve mention: Fatima Keshavjee, Farzana Nathoo and Ashifa Makhani. I am fortunate to count them among my friends. Heartfelt thanks are expressed to the H. Sachedina and A. Jaffer families for opening their homes to me and making me feel like one of their own. My social and academic life has been greatly enhanced by people like Dr. Laird Trimble, Ravi Menon, Marg Rusinko and others in the in-vivo NMR group and the Department of Applied Sciences in Medicine, who are too numerous to mention individually.

Lastly I would like to acknowledge the Department of Applied Sciences in Medicine for a Research Assistantship during a portion of may stay.

TABLE OF CONTENTS

Chapter			Page
1	Introduction		1
2	NMR and NMR Imaging Basics		5
	2.1 Introduction		5
	2.2 Simple Nuclear Magnetic Resonance Theory		5
	2.3 Rotating Frame of Reference		8
	2.4 Interaction Between Magnetization and an RF Magnetic Field		9
	2.5 Relaxation Phenomena		11
		2.5.1 Longitudinal Relaxation	11
		2.5.2 Transverse Relaxation	12
		2.5.3 Two-site Rapid Exchange Model	13
	2.6 Spin Echoes		14
	2.7 Slice Definition		16
	2.8 Two-Dimensional Fourier Transform NMR Imaging		18
3	Theoretical Analysis of Pulsatile Motion Artifacts in NMR Imaging		23
	3.1 Introduction		23
	3.2 Pulsatile Flow Artifacts in 2DFT NMR Imaging		25
		3.2.1 First Echo Images	26
		3.2.1.1 Pulsatile Flow Normal to the Slice	28
		3.2.1.2 Pulsatile Flow Along the Phase-Encoding Direction	31
		3.2.1.3 Pulsatile Flow Along the Read-Encoding Direction	34
		3.2.2 Higher-Echo Images	36

3.2.2.1 Stationary Spins 37
3.2.2.2 Pulsatile Flow Normal to the Slice 39
3.2.2.3 Pulsatile Flow Along the Phase-Encoding Direction 41
3.2.2.4 Pulsatile Flow Along the Read-Encoding Direction 42
3.3 Suppression of Pulsatile Flow Artifacts 44
4 Cardiac Synchronization and Respiratory Gating Systems 49
4.1 Introduction 49
4.2 Respiratory Gating System 50
4.3 ECG Synchronization System 54
4.4 Combined Cardiac Synchronization and Respiratory GatingSystem 55
5 Experimental Results and Discussion 62
5.1 Introduction 62
5.2 Image Acquisition and Reconstruction 62
5.3 Phantom Study 63
5.3.1 Experimental Design and Procedure 66
5.3.2 Phantom-Study Results and Discussion 68
5.4 Animal Study 81
5.4.1 Experimental Procedure 81
5.4.2 Animal-Study Results and Discussion 82
5.5 Additional Causes of the Residual Artifacts 97
5.5.1 Imperfect 180° RF Pulses 97
5.5.2 Variable Cardiac Period 101
6 Conclusions 106
References 111

LIST OF TABLES

Table		Page
3.1	Timing parameter values for imaging pulse sequence shown in Fig 3.1	25
5.1	Calculated and Measured Positions of Ghost Structures in the Flow Phantom Images	76

LIST OF FIGURES

Figure		Page
2.1	Precession of Spins About $\mathbf{B}_0$	7
2.2	Effect of $\mathbf{B}_1$ Magnetic Field	
	A) Tipping of the Magnetization Vector by an On-Resonance 90° RF Pulse	10
	B) Precession of Transverse Magnetization in the Laboratory Frame	10
2.3	Formation of an Echo	
	A) Generation of Transverse Magnetization by a 90° Pulse	15
	B) Dephasing of Transverse Magnetization	15
	C) Phase Reversal due to 180° RF Pulse	15
	D) Rephasing of Transverse Magnetization	15
	E) Complete Refocussing of Transverse Magnetization	15
2.4	Offset Field due to a Linear Magnetic Field Gradient	17
2.5	A Simple 2DFT Spin-echo NMR Imaging Pulse Sequence	19
3.1	The 2DFT Spin-echo NMR Imaging Pulse Sequence Used to Acquire Images	24
3.2	Images of an Elemental Volume of Spins	
	A) Stationary Spins	31
	B) Spins Flowing Steadily Normal to the Slice	31
	C) Spins Experiencing Pulsatile Flow Normal to the Slice	31
3.3	Images of an Elemental Volume of Spins	
	A) Stationary Spins	33
	B) Spins Flowing Steadily in the Phase Encoding Direction	33
	C) Spins Experiencing Pulsatile Flow in the Phase	

		Encoding Direction	33
3.4	Images of an Elemental Volume of Spins		
	A)	Stationary Spins	36
	B)	Spins Flowing Steadily in the Read Encoding Direction	36
	C)	Spins Experiencing Pulsatile Flow in the Read Encoding Direction	36
3.5	Images of an Elemental Volume of Spins		
	A)	Spins are Stationary	48
	B)	Synchronized Image of Spins Flowing Normal to the Slice	48
	C)	Unsynchronized Image of Spins Flowing Normal to the Slice	48
	D)	Synchronized Image of Spins Flowing in the Phase Encoding Direction	48
	E)	Unsynchronized Image of Spins Flowing in the Phase Encoding Direction	48
	F)	Synchronized Image of Spins Flowing in the Read Encoding Direction	48
	G)	Unsynchronized Image of Spins Flowing in the Read Encoding Direction	48
4.1	Respiratory Gating System Block Diagram		51
4.2	Respiratory Gating System		
	A)	Respiratory Transmitter Unit Circuit Diagram	52
	B)	Respiratory Receiver Unit Circuit Diagram	53
4.3	ECG Synchronization System Block Diagram		56
4.4	ECG Synchronization System		
	A)	ECG Transmitter Unit Circuit Diagram	57
	B)	ECG Receiver Unit Circuit Diagram	58

4.5	Synchronization/Gating System Block Diagram		60
4.6	Multiplexer Unit Circuit Diagram		60
4.7	Flow Diagram for Synchronized/Gated NMR Images		61
5.1	Flow Phantom Illustration		67
5.2	Illustration of Flow Experiment Setup		68
5.3	Flow Phantom Images with Pulsatile Flow		
	A)	1st-echo Unsynchronized Image with z Direction Flow	69
	B)	1st-echo Synchronized Image with z Direction Flow	69
	C)	4th-echo Unsynchronized Image with z Direction Flow	70
	D)	4th-echo Synchronized Image with z Direction Flow	70
	E)	1st-echo Unsynchronized Image with y-z Direction Flow	71
	F)	1st-echo Synchronized Image with y-z Direction Flow	71
	G)	4th-echo Unsynchronized Image with y-z Direction Flow	72
	H)	4th-echo Synchronized Image with y-z Direction Flow	72
	I)	1st-echo Unsynchronized Image with x-z Direction Flow	73
	J)	1st-echo Synchronized Image with x-z Direction Flow	73
	K)	4th-echo Unsynchronized Image with x-z Direction Flow	74
	L)	4th-echo Synchronized Image with x-z Direction Flow	74
5.4	Illustration of Increasing $\hat{x}$ Effect with Echo Number		80
5.5	1st-echo Thoracic Images of a Cat		
	A)	Unsynchronized Image	84
	B)	Synchronized Image with ECG Delay = 1 μs	84
	C)	Synchronized Image with ECG Delay = 20 ms	85
	D)	Synchronized Image with ECG Delay = 60 ms	85
	E)	Synchronized Image with ECG Delay = 120 ms	86
	F)	Synchronized Image with ECG Delay = 180 ms	86
	G)	Synchronized Image with ECG Delay = 250 ms	87

H) Sketch of Major Anatomical Structures in Thoracic Cat Images 87

I) Illustration of Cardiac Cycle Phase for Above Synchronized Images 88

5.6 Background Noise and Artifactual Signal in the Unsynchronized and Synchronized Images 90

5.7 2nd-echo Thoracic Images of a Cat

A) Unsynchronized Image 91

B) Synchronized Image with ECG Delay = 250 ms 91

5.8 Background Noise and Artifactual Signal as a Function of Echo Number in a Synchronized Image Set 92

5.9 Thoracic Images of a Cat

A) 1st echo Synchronized Image with ECG Delay = 1 μs 94

B) 1st echo Synchronized/Gated Image with ECG Delay = 1 μs 94

C) 2nd echo Synchronized Image with ECG Delay = 1 μs 95

D) 2nd echo Synchronized/Gated Image with ECG Delay = 1 μs 95

5.10 Comparison of Background Noise and Artifactual Signal Levels in Synchronized and Synchronized/Gated Image Sets 96

5.11 Thoracic Images of Cats

A) Unsynchronized 1st-echo Image with 90° Selective Pulse 98

B) Unsynchronized 2nd-echo Image with 90° Selective Pulse 98

C) Unsynchronized 1st-echo Image with 0° Selective Pulse 99

D) Unsynchronized 2nd-echo Image with 0° Selective Pulse 99

5.12 Comparison of Background Noise and Artifactual Signal Levels in 90° and 0° Excitation Pulse Image Sets 101

5.13 Effect of Variable t_r on Images

A) Constant t_r Image 104

B) Variable t_r Image 104

LIST OF SYMBOLS AND ABBREVIATIONS

A_X, A_Y, A_Z	Amplitude of the sinusoidal component of the pulsatile flow velocity.
$\mathbf{B}_{eff}$, $\mathbf{B}_e$	Effective magnetic field in the rotating frame.
b_r	Offset field due to linear magnetic field gradient.
$\mathbf{B}_0$	Static magnetic field.
$\mathbf{B}_1$	Radio frequency magnetic field.
ΔB	Static magnetic field inhomogeneity.
CPMG	Carr Purcell Meiboom Gill RF pulse sequence.
E_m	Spin energy state.
E_β	Upper energy state of a proton.
E_α	Lower energy state of a proton.
ECG	Electrocardiogram.
EM	Electromagnetic.
ΔE	Separation between the two proton energy states.
F	Fourier transform operator.
FET	Field-effect transistor.
FID	Free induction decay.
FT	Fourier transform.
F/O	Fiber optic.
F/V	Frequency to voltage.
G_X, G_Y, G_Z, G	Linear magnetic field gradients.

ΔG	Increment of the phase gradient strength.
h	Planck's constant.
I	Spin angular momentum operator.
I	Spin quantum number.
J_p	pth order Bessel function of the first kind.
k	Boltzmann's constant.
L_Y	Image field-of-view in the phase encoding direction.
m	Magnetic quantum number. Magnetization of a voxel.
M	Net magnetization vector.
M_0	Thermal equilibrium value of Longitudinal magnetization.
M_X, M_Y, M_{XY}	Transverse magnetization.
M_Z	Longitudinal magnetization.
N_β	Proton population in upper energy state.
N_α	Proton population in lower energy state.
P_B	Fraction of cellular water bound to macromolecules.
QPSD	Quadrature phase sensitive detection.
s	Complex NMR image signal.
SR	Set-reset.
S/N	Signal to noise ratio.

T	Absolute temperature. Experimentally observed relaxation time. Period of sinusoidal component of the pulsatile flow.
T_B	Relaxation time constant of the bound cellular water.
T_E	Echo time.
T_F	Relaxation time of the free cellular water.
T_p	pth order Chebyshev polynomial.
TTL	Transistor transistor logic.
T_1	Longitudinal relaxation time constant.
T_2	Inherent transverse relaxation time constant.
T_2^*	Transverse relaxation time constant which includes the effects of magnetic field inhomogeneities.
t, t', $\hat{t}$	Time variables.
t_r	Repetition time.
tw	Duration of an RF pulse.
Δt	Sampling interval
u(t)	Real channel of the NMR signal.
v(t)	Imaginary channel of the NMR signal.
x,y,z	Cartesian spatial coordinates.
V_X, V_Y, V_Z	Average velocity of pulsatile flow velocity.
γ	Gyromagnetic ratio.
δ	Delta function.

θ	Tip angle. Phase angle.
μ	Nuclear magnetic moment.
ν_0, ω_0	Larmor frequency.
ϕ	Phase angle.
$\boldsymbol{\Omega}$	Frequency and direction of rotating frame rotation.
Ω	Frequency of sinusoidal component of pulsatile flow velocity.
ω	Frequency of RF radiation.
ω_X, ω_Y	Spatial frequencies.
2DFT	Two dimensional Fourier transform.

CHAPTER 1
INTRODUCTION

Lauterbur, and Mansfield & Grannell published the first nuclear magnetic resonance (NMR) images in 1973. Clinical images were beginning to appear in the literature (Hinshaw et al., 1977,1978; Mansfield et al., 1978) by 1978. Several imaging techniques have emerged during the development of NMR imaging, and today the two-dimensional Fourier transform (2DFT) technique (Kumar et al., 1975; Edelstein et al., 1980) is ubiquitous. The complicated nature of 2DFT NMR imaging provides ample opportunity for artifacts to occur in these images. There are many causes which lead to such artifacts, the most common of which have been identified by Henkelman & Bronskill (1987) in their review of artifacts in NMR imaging.

It has been shown (Schultz et al., 1984; Wood & Henkelman, 1985) that motion during 2DFT NMR imaging results in images in which signal is incorrectly assigned in the phase-encoding direction. Periodic motion leads to the moving structure being repeated discretely, as ghosts in the phase encoding direction. Aperiodic motion results in images with the moving structure streaked in the phase encoding direction. In 2DFT NMR imaging, motion causes artifacts via two distinct mechanisms: a) motion between projections leads to differences in the transverse magnetization distribution generated during each projection (or view) of the imaging experiment which, in turn, results in ghosting or streaking artifacts in the phase-encoding direction, and b) motion during projections causes the transverse magnetization of moving spins to acquire a phase different from that of stationary spins. If this motion differs for each projection, then the phase accumulated by the moving magnetization during each projection will also vary. These inconsistencies in the phase of the moving magnetization also lead to ghosting and streaking artifacts in the phase-encoding direction.

In the thoracic region of the body, motion that contributes to the degradation of NMR images can be separated into three categories: respiratory motion, cardiac motion, and pulsatile blood flow. Of these three categories, artifacts due to respiratory motion and means of suppressing these artifacts have received the most attention in the literature.

The most direct way of dealing with respiratory motion is to restrict NMR data acquisition to occur only in the quiescent portion of the respiratory cycle (Lewis et al., 1986). An image acquired in this manner is said to be respiratory gated. Wood & Henkelman (1986a) suggest that respiratory gating is the most effective means of removing respiratory motion artifacts, although the imaging time may be lengthened by a factor of two to four (Haacke & Patrick, 1986) compared to ungated images. An alternative method of reducing respiratory motion artifacts is to alter the temporal sequence in which the projections are acquired (Bailes et al., 1985; Haacke & Patrick, 1986). By randomizing this sequence, the periodicity of the motion is destroyed, and ghosting is eliminated. However, the streaking artifacts remain. The extent of these artifacts can be limited by utilizing the respiratory waveform to reorder the sequence in which the projections are executed (Wood & Henkelman, 1986a). Although these reordering techniques increase the imaging time only marginally, difficulties arising in the practical implementation of these schemes have prevented their widespread use (Runge and Wood, 1988).

It was realized early in cardiac NMR imaging that acquisition of the NMR data would have to be synchronized to the cardiac cycle (Hawkes et al., 1981; Lanzer et al., 1984; Van Dijk, 1984a,b) in order to reduce cardiac motion and pulsatile blood flow artifacts. Cardiac synchronization permits the data from each projection to be acquired during a given phase of the cardiac cycle. The resulting consistency of motion minimizes the ghosting and streaking artifacts due to cardiac motion and pulsatile blood flow.

More recently, gradient-moment nulling methods of reducing motion artifacts have been proposed. In these schemes (Joseph et al., 1987; Pattany et al., 1987), gradient pulses are used to null the excess phase accumulation due to the velocity, acceleration, and higher-order terms of the moving magnetization. These gradient pulses are designed to leave the phase of the spatially static spins unaffected. A major drawback of these schemes is that the minimum echo time (T_E) is increased drastically (Joseph et al., 1987). It is therefore not feasible to use these schemes to measure the transverse relaxation times of short-T_2 tissue. Also, the use of numerous gradient pulses may compromise the accuracy of T_2 measurements obtained from images utilizing these gradient-moment nulling techniques.

Physiological motion in the thorax and its detrimental effect on images has contributed to the slowing of development of NMR imaging in this region of the body. The effectiveness of NMR imaging in quantitatively evaluating lung edema and clearance of fluid from the lung is being evaluated at the medium-bore animal unit of the University of Alberta in-vivo NMR facility. Previous work on this project (Phillips, 1987) has shown that artifacts in thoracic images of cats compromise the reliability of quantitative relaxation measurements of lung tissue obtained from these images. This work utilized respiratory gating of NMR data acquisition to reduce respiratory motion artifacts. Also, it was suggested that cardiac synchronization of the NMR data would alleviate the artifacts caused by cardiac motion and pulsatile blood flow.

In order to satisfy the objectives of the pulmonary imaging project mentioned above, it is necessary to eliminate artifacts caused by pulsatile blood flow. Therefore, the objective of this thesis is to understand the manner in which pulsatile blood flow leads to artifacts in NMR images and to devise a scheme by which these artifacts are minimized. Toward this end, Chapter 2 discusses the basics of NMR and 2DFT NMR imaging. A simple

mathematical model for pulsatile flow is presented in Chapter 3, where the effect of this flow on 2DFT NMR images is evaluated analytically. The ability to cardiac synchronize and/or respiratory gate NMR image data was developed for the medium-bore animal unit. Chapter 4 details the hardware constructed to allow for cardiac synchronization and/or respiratory gating. Chapter 5 describes flow phantom experiments conducted to demonstrate some of the artifacts predicted in Chapter 3, and to evaluate the efficacy of cardiac synchronization and respiratory gating at reducing artifacts in thoracic images of cats. Two other factors, unrelated to motion, were also shown to contribute to the artifacts present in the thoracic images of cats. Finally, conclusions based on the results of the experiments are presented in Chapter 6.

CHAPTER 2

NMR AND NMR IMAGING BASICS

2.1 Introduction

A prerequisite to understanding the causes and remedies of motional artifacts in Fourier transform (FT) nuclear magnetic resonance imaging is a functional knowledge of the NMR phenomenon and FT NMR imaging. The contents of this chapter are intended to provide a simple summary of the above topics. Detailed treatments of the NMR phenomenon may be found in Abragam (1961), Slichter (1963), and Farrar & Becker (1971). Thorough treatments of NMR imaging are given by Mansfield & Morris (1982) and Morris (1986).

2.2 Simple Nuclear Magnetic Resonance Theory

Nuclear magnetic resonance is only possible with nuclei that possess a net angular momentum. The quantum mechanical relation between the magnetic moment μ and the spin angular momentum $\mathbf{I}h/2\pi$ of a nucleus, where h is Planck's constant and $\mathbf{I}$ identifies the spin angular momentum operator, is written (Slichter, 1963 p2)

$$\mu = \gamma \mathbf{I} \frac{h}{2\pi} \tag{2.1}$$

where the proportionality constant γ is called the gyromagnetic ratio. The spin quantum number I can assume integer or half-integer values. When such nuclei are allowed to equilibrate in a static magnetic field $\mathbf{B}_0 = B_0\mathbf{k}$, the nuclei can be found in the stationary energy states E corresponding to (Slichter, 1963 p2)

$$E_m = -\mu \cdot \mathbf{B}_0 = -\gamma m \frac{h}{2\pi} B_0 \; ; \; m = I, I-1, \ldots -I \tag{2.2}$$

where m is known as the magnetic quantum number. Restricting ourselves to protons, which are spin-half (I = 1/2) nuclei, results in two energy states, an upper and lower denoted by E_β and E_α, respectively. The energy separation (ΔE) between these two states is

$$\Delta E = E_\beta - E_\alpha = \gamma\frac{h}{2\pi}B_0 . \qquad (2.3)$$

The most efficient exchange of energy between the spins and an electromagnetic (EM) field might be expected to require EM radiation whose photon energy ($h\nu_0$) equals the energy separation of the two states. This is indeed the case and leads to the proportionality between the resonance (Larmor) frequency ω_0 and the applied magnetic field B_0, as described by the equations below:

$$h\nu_0 = \Delta E = \gamma\frac{h}{2\pi}B_0$$

$$\omega_0 = \gamma B_0. \qquad (2.4)$$

The equations of motion of the spin angular momentum operator **I** are of exactly the same form as the classical equations describing the interaction of a magnetic moment with an applied magnetic field (Abragam, 1961 p22). For the sake of simplicity, the resultant magnetization vector of free spins will be treated as a classical magnetic moment. Accordingly, the rate of change of angular momentum can be equated to the torque experienced by a magnetic moment residing in a static magnetic field, giving

$$\frac{d}{dt}(\mathbf{I}\frac{h}{2\pi}) = \boldsymbol{\mu} \times \mathbf{B}_0. \qquad (2.5A)$$

Substituting equation 2.1 into the above equation and rearranging gives

$$\frac{d}{dt}(\boldsymbol{\mu}) = \boldsymbol{\mu} \times (\gamma \mathbf{B}_0) \qquad (2.5B)$$

which describes the precessional motion of μ about the static field $\mathbf{B}_0$ at the angular frequency $\omega_0 = \gamma B_0$, i.e., the Larmor frequency. The z-component of the spin magnetic moments may be interpreted as being either parallel or antiparallel to $\mathbf{B}_0$, corresponding to the low and high energy states (see Fig. 2.1). Regardless of a spin's orientation, it will precess about the static magnetic field at the Larmor frequency.

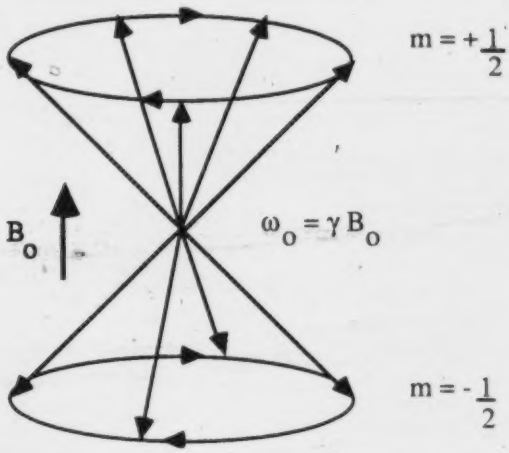

Figure 2.1 Precession of spins in the main magnetic field $\mathbf{B}_0$.

At any temperature above absolute zero the thermal equilibrium population of spins in the upper (N_β) and lower (N_α) states is governed by Maxwell-Boltzmann statistics. The Boltzmann relation translates to a larger population of spins aligned with the applied field (low energy state) compared to the population opposing this field (high energy state). The ratio of these populations may be written (Slichter, 1963 p4) as

$$\frac{N_\alpha}{N_\beta} = \exp\left(\frac{\Delta E}{kT}\right) \tag{2.6}$$

where k represents Boltzmann's constant and T is the absolute temperature. The net magnetization $\mathbf{M}$ of a collection of free spins, defined as

$$\mathbf{M} = \sum_i \mu_i \tag{2.7}$$

per unit volume, has at thermal equilibrium a small z component (M_0) proportional to the difference between the above two populations.

2.3 Rotating Frame of Reference

Before proceeding to examine the behavior of magnetization in the presence of static and radio frequency (RF) magnetic fields, it would be advantageous to see how the equations describing the motion of spins are altered in a frame of reference rotating about the static field in the same sense as the precessing spins. The precessional motion of **M** in such a reference frame is greatly simplified compared with that in the laboratory frame, thus allowing for a better understanding of the magnetization's behavior. To describe the behavior of **M**, equations 2.5B and 2.7 are combined to yield in the laboratory frame,

$$\frac{d\mathbf{M}}{dt} = \mathbf{M} \times \gamma \mathbf{B}_0. \tag{2.8}$$

Allowing $\partial\mathbf{M}/\partial t$ to represent the time derivative of **M** in the rotating frame, the motion of **M** in the laboratory reference frame may be expressed in terms of components in the rotating frame as:

$$\frac{d\mathbf{M}}{dt} = \frac{\partial M_X}{\partial t}\mathbf{i}_\rho + \frac{\partial M_Y}{\partial t}\mathbf{j}_\rho + \frac{\partial M_Z}{\partial t}\mathbf{k}_\rho + M_X\frac{\partial \mathbf{i}_\rho}{\partial t} + M_Y\frac{\partial \mathbf{j}_\rho}{\partial t} + M_Z\frac{\partial \mathbf{k}_\rho}{\partial t} \tag{2.9}$$

where $\mathbf{i}_\rho$, $\mathbf{j}_\rho$ and $\mathbf{k}_\rho$ are the Cartesian unit vectors of the rotating frame. The rotation of these unit vectors is mathematically described by

$$\frac{\partial \mathbf{i}_\rho}{\partial t} = \boldsymbol{\Omega} \times \mathbf{i}_\rho \; ; \qquad \frac{\partial \mathbf{j}_\rho}{\partial t} = \boldsymbol{\Omega} \times \mathbf{j}_\rho \; ; \qquad \frac{\partial \mathbf{k}_\rho}{\partial t} = \boldsymbol{\Omega} \times \mathbf{k}_\rho \; ; \tag{2.10}$$

with $\boldsymbol{\Omega}$ representing both the direction and magnitude of this rotation. Substitution of the above equation into equation 2.9 allows the latter to be reduced to

$$\frac{d\mathbf{M}}{dt} = \frac{\partial \mathbf{M}}{\partial t} + \boldsymbol{\Omega} \times \mathbf{M}. \tag{2.11}$$

Equating equations 2.8 and 2.11 gives

$$\frac{\partial \mathbf{M}}{\partial t} = \mathbf{M} \times \gamma \mathbf{B}_{eff} \tag{2.12}$$

where

$$\mathbf{B}_{eff} = \mathbf{B}_0 + \frac{\boldsymbol{\Omega}}{\gamma}.$$

The above equations explain that the motion of **M** in the rotating frame of reference is of the same form as that in the laboratory reference frame provided the $\mathbf{B}_0$ field is replaced by $\mathbf{B}_{eff}$. Note that if rotation occurs at the Larmor frequency in the sense opposite to that of a right-handed screw advancing along the positive z axis, i.e., $\boldsymbol{\Omega} = -\gamma B_0 \mathbf{k}$, then $\mathbf{B}_{eff}$ and $\partial \mathbf{M}/\partial t$ both reduce to zero indicating that the magnetization **M** appears stationary in the rotating frame.

2.4 Interaction Between Magnetization and an RF Magnetic Field

In order to perform an NMR experiment, it is necessary to perturb the net magnetization from its thermal equilibrium state by irradiating the spin system with a circularly polarized RF magnetic field of angular frequency ω and amplitude B_1 restricted to the transverse plane and rotating in the same sense as the spins. Allowing the rotating frame x-axis (X_ρ) to be defined by the RF magnetic vector, the motion of **M** in the rotating frame is described by

$$\frac{\partial \mathbf{M}}{\partial t} = \mathbf{M} \times \gamma \mathbf{B}_e \tag{2.13}$$

where

$$\mathbf{B}_e = B_1 \mathbf{i}_\rho + (B_0 + \frac{\omega}{\gamma})\mathbf{k}_\rho.$$

The above expression describes the precession of **M** about the effective field $\mathbf{B}_e$ at angular velocity γB_e. If the RF field's frequency is on resonance ($\omega = \omega_0 = \gamma B_0$), then $\mathbf{B}_e$ reduces to $B_1\mathbf{i}_\rho$ and **M** will precess about the X_ρ axis while remaining in the Y_ρ-Z_ρ plane. The angle through which **M** is tipped (θ) is given by

$$\theta = \gamma B_1 t_w \tag{2.14}$$

where t_w is the duration of the RF magnetic field pulse. A $\theta = \pi$ (180°) pulse would invert the magnetization whereas a $\pi/2$ (90°) pulse would tip the magnetization vector **M** into the transverse plane as shown in Fig. 2.2A.

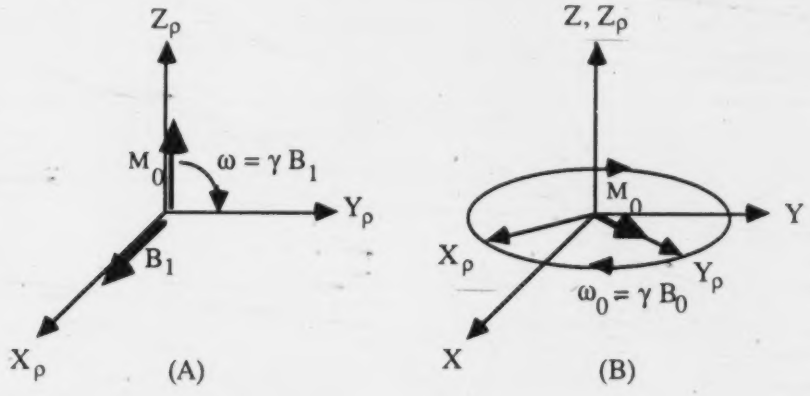

Figure 2.2 (A) Tipping of magnetization into transverse plane by an on-resonance 90° RF pulse. (B) Precession of transverse magnetization at the Larmor frequency in laboratory frame.

After a 90° RF pulse, **M** would be pointing along the Y_ρ axis and would remain stationary in the rotating frame. It would, however, precess at the Larmor frequency in the laboratory frame (see Fig. 2.2B), thereby inducing a measurable voltage across a coil whose axis lies in the transverse plane. This transverse magnetization, precessing freely in the absence of an RF magnetic field, decays exponentially due to transverse relaxation processes. Such a decaying sinusoidal signal is referred to as a free induction decay or FID, and its spectrum consists of Lorentzian lines located at $\pm \omega_0$.

Two RF sinusoidal reference signals, the first in phase with the excitation RF magnetic field and the second in quadrature with respect to the first, are multiplied with the above received signal (whose spectrum is centered about ω_0). The two resulting channels contain components in two frequency bands centered at 0 and $2\omega_0$. Low-pass filtering of both channels retains only the low frequency components which are then digitized and stored to form the real and imaginary parts of a complex FID. This detection scheme, known as quadrature phase-sensitive detection (QPSD), can be equated to detecting the X_ρ and Y_ρ components of the net transverse magnetization.

2.5 Relaxation Phenomena

After being perturbed from their equilibrium values, the longitudinal (M_Z) and transverse (M_{XY}) components of the magnetization, owing to longitudinal and transverse relaxation, respectively, recover to their equilibrium values. For homogeneous samples, the recovery of M_Z is governed by a first-order differential equation characterized by the time constant T_1. Mathematically, this may be expressed as (Abragam, 1961 p44)

$$\frac{dM_Z}{dt} = -\left(\frac{M_Z - M_0}{T_1}\right). \qquad (2.15)$$

In homogeneous samples, the decay of M_{XY} is also a first-order process, characterized by the time constant T_2. Equations describing this process take the form (Abragam, 1961 p44)

$$\frac{dM_X}{dt} = -\frac{M_X}{T_2} \quad ; \quad \frac{dM_Y}{dt} = -\frac{M_Y}{T_2} \quad . \qquad (2.16)$$

2.5.1 Longitudinal Relaxation

Since M_Z is proportional to the the difference in the population of the two states, longitudinal relaxation may be thought to allow for the recovery of the populations to their

equilibrium values. In terms of magnetization, this relaxation process allows M_Z to recover to its equilibrium value of M_0.

Any mechanism responsible for generating fluctuating magnetic fields at the site of a nucleus can contribute to relaxation. Although there are several processes that contribute to longitudinal relaxation, the magnetic dipole-dipole interaction is usually the dominant mechanism for tissue protons. To qualitatively understand this mechanism, consider a spin with another spin as a neighbor. The magnetic moment of the neighboring spin will cause a fluctuating magnetic field at the site of the former spin when there is relative motion between the two spins, say, due to thermal agitation. This fluctuating field, having a component at the Larmor frequency of the original nucleus, is capable of inducing transitions between the two energy states of the nucleus, thus contributing to longitudinal relaxation.

The nature of the rotational and translational motions permitted by the surroundings of the nuclei (the lattice) significantly influences longitudinal relaxation efficiency. For instance, slow rotational motion in solids results in a primarily low-frequency power spectrum of the fluctuating fields. The resulting small amplitude fo the components fluctuating at the Larmor frequency lead to very long spin-lattice relaxation times. Similarly, very rapid rotational motion associated with bulk water, for example, leads to a wide power spectrum with small Larmor frequency components, thus long T_1 values. Alternatively, intermediate thermal motions of water protons bound to macromolecules in tissue result in larger Larmor frequency components and correspondingly shorter T_1 times.

2.5.2 Transverse Relaxation

The second relaxation process, termed transverse relaxation, causes the decay of M_{XY}. Interactions of spin dipoles with other moving dipoles lead to the superimposition of a local magnetic field upon the main field. Obviously, the precessional frequencies of

the nuclei will vary with their location, leading to a dephasing and hence a decay in the net transverse magnetization.

In solids, the dipole-dipole interaction within a rigid environment contributes a large additional local field at nuclear sites resulting in rapid transverse magnetization decay of the order of tens of microseconds. On the other hand, the thermal motion of spins in liquid-like systems averages the local field component of the dipole-dipole relaxation mechanism to small values, resulting in T_2 relaxation times in the range of tens of milliseconds. For a given sample, T_2 is smaller than T_1 and, in the limit, may approach but never exceed T_1.

If we assume that the motion of the magnetization due to precession can be superimposed upon that due to relaxation, then equation 2.8 may be modified to give the complete phenomenological equations of Bloch as follows (Abragam, 1961 pp44-45):

$$\frac{d\mathbf{M}}{dt} = \mathbf{M} \times \gamma[\mathbf{B}_0 + \mathbf{B}_1(t)] - \left(\frac{M_X\mathbf{i}+M_Y\mathbf{j}}{T_2}\right) - \left(\frac{M_Z-M_0}{T_1}\right)\mathbf{k} \; . \qquad (2.17)$$

2.5.3 Two-Site Rapid Exchange Model

Proton relaxation times from tissue are usually found to be different from those of a solution of cellular salts. This result is explained by invoking two environments in which tissue water may exist (Mansfield & Morris, 1982 p15). The majority of cellular water can be considered to exist in a solution of cellular salts but at least 10% of the water molecules are bound to macromolecules. Slower motion associated with the macromolecules allows the bound-water protons to experience fields with large spectral components at the Larmor frequency and zero frequency, leading to efficient relaxation. In contrast, the rapid thermal motion of the unbound water results in smaller magnetic field components at these frequencies and consequently inefficient relaxation. If the water molecules exchange between these two environments rapidly (compared to the time-scale of the relaxation times), the measured relaxation time is given by (Zimmerman and Brittin, 1957)

$$\frac{1}{T} = \frac{1}{T_B}(P_B) + \frac{1}{T_F}(1-P_B) \qquad (2.18)$$

where T, T_B and T_F are the observed, bound-water, and free-water T_1 or T_2 relaxation times, respectively, and P_B is the fraction of cellular water in the bound state.

2.6 Spin Echoes

It was mentioned previously that the dipole-dipole interaction generates a fluctuating magnetic field at the nuclear sites, which adds to the $\mathbf{B}_0$ field. This fluctuating field has a finite zero-frequency component leading to a spread in the resonance frequencies of the individual spins and a dephasing of their resultant transverse magnetization. Any further source of static field inhomogeneity, say due to instrument imperfections, will further contribute to transverse magnetization decay. This net dephasing is characterized by the time constant T_2^* which incorporates the effects of intrinsic irreversible dephasing (T_2) and the reversible dephasing due to static field inhomogeneities (ΔB). The above parameters are related approximately by (Farrar & Becker, 1971 p4)

$$\frac{1}{T_2^*} = \frac{1}{T_2} + \frac{\gamma \Delta B}{2} . \qquad (2.19)$$

Provided the static-field inhomogeneities are time invariant, it is possible to reverse their dephasing effects by utilizing additional RF pulses to generate spin echoes. To illustrate how spin echoes are generated consider the Carr Purcell Meiboom Gill (CPMG) (Meiboom & Gill, 1958) pulse sequence (see Fig. 2.3). Immediately after a $90°_{X\rho}$ RF pulse, where $90°_{X\rho}$ means a 90° pulse applied along the x axis of the rotating frame, all the magnetization isochromats are aligned along the Y_ρ axis thereby inducing a maximum signal (Fig. 2.3A). The field inhomogeneity causes some isochromats to precess faster than the rotating frame while others precess at a lower rate (Fig. 2.3B). After a time τ, a $180°_{Y\rho}$ RF pulse reverses the phase acquired by the isochromats

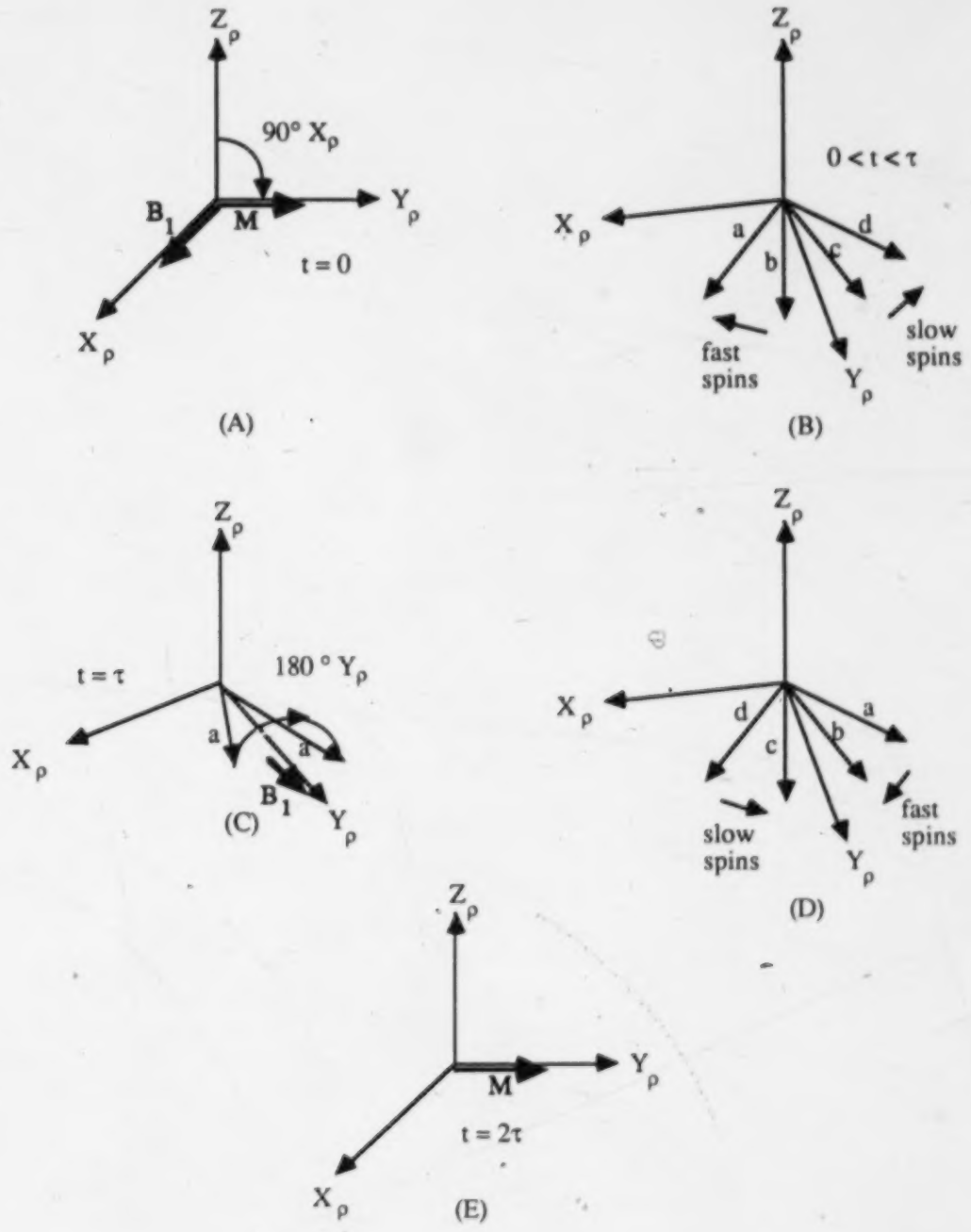

Figure 2.3 Illustration of effect of CPMG spin echo pulse sequence. (A) All magnetization isochromats are in phase after 90° RF pulse. (B) Field inhomogeneity causes dephasing of spin isochromats. (C) 180° RF pulse reverses phase of all spin isochromats. (D) and (E) Isochromats refocus.

(Fig. 2.3C). Since the precessional frequencies of the isochromats remain unchanged, the isochromats refocus (Fig. 2.3D), and the echo signal grows to a maximum at 2τ (Fig. 2.3E). Further echoes can be generated by applying additional $180°_{Y_\rho}$ RF pulses at intervals of 2τ. The amplitude of the echoes will then follow the natural T_2 decay envelope.

2.7 Slice Definition

Before proceeding to discuss two-dimensional Fourier transform (2DFT) NMR imaging, in would be illuminating to see how spins within a given slice in a sample are excited leaving the remaining spins undisturbed, i.e., slice selection. The most common strategy involves the establishment of linear magnetic field gradients together with irradiation with narrow-band RF pulses. At a given location within the sample, the effect of such a linear gradient is to superimpose on the main field $\mathbf{B}_0$ an offset field $b_r\mathbf{k}$ given by

$$b_r\mathbf{k} = (\mathbf{G} \cdot \mathbf{r})\, \mathbf{k} \qquad (2.20)$$

where $\mathbf{G}$ denotes the gradient strength and direction and $\mathbf{r}$ is a vector describing the displacement along the gradient direction at which the offset field is calculated. Fig. 2.4 illustrates the additional field due to a Y-gradient (G_Y).

In the presence of a gradient, slices orthogonal to the gradient direction will be encoded with unique Larmor precessional frequencies. Then the spin system is irradiated with a narrow-band RF pulse whose center frequency defines the slice of interest. Magnetization within the slice interacts with the RF pulse and is tipped into the transverse plane, leaving, in principle, the remaining magnetization unaltered. Mansfield et al. (1979) have shown that a low-amplitude rectangular RF pulse results in a transverse magnetization slice profile with a main lobe corresponding to the slice of interest, and significant unwanted side lobes. More ideal slice profiles are obtained if RF pulse envelopes are amplitude modulated to control the power spectrum of the irradiation by, for example,

Gaussian or Gaussian-windowed Sinc (Locher, 1980) waveforms. Nevertheless, one must always bear in mind that the equations of motion for the off-resonance magnetization are not linear in tip angle, and therefore one cannot carry too far any correspondence between the power spectrum and the slice profile of the excited magnetization. For small tip angle selective pulses, the slice thickness is inversely related to the slice gradient strength and proportional to the RF pulse bandwidth.

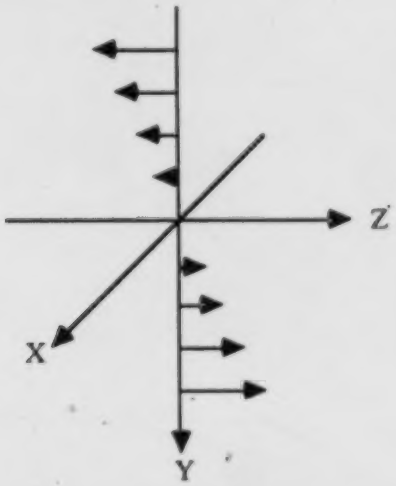

Figure 2.4 Illustration of offset magnetic field produced by a linear field gradient in the Y direction (G_Y). The length and direction of the arrows depicts the magnitude and sign of the offset fields.

Another unfortunate side effect of off-resonance conditions for some spins is the resultant phase distribution of M_{XY}. Although significant transverse magnetization is generated within the slice of interest, the phase of the magnetization within this slice is linearly distributed across the slice direction, giving a greatly reduced net transverse magnetization vector, hence a very small detected signal. One remedy to this problem is to exploit the linear nature of this phase distribution. After the shaped RF pulse, reversing the direction of the slice selection gradient for an appropriate duration allows the magnetization isochromats within the slice to partially refocus, resulting in a larger net transverse magnetization vector aligned with the Y_ρ axis (Sutherland et al., 1978; Hoult, 1979).

2.8 Two-Dimensional Fourier Transform NMR Imaging

Although several techniques can be used to generate NMR images, the Fourier method is currently the most widespread technique. In this section, two-dimensional Fourier transform (2DFT) NMR imaging will be addressed. Fig. 2.5 details a typical 2DFT NMR imaging pulse sequence.

This scheme of NMR imaging requires the ability to selectively establish any combination of three orthogonal linear magnetic field gradients (G_X, G_Y and G_Z), as well as shape the RF excitation pulse envelope. The signal obtained from a single execution of the sequence illustrated in Fig. 2.5 is called a projection. Narrowband RF irradiation of a subject placed in a slice gradient (G_Z) tips the equilibrium magnetization of a narrow slice of spins into the transverse plane. To refocus most of the transverse magnetization within the slice, the slice gradient is reversed (slice rephase gradient) for a short duration so that the area under this rephase gradient is half the gradient area during the 90° excitation pulse. A complete 2DFT NMR image data set is obtained by collecting 2n (typically 128) projections with the phase gradient usually increased (or decreased) in a monotonical manner by a fixed amount ΔG. By establishing a phase gradient (G_Y in this case) for a short duration t_Y, the y coordinate information of each voxel is encoded into the phase of the voxel's NMR signal. The voxel's x coordinate in encoded into the NMR signal frequency since the signal is acquired in the presence of the read (G_X) gradient. The resulting echo signal is uniformly sampled 2N times every Δt seconds during the acquisition window.

The simplest manner of understanding this method of imaging involves the total neglect of relaxation phenomena and the tracing, in the rotating frame, of the evolution of the magnetization of a single voxel (of amplitude m) during one projection of the imaging procedure. Before proceeding further, the time origin of the recorded data is defined to

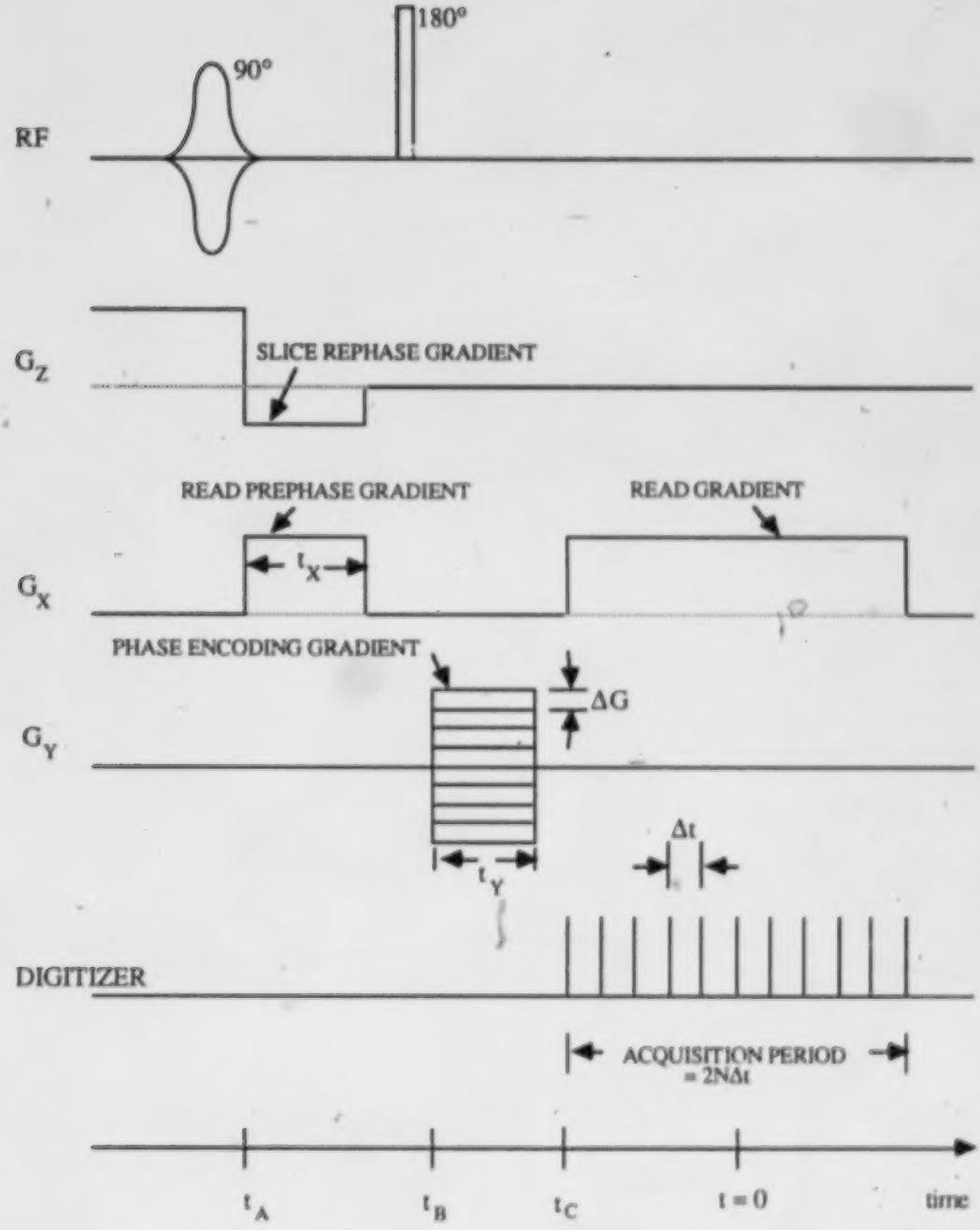

Figure 2.5 A simple RF and gradient pulse sequence for 2DFT spin-echo NMR imaging.

coincide with the center of the acquisition period. Immediately after the slice selection portion of the pulse sequence, this voxel, centered at (x,y), will contain transverse magnetization of amplitude m aligned with the Y_ρ axis. During the prephase portion of the read gradient (before the 180° RF pulse), this transverse magnetization precesses at a frequency $\omega = -\gamma G_X x$ acquiring a phase angle (θ) of

$$\theta = -\int_{t_A}^{t_A + t_X} \gamma G_X x dt$$

$$= -\gamma G_X x t_X \qquad (2.21)$$

with respect to the Y_ρ axis at the end of this period. The effect of the 180° RF pulse is to reverse the sign of the phase angle acquired so far. A phase gradient of strength G_Y and duration t_Y adds to the magnetization's phase giving

$$\theta = \gamma G_X x t_X - \int_{t_B}^{t_B + t_Y} \gamma G_Y y dt$$

$$= \gamma G_X x t_X - \gamma G_Y y t_Y. \qquad (2.22)$$

The read gradient during the acquisition period causes this magnetization to precess at a frequency $\omega = -\gamma G_X x$. The magnetization's phase during the acquisition period is then expressed by

$$\theta = \gamma G_X x t_X - \gamma G_Y y t_Y - \int_{t_C}^{t} \gamma G_X x dt$$

$$= \gamma G_X x t_X - \gamma G_X x (t - t_C) - \gamma G_Y y t_Y. \qquad (2.23)$$

Since the pulse sequence is calibrated so that the phase acquired during the prephase portion of the read gradient cancels the phase acquired in the first half of the acquisition period, this expression for the magnetization's phase then reduces to

$$\theta(G_Y,t) = -\gamma G_Y y t_Y - \gamma G_X x t \,. \qquad (2.24)$$

Using the QPSD technique and letting the Y_ρ and X_ρ components of the magnetization give rise to the signal in the real (u[t]) and imaginary (v[t]) channels, respectively, the complex signal recorded is expressed as

$$s'(t,G_Y) = u(G_Y,t) + i\, v(G_Y,t) = m \exp[-i(\gamma G_X x t + \gamma G_Y y t_Y)]. \qquad (2.25)$$

The above equation reflects the contribution of only one voxel to the detected signal. When all the voxels of the slice are accounted for, the total signal is

$$s(t,G_Y) = \int\int m(x,y) \exp[-i (\gamma G_X x t + \gamma G_Y y t_Y)]\, dx\, dy \qquad (2.26)$$

where m(x,y) is the spatial distribution of transverse magnetization in the slice. Defining the spatial frequencies ω_X and ω_Y as

$$\omega_X = \gamma G_X t \quad ; \quad \omega_Y = \gamma G_Y t_Y \,, \qquad (2.27)$$

the recorded signal may be rewritten as

$$s(\omega_X,\omega_Y) = \int\int m(x,y) \exp[-i (\omega_X x + \omega_Y y)]\, dx\, dy$$

$$= F[m(x,y)] \qquad (2.28)$$

where F represents the Fourier transform operator. The image $\hat{m}(x,y)$ is calculated by inverse Fourier transforming the dataset $s(\omega_X,\omega_Y)$ to give

$$\hat{m}(x,y) = \mathsf{F}^{-1}[s(\omega_X,\omega_Y)] = m(x,y). \qquad (2.29)$$

The calculated image therefore reflects the spatial distribution of magnetization in the imaged slice. Normally, the modulus of each element in the complex image matrix $\hat{m}(x,y)$ is converted into a pixel intensity in order to display the final NMR image.

CHAPTER 3

THEORETICAL ANALYSIS OF PULSATILE FLOW ARTIFACTS IN NMR IMAGING

3.1 Introduction

The principal objective of this thesis is the development and implementation of schemes that reduce or eliminate pulsatile flow artifacts in 2DFT NMR images. Towards this end, this chapter presents a model for the pulsatile flow of spins and investigates the artifacts expected in 2DFT NMR images from such motion. It is hoped that the insight gained from this exercise will suggest schemes that will either reduce or eliminate these artifacts. The final section of this chapter shows how the synchronization technique is used to suppress these artifacts.

The RF and gradient pulse sequence used for 2DFT NMR images presented in this thesis differs slightly from the one presented in Chapter 2; it is shown in Fig. 3.1, and the pulse program timings are shown in Table 3.1. Assuming perfect gradient and RF pulses, the two pulse sequences yield identical images if the spins are motionless. Delaying the refocus portion of the slice gradient (G_Z) until after the 180° RF pulse enables this gradient pulse to perform two functions simultaneously. Firstly, it refocuses the in-slice transverse magnetization, and secondly, it acts as a spoiler gradient for the out-of-slice transverse magnetization resulting from imperfect 180° RF pulses. It is also necessary to employ trim gradients (G_X) after each acquisition period to center the higher order echoes. For the case where the spins are moving, the resulting images will depend upon both the nature of the motion and the details of the pulse sequence used.

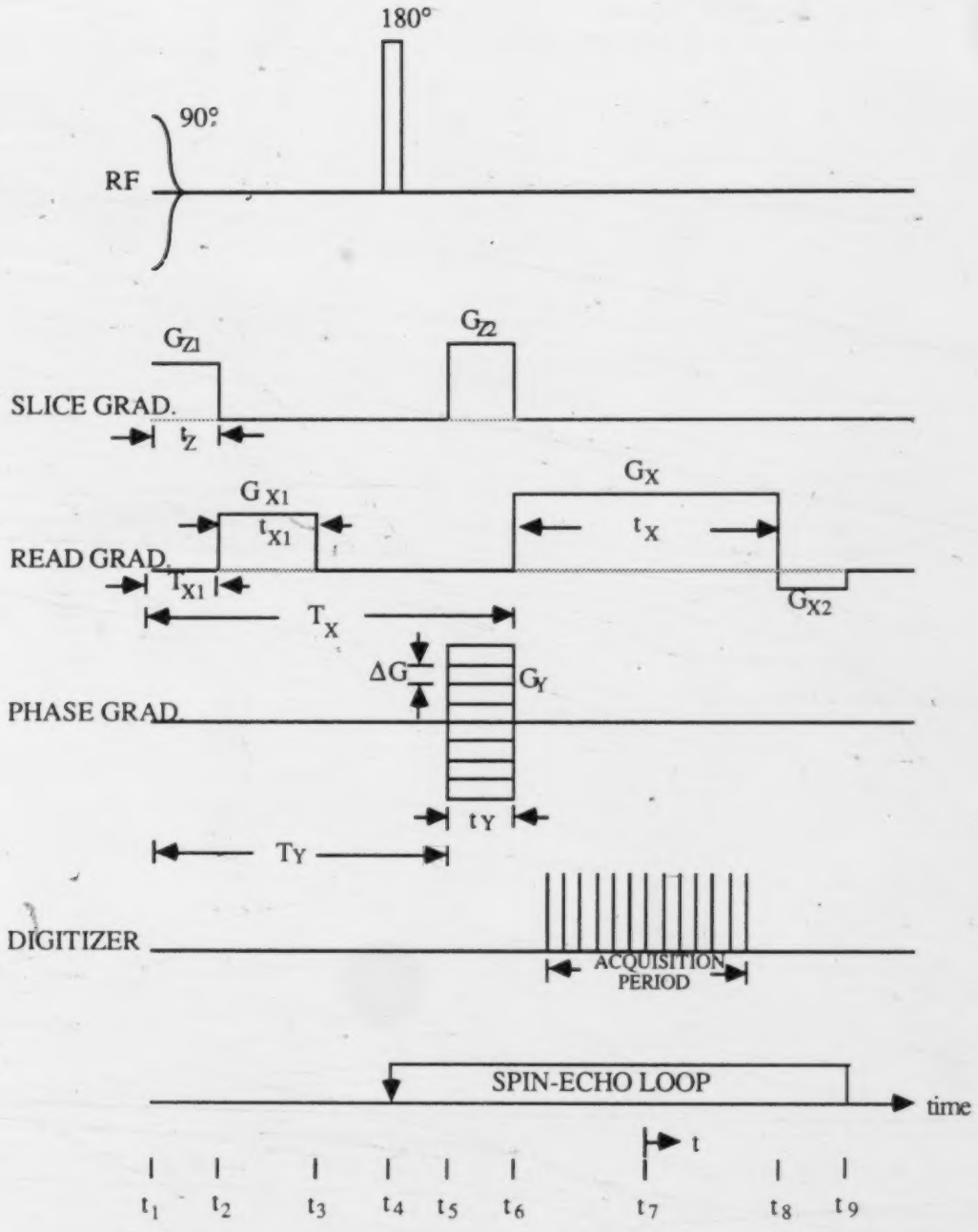

Figure 3.1 The 2DFT NMR multi-echo imaging pulse sequence used for imaging. The slice refocus and phase encoding gradients are applied only on the first pass through the spin-echo loop.

Pulse-program timing parameters	Value (ms)
T_{X1}	3.84
t_{X1}	5.304
T_X	18.384
t_X	12.288
T_Y	14.384
t_Y	4.0
t_Z	7.68
T_E	26.528

Table 3.1 Pulse program timing parameters for the pulse program shown in Fig. 3.1.

3.2 Pulsatile Flow Artifacts in 2DFT NMR Imaging

Considering only steady flow, three basic flow effects are encountered in NMR imaging: replacement of partially saturated longitudinal magnetization with fully realxed magnetization, displacement of excited spins, and phase shifts of spins moving along a magnetic field gradient. Whether these effects are manifested in 2DFT NMR images or not, and to what extent, will depend on the specific pulse sequence used. Axel (1984) has published a short review of steady-flow effects in NMR imaging. These steady-flow effects are concerned primarily with either the loss or enhancement of the NMR signal due to flowing spins, and not with the blurring and ghosting artifacts that severely degrade thoracic 2DFT NMR images. The works of Wood and Henkelman (1985,1986a,b), and Haake and Patrick (1986), which show the replications of the moving structures in the phase encoding direction at discrete spacings (ghosting) due to sinusoidal motion, are more relevant to the subject of this thesis. Their analyses show that blurring in the direction of motion is evident only when there is a component of the oscillatory motion parallel to the defined slice. Perman et al. (1986) have shown that pulsatile flow along the read direction leads to ghosting. The analysis to follow is an extension of the works of Wood and Henkelman, Haake and Patrick, and Perman et al. For the sake of simplicity, the pulsatile flow of spins will be decomposed into components along the three Cartesian axes, x, y,

and z, and the effects of pulsatile flow along each of these directions will be evaluated separately. Neglecting relaxation phenomena and the enhancement or loss of signal due to steady flow, the effect of pulsatile flow on first echo images will be investigated. This analysis will then be generalized to account for higher echo images.

3.2.1 First Echo Images

Quantitative evaluation of the effect of pulsatile flow in 2DFT NMR imaging requires a model to describe the motion of the spins. A complicated model would be required to accurately describe the follow encountered in the major blood vessels of a cat. For present purposed, a simple and inexhaustive model for pulsatile flow, used in the following analysis, specifies the velocity term of the motion to consist of a constant and a fundamental harmonic component. Consider the contents of a volume element in the slice defined by the selective 90° RF pulse of the imaging sequence, and allow these spins to flow. Letting the imaging experiment be unsynchronized to the pulsatile flow, the location of this spin packet, during any projection, is given by the following equations:

$$x(t) = x + \int_{t_1}^{t} [V_X + A_X \sin(\Omega \hat{t})]dt ,$$

$$y(t) = y + \int_{t_1}^{t} [V_Y + A_Y \sin(\Omega \hat{t})]dt ,$$

$$z(t) = z + \int_{t_1}^{t} [V_Z + A_Z \sin(\Omega \hat{t})]dt , \qquad (3.1)$$

where x(t), y(t) and z(t) are the Cartesian coordinates of this spin packet, expressed as functions of the time variable t. The origin of t coincides with the center of the first echo's acquisition period for each projection, and the 90° RF pulse acts at time t_1 (see Fig. 3.1). In the above expression, x, y and z represent the location of the spin packet at t_1, V_X, V_Y

and V_Z represent the average flow velocities along the Cartesian axes, and A_X, A_Y and A_Z are the corresponding amplitudes of the sinusoidal portion of the flow whose frequency is denoted by Ω. $\hat{t}$ is the time variable that spans the entire imaging experiment and is related to the variable t by:

$$\hat{t} = \frac{G_Y t_r}{\Delta G} + n t_r + t , \qquad (3.2)$$

where t_r, the repetition time, is the duration of time from the start of one projection to the start of the next. G_Y, the phase encoding gradient strength, has a starting amplitude of $-n\Delta G$ and is incremented in steps of ΔG for each new projection. For the kth projection, we then have

$$G_Y = (k-n)\,\Delta G \quad ; \quad k = 0,1,2, \ldots , 2n-1. \qquad (3.3)$$

To simplify the expressions of equation 3.1, we assume that the oscillatory components of the velocity terms are invariant during a pulse sequence, but change from one projection to the next. In this case, equation 3.1 may be simplified to read:

$$x(t) = x + [V_X + A_X \sin(\Omega t')](t - t_1),$$

$$y(t) = y + [V_Y + A_Y \sin(\Omega t')](t - t_1),$$

$$z(t) = z + [V_Z + A_Z \sin(\Omega t')](t - t_1), \qquad (3.4)$$

where

$$t' = \frac{G_Y t_r}{\Delta G} + n t_r . \qquad (3.5)$$

3.2.1.1 Pulsatile Flow Normal to the Slice.

Consider the spins contained in a voxel in the defined slice. If this packet of spins experiences pulsatile flow only in the direction normal to the slice (z), then its x and y coordinates will remain unchanged. However, the z coordinate of such a spin packet is described by

$$z(t) = z + [V_Z + A_Z\sin(\Omega t')](t - t_1)\,. \qquad (3.6)$$

Movement of this elemental volume of spins in the presence of the slice selection gradient causes the transverse magnetization of this spin packet to accumulate an excess phase ϕ_Z. To accurately calculate this transverse magnetization's phase at the end of the slice selection procedure (t_2), it is necessary to obtain an expression for the effective magnetic field, $\mathbf{B}_{eff}$, in the rotating frame during this period. It would then be possible to calculate the final phase of this magnetization by tracing its evolution, under the influence of this effective field, in the rotating frame. Such a calculation is more amenable to computer simulation than to analytical evaluation. To simplify matters, we assume that the magnetization of this spin packet is tipped onto the Y_ρ axis at the center of the 90° RF pulse (t_1), and thereafter, this magnetization precesses in the presence of the slice gradient until time t_2. The excess phase ϕ_Z is then given by

$$\phi_Z = \int_{t_1}^{t_2} \gamma G_{Z1}\{z+[V_Z+A_Z\sin(\Omega t')]\,(t - t_1)\}dt - \int_{t_5}^{t_6} \gamma G_{Z2}\{z+[V_Z+A_Z\sin(\Omega t')]\,(t - t_1)\}dt$$

$$= z[\,\gamma G_{Z1} t_Z - \gamma G_{Z2} t_Y\,] + \phi_{ZV} + \phi_{ZA}\sin(\Omega t') \qquad (3.7)$$

where

$$\phi_{ZV} = \frac{V_Z}{2}[\gamma G_{Z1} t_Z^2 - 2\gamma G_{Z2} t_Y (T_Y + \frac{t_Y}{2})]$$
$$\phi_{ZA} = \frac{A_Z}{2}[\gamma G_{Z1} t_Z^2 - 2\gamma G_{Z2} t_Y (T_Y + \frac{t_Y}{2})]$$
$$T_Y = t_5 - t_1 \qquad (3.8)$$
$$t_Z = t_2 - t_1$$
$$t_Y = t_6 - t_5.$$

The z-gradient amplitudes and durations are calibrated so as to nullify the first term of equation 3.7, thereby simplifying it to

$$\phi_Z = \phi_{ZV} + \phi_{ZA}\sin(\Omega t'). \qquad (3.9)$$

Incorporating this excess phase into the expression for the acquired signal, which reflects the contribution of all the voxels in the slice, gives

$$s(t,G_Y) = \exp[i\phi_{ZV}] \int\int m(x,y)\exp\{i\phi_{ZA}\sin[\Omega(\frac{G_Y t_r}{\Delta G} + nt_r)]\}\exp[-i(\gamma G_X x t + \gamma G_Y y t_Y)]dxdy . \qquad (3.10)$$

Note that in the above expression m(x,y) is independent of time. This implies that although the flow is pulsatile, it is also laminar, so that the distribution of transverse magnetization m(x,y) generated within the selected slice does not change from one projection to the next. Exploiting the identity (Gradshteyn & Ryzhik, 1980)

$$\exp[i\,\delta\sin(\theta)] = \sum_{p=-\infty}^{\infty} J_p(\delta)\exp(i\,p\theta), \qquad (3.11)$$

where J_p is the pth order Bessel function of the first type, and utilizing the definitions for ω_X and ω_Y, the expression for $s(t,G_Y)$ may be reduced to read

$$s(\omega_X,\omega_Y) = \exp[i\phi_{ZV}] \sum_{p=-\infty}^{\infty} K_p \iint m(x,y+p\bar{Y}) \exp[-i(\omega_X x+\omega_Y y)]dxdy$$

$$= \exp[i\phi_{ZV}] \sum_{p=-\infty}^{\infty} K_p \, F\{m(x,y+p\bar{Y})\}, \tag{3.12}$$

where

$$K_p = \exp[ip\Omega nt_r] \, J_p[\phi_{ZA}]$$
$$\bar{Y} = \frac{\Omega t_r}{\gamma \Delta G t_Y}, \tag{3.13}$$

and p is an integer. In accordance with normal procedure, the final image is calculated by inverse Fourier transforming $s(\omega_X,\omega_Y)$, resulting in

$$\hat{m}(x,y) = \exp[i\phi_{ZV}] \sum_{p=-\infty}^{\infty} K_p \, m(x,y+p\bar{Y}). \tag{3.14}$$

The above equation clearly shows that the final image consists of the summation of the real structure (p=0) and ghost structures ($p\neq0$), with each ghost translated in the phase-encoding (y) direction by a multiple of $\bar{Y}$ (Fig 3.2C). For typical values of imaging and flow parameters, $\bar{Y}$ falls in the range of decimeters. Notice that equation 3.14 predicts no blurring of the principal or ghost structures. For a fixed argument, the value of any higher order Bessel function approaches zero. Therefore, the amplitudes of the higher-order ghost structures are expected to decay. However, it is possible for the main structure to have a lesser magnitude than immediately neighboring ghosts for certain values of the Bessel function argument ϕ_{ZA}. If A_Z is zero (steady flow), then ϕ_{ZA} vanishes. For a zero argument, the zeroth order Bessel function is unity and the higher order functions vanish. The final image will therefore contain only the principal structure (see Fig 3.2B) with a

phase of ϕ_{ZV}. For the case of no flow ($A_Z = V_Z = 0$), the calculated image $\hat{m}(x,y)$ will equal the magnetization distribution of the slice $m(x,y)$ (Fig 3.2A).

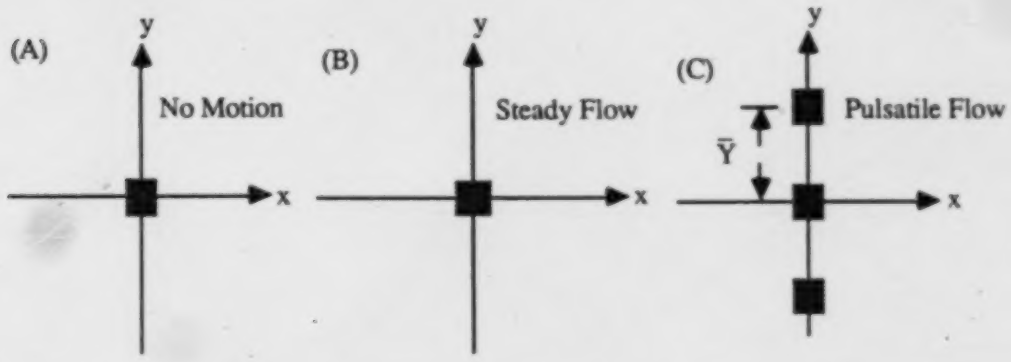

Figure 3.2 Diagrammatic representations of first-echo 2DFT NMR modulus images of an elemental volume of spins located at the origin at the time of the 90° RF pulse. In (A) the spin packet is stationary; (B) and (C) show the effect of steady and pulsatile flow, respectively, normal to the slice. Only the first order ghosts ($p = \pm 1$) are shown in (C).

3.2.1.2 Pulsatile Flow Along the Phase-Encoding Direction.

Next, consider an elemental volume of spins flowing in a pulsatile manner along the phase-encoding (y) direction. The spin packet's y coordinate during any projection is given by

$$y(t) = y + [V_Y + A_Y \sin(\Omega t')](t - t_1), \tag{3.15}$$

and the other two coordinates remain fixed. The excess phase (ϕ_Y) accumulated due to spins moving in the phase-encoding direction during a phase-encoding gradient is given by

$$\begin{aligned}\phi_Y &= -\int_{t_3}^{t_6} \gamma G_Y \{ y + [V_Y + A_Y \sin(\Omega t')](t - t_1) \} \, dt \\ &= -\gamma G_Y y t_Y - \gamma G_Y t_Y V_Y (T_Y + \tfrac{t_Y}{2}) - \gamma G_Y t_Y A_Y (T_Y + \tfrac{t_Y}{2}) \sin(\Omega t') \\ &= -\omega_Y (y + \hat{y}) + \tilde{y} \omega_Y \sin(\bar{Y} \omega_Y + \Omega n t_r),\end{aligned} \tag{3.16}$$

where

$$\hat{y} = V_Y(T_Y + \frac{t_Y}{2})$$
$$\bar{y} = -A_Y(T_Y + \frac{t_Y}{2}). \tag{3.17}$$

Using a procedure similar to that of the previous section, the acquired signal is expressed more simply in the form

$$s(\omega_X,\omega_Y) = \sum_{p=-\infty}^{\infty} K_p(\omega_Y) \int\int m(x,y) \exp\{-i\,[\omega_X x + \omega_Y(y + \hat{y} - p\bar{Y})]\}\, dxdy \tag{3.18}$$

where

$$K_p(\omega_Y) = \exp(ip\Omega nt_r)\, J_p(\bar{y}\omega_Y). \tag{3.19}$$

For typical experimental values of flow velocity (10 cm s^{-1})and pulse timings used, the displacement term $\hat{y}$ evaluates to approximately one millimeter whereas the $\bar{Y}$ can be about two orders of magnitude larger. Equation 3.18 may be written as

$$s(\omega_X,\omega_Y) = \sum_{p=-\infty}^{\infty} K_p(\omega_Y)\, F[\, m(x,y - \hat{y} + p\bar{Y})\,]\,. \tag{3.20}$$

The final image, obtained by inverse Fourier transforming $s(\omega_X,\omega_Y)$, is

$$\hat{m}(x,y) = \sum_{p=-\infty}^{\infty} F^{-1}[K_p(\omega_Y)] * m(x,y - \hat{y} + p\bar{Y})\,, \tag{3.21}$$

where the symbol * is used to denote a two-dimensional convolution. $F^{-1}[K_p(\omega_Y)]$ is given by (Abramowitz and Stegun, 1965) as

$$F^{-1}[\, K_p(\omega_Y)] = \exp(ip\Omega nt_r)\delta(x)\, \frac{(-i)^p T_p(\frac{-y}{\bar{y}})}{\sqrt{\bar{y}^2 - y^2}} \quad ; y^2 < \bar{y}^2$$
$$= 0 \quad ; y^2 \geq \bar{y}^2, \tag{3.22}$$

where T_p is the pth order Chebyshev polynomial.

The final image is again a summation of the main structure (p=0) and ghost structures (p≠0). The convolution in equation 3.21 is responsible for blurring these structures in the phase-encoding (y) direction and each ghost is again translated in the phase-encoding direction by a multiple of $\bar{Y}$ (Fig 3.3C). Evaluation of typical values for the parameter $\bar{y}$ shows that its amplitude is approximately one millimeter. The resulting blurring is at most $2\bar{y}$ and the details of each ghost's blurring will depend upon the corresponding Chebyshev polynomial. Since the maximum amplitude of any Chebyshev polynomial is unity, this analysis suggests that the amplitudes of the ghost will not decay. However, since the acquired signal matrix $s(\omega_X,\omega_Y)$ has finite power, the higher order ghost structures are expected to decay. The pixels associated with the flowing voxels will be shifted by $\hat{y}$ in the principal and ghost structures. When only steady flow occurs ($A_Y = 0$), then $\bar{y}$ evaluates to zero and $K_p(\omega_Y)$ vanishes for all non-zero values of p. The image contains only the main structure with the moving voxels shifted by $\hat{y}$ (Fig 3.3B). If there is no flow ($A_Y = V_Y = 0$), then $\hat{y}$ also vanishes and $\hat{m}(x,y)$ equals $m(x,y)$ (Fig 3.3A).

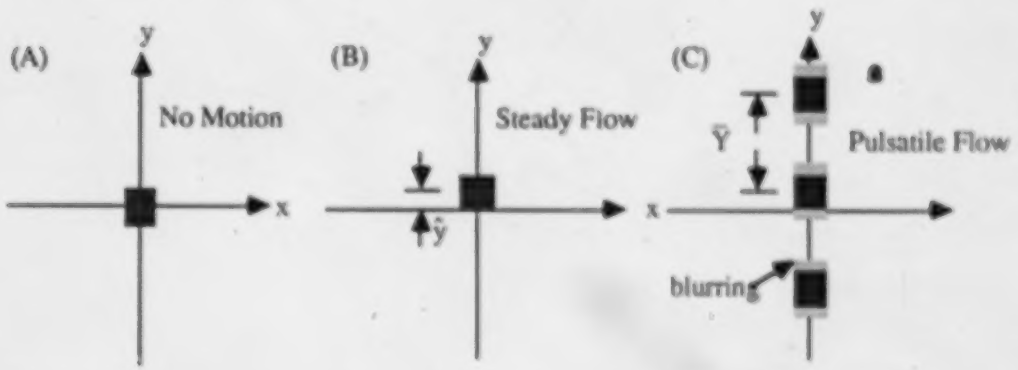

Figure 3.3 Diagrammatic representations of first-echo 2DFT NMR modulus images of an elemental volume of spins located at the origin at the time of the 90° RF pulse. In (A) the spin packet is stationary; (B) and (C) show the effect of steady and pulsatile flow, respectively, in the phase encoding direction. Only the first order ghosts (p = ±1) are shown in (C).

3.2.1.3 Pulsatile Flow Along the Read-Encoding Direction

Lastly, the case where an elemental volume of spins flows only in the read-encoding (x) direction is examined. The x coordinate of such a spin packet's magnetization for any projection is then given by

$$x(t) = x + [V_X + A_X\sin(\Omega t')](t - t_1). \qquad (3.23)'$$

This movement, in the presence of a read gradient, leads to an excess phase accumulation (ϕ_X) that is calculated by evaluating

$$\phi_X = \int_{t_2}^{t_3} \gamma G_{X1}\{x + [V_X + A_X\sin(\Omega t')](t - t_1)\}dt - \int_{t_6}^{t} \gamma G_X\{x + [V_X + A_X\sin(\Omega t')](t - t_1)\}dt$$

$$= x\,[\gamma G_{X1} t_{X1} - \gamma G_X(t - t_6)] + \frac{V_X}{2} K(\omega_X) + \frac{A_X}{2} K(\omega_X)\sin(\Omega t'), \qquad (3.24)$$

where

$$K(\omega_X) = 2\gamma G_{X1} t_{X1}\left(T_{X1} + \frac{t_{X1}}{2}\right) - \left[\frac{\omega_X^2}{\gamma G_X} + 2\omega_X(T_X + t_X) + \gamma G_X\left(T_X t_X + \frac{t_X^2}{4}\right)\right]$$

$$T_{X1} = t_2 - t_1 \qquad (3.25)$$

$$t_{X1} = t_3 - t_2$$

$$T_X = t_6 - t_1$$

$$t_X = t_8 - t_6.$$

The above expression for ϕ_X may be simplified by noting that the pulse sequence is calibrated to cancel the first term of equation 3.24 when t = 0. This results in

$$\phi_X = \phi_{XV} - \omega_X(x + \hat{x}) - \frac{V_X}{2\gamma G_X}\omega_X^2 + \frac{A_X}{2} K(\omega_X)\sin(\bar{Y}\omega_Y + \Omega n t_r) \qquad (3.26)$$

where

$$\phi_{XV} = V_X\left[\gamma G_{X1} t_{X1}\left(T_{X1} + \frac{t_{X1}}{2}\right) - \frac{\gamma G_X}{2}\left(T_X t_X + \frac{t_X^2}{4}\right)\right]$$

$$\hat{x} = V_X \left(T_X + \frac{t_X}{2} \right).$$

Incorporating this excess phase into the expression for the acquired signal $s(\omega_X,\omega_Y)$ we have

$$s(\omega_X,\omega_Y) = \exp(i\phi_{XV}) \int\int m(x,y) \exp[-i\frac{V_X}{2\gamma G_X} \omega_X^2] \exp[i\frac{A_X}{2} K(\omega_X) \sin(\bar{Y}\omega_Y + \Omega n t_r)] \exp\{-i[\omega_X(x + \hat{x}) + \omega_Y y]\}\, dxdy\,, \tag{3.27}$$

which, using a procedure similar to that of previous sections, may be reduced to

$$s(\omega_X,\omega_Y) = \exp(i\phi_{XV}) \sum_{p=-\infty}^{\infty} K'(\omega_X)\, K_p(\omega_X)\, F[m(x - \hat{x}, y + p\bar{Y})] \tag{3.28}$$

where

$$K'(\omega_X) = \exp\left[-i\frac{V_X}{2\gamma G_X}\omega_X^2 \right]$$
$$K_p(\omega_X) = \exp\left(ip\Omega n t_r\right) J_p\left[\frac{A_X}{2} K(\omega_X) \right]. \tag{3.29}$$

The final image, obtained by inverse Fourier transforming $s(\omega_X,\omega_Y)$, is

$$\hat{m}(x,y) = \exp(i\phi_{XV}) \sum_{p=-\infty}^{\infty} F^{-1}[K'(\omega_X)] * F^{-1}[K_p(\omega_X)] * m(x - \hat{x}, y + p\bar{Y}). \tag{3.30}$$

Again, the image consists of the summation of the principal structure (p=0) and ghost structures (p≠0). The moving voxels are shifted in the read-encoding (x) direction by $\hat{x}$ in all of these structures. For typical flow and imaging parameters, $\hat{x}$ evaluates to about three millimeters. All the ghost structures are also translated in the phase-encoding (y) direction by multiples of $\bar{Y}$ (Fig 3.4C). The two convolutions indicated in equation 3.30 account for the blurring of each of these structures in the read direction. The nature of each ghost's blurring will, in general, be different. Attempts to evaluate $F^{-1}[K'(\omega_X)]$ and $F^{-1}[K_p(\omega_X)]$

analytically were unsuccessful. These functions are probably more amenable to a computer evaluation. If only steady flow occurs ($A_X = 0$), $K_p(\omega_X)$ is zero for all non-zero values of p. The final image contains a less blurred (due to the convolution with $F^{-1}[K'(\omega_X)]$) main structure having the phase ϕ_{XV} (Fig 3.4B). For the static case ($A_X = V_X = 0$), $\hat{x}$ vanishes and $K'(\omega_X)$ evaluates to unity with the result that $\hat{m}(x,y)$ equals $m(x,y)$ (Fig 3.4A).

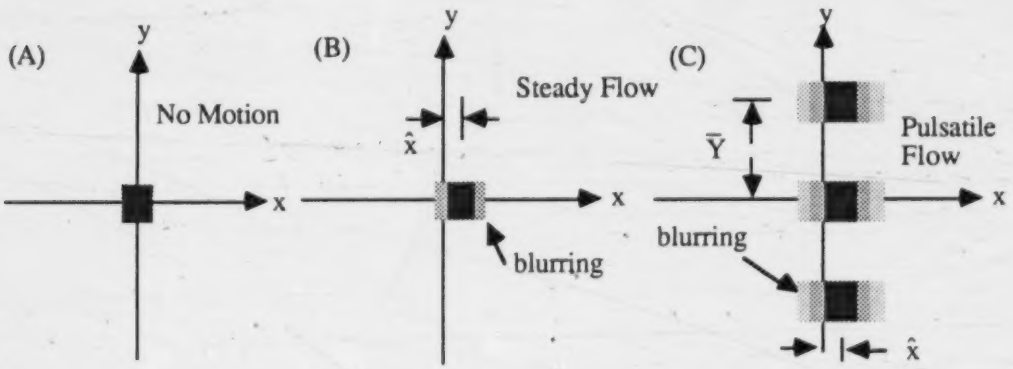

Figure 3.4 Diagrammatic representations of first-echo 2DFT NMR modulus images of an elemental volume of spins located at the origin at the time of the 90° RF pulse. In (A) the spin packet is stationary; (B) and (C) show the effect of steady and pulsatile flow, respectively, in the read-encoding direction. Only the first-order ghosts ($p = \pm 1$) are shown in (C).

3.2.2 Higher-echo images

The analysis to follow is an extension of that presented earlier. Initially, expressions for higher echo images will be derived for the case of stationary spins. Then, the effect of pulsatile flow on the higher echo images will be assessed. As in section 3.2.1, the pulsatile flow will be decomposed into components along the Cartesian axes, and the effect of each component will be evaluated separately. Relaxation and steady-flow phenomena will be neglected.

For an unsynchronized imaging experiment, the x,y and z coordinates of a voxel's magnetization for the Eth echo during any projection are given by :

$$x(t) = x + \int_{t_1 - (E-1)T_E}^{t} [V_X + A_X \sin(\Omega \hat{t})]dt ,$$

$$y(t) = y + \int_{t_1 - (E-1)T_E}^{t} [V_Y + A_Y \sin(\Omega \hat{t})]dt ,$$

$$z(t) = z + \int_{t_1 - (E-1)T_E}^{t} [V_Z + A_Z \sin(\Omega \hat{t})]dt . \qquad (3.32)$$

Notice that the origin of the time variable t has been shifted to the center of the Eth acquisition period although the numerical value of the pulse sequence timings (t_1,t_2, etc.) remain unchanged.

3.2.2.1 Stationary Spins

The data matrix obtained from 2DFT NMR imaging may be written as

$$s(\omega_X,\omega_Y) = \int\int m(x,y) \exp(i\phi)\, dx\, dy \qquad (3.33)$$

where ø represents the phase of the magnetization belonging to a voxel located at (x,y). For the first echo image of stationary spins (see section 2.8),

$$\phi = -(\omega_X x + \omega_Y y). \qquad (3.34)$$

To calculate the value of ø for the Eth image ($E \geq 1$) of a multi-echo pulse sequence, it is necessary that the phase contributions due to each gradient pulse be evaluated during the Eth echo. For reasons mentioned in section 3.2.1.1, we assume that the 90° RF pulse effectively tips the magnetization of the slice onto the Y_ρ axis at time t_1. Thereafter, the

spins precess in the presence of the various gradient pulses. The contribution to the total phase ø due to the z-gradient pulses at the Eth echo is

$$\phi_Z = (-1)^{E-1}\left\{\int_{t_1 - (E-1)T_E}^{t_2 - (E-1)T_E} \gamma G_{Z1} z dt - \int_{t_5 - (E-1)T_E}^{t_6 - (E-1)T_E} \gamma G_{Z2} z dt\right\}$$

$$= (-1)^{E-1}\ \{z[\gamma G_{Z1}(t_2 - t_1) - \gamma G_{Z2}(t_6 - t_5)]\}. \qquad (3.35)$$

In the above expression, T_E represents the time from the center of one acquisition period to the center of the next echo's acquisition period. The factor $(-1)^{E-1}$ results from the effect of the train of (E-1) 180° RF pulses prior to the Eth echo. Since the pulse sequence is calibrated so that the area under the G_{Z1} and G_{Z2} gradient pulses is the same, ϕ_Z evaluates to zero as before.

Next, the contribution of the y-gradient pulse to the total phase ø is

$$\phi_Y = (-1)^{E-1}\left\{-\int_{t_5 - (E-1)T_E}^{t_6 - (E-1)T_E} \gamma G_Y y\, dt\right\}$$

$$= (-1)^{E-1}[-\gamma G_Y y t_Y] = (-1)^{E-1}(-\omega_Y y). \qquad (3.36)$$

Lastly, the contribution of the initial read prephase gradient and E read and trim gradients to the total phase is evaluated at the Eth acquisition period, giving

$$\phi_X = (-1)^{E-1}\left\{\int_{t_2 - (E-1)T_E}^{t_3 - (E-1)T_E} \gamma G_{X1} x\, dt\right\} + \left\{\sum_{k=1}^{E-1} (-1)^{k-1}\left[\int_{t_6 - kT_E}^{t_8 - kT_E} \gamma G_X x\, dt + \int_{t_8 - kT_E}^{t_9 - kT_E} \gamma G_{X2} x\, dt\right]\right\}$$

$$- \int_{t_6}^{t} \gamma G_X x\, dt$$

$$= (-1)^{E-1}\ \gamma G_{X1} x(t_3 - t_2) + \sum_{k=1}^{E-1} (-1)^{k-1}[\gamma G_X x(t_8 - t_6) + \gamma G_{X2} x(t_9 - t_8)] - \gamma G_X x(t - t_6).$$

(3.37)

However, the 2DFT NMR pulse sequence is adjusted so as to reduce ϕ_X to zero at the center of the Eth acquisition period, allowing the above expression to be reduced to

$$\phi_X = -\gamma G_X x t = -\omega_X x. \tag{3.38}$$

The final expression for the data matrix obtained from 2DFT NMR imaging is

$$s(\omega_X,\omega_Y) = \int\int m(x,y) \exp[i(\phi_Z + \phi_Y + \phi_X)]\, dx\, dy$$

$$= \int\int m(x,y) \exp\{-i[\omega_X x + \omega_Y([-1]^{E-1} y)]\}\, dx\, dy. \tag{3.39}$$

Inverse Fourier transforming the above gives us the final image $\hat{m}(x,y)$ as

$$\hat{m}(x,y) = m(x,\pm y), \tag{3.40}$$

where the plus and minus signs apply to the odd and even numbered echoes, respectively.

3.2.2.2 Pulsatile Flow Normal to the Slice

For pulsatile flow normal to the slice, only the z coordinate of a spin packet varies with time. Assuming that negligible change in motion occurs during a projection, the z coordinate of this spin packet's magnetization may be described by

$$z(t) = z + [V_Z + A_Z \sin(\Omega t')]\,[t - t_1 + (E-1)T_E]. \tag{3.41}$$

Then, this magnetization's phase evolution, due to the z gradient, is expressed as

$$\phi_Z = (-1)^{E-1}\left[\int_{t_1-(E-1)T_E}^{t_2-(E-1)T_E} \gamma G_{Z1}\{z+[V_Z+A_Z\sin(\Omega t')][t-t_1+(E-1)T_E]\}\,dt - \int_{t_3-(E-1)T_E}^{t_4-(E-1)T_E} \gamma G_{Z2}\{z+[V_Z+A_Z\sin(\Omega t')][t-t_1+(E-1)T_E]\}\,dt\right] \tag{3.42}$$

After evaluating the above expression and noting that the static terms cancel, the result is

$$\phi_Z = \phi_{ZV} + \phi_{ZA}\sin(\bar{Y}\omega_Y + \Omega n t_r) \tag{3.43}$$

where

$$\phi_{ZV} = (-1)^{E-1}\frac{V_Z}{2}[\gamma G_{Z1} t_Z^2 - 2\gamma G_{Z2} t_Y (T_Y + \frac{t_Y}{2})]$$
$$\phi_{ZA} = (-1)^{E-1}\frac{A_Z}{2}[\gamma G_{Z1} t_Z^2 - 2\gamma G_{Z2} t_Y (T_Y + \frac{t_Y}{2})]. \tag{3.44}$$

Incorporating the expression for ϕ_Z into that for the acquired signal, and simplifying in a manner similar to that used in section 3.2.1, we obtain the result

$$s(\omega_X,\omega_Y) = \exp[i\phi_{ZV}]\sum_{p=-\infty}^{\infty} K_p\, F\{m[x,\pm(y+p\bar{Y})]\} \tag{3.45}$$

where

$$K_p = \exp[ip\Omega n t_r]\, J_p[\,\phi_{ZA}\,]. \tag{3.46}$$

Notice that for E = 1, these expressions reduce to those derived for first-echo images (section 3.2.1.1). The final image $\hat{m}(x,y)$ is expressed as

$$\hat{m}(x,y) = \exp[i\phi_{ZV}]\sum_{p=-\infty}^{\infty} K_p\, m[x,\pm(y+p\bar{Y})]. \tag{3.47}$$

Comparinson of equation 3.47 with equation 3.14 shows that the effect of pulsatile flow normal to the slice on higher echo images is almost identical to that for the first echo image.

3.2.2.3 Pulsatile Flow along the Phase-Encoding Direction

In the case where the flow of spins is in the phase-encoding direction, only the y coordinate of an elemental volume of spins is time-dependent. Neglecting any change in motion during a projection, the value of the y coordinate takes the form

$$y(t) = y + [V_Y + A_Y \sin(\Omega t')]\,[t - t_1 + (E-1)T_E]\,. \tag{3.48}$$

The phase contribution due to the y gradient at the Eth acquisition period is calculated by evaluating

$$\phi_Y = (-1)^{E-1}\left\{ -\int_{t_5 - (E-1)T_E}^{t_6 - (E-1)T_E} \gamma G_Y\{y + [V_Y + A_Y \sin(\Omega t')][t - t_1 + (E-1)T_E]\}\, dt \right\}. \tag{3.49}$$

Including the result of this evaluation into the expression for the image data matrix and simplifying yields

$$s(\omega_X, \omega_Y) = \sum_{p=-\infty}^{\infty} K_p(\omega_Y)\, F\{m[x, \pm(y - \hat{y} + p\bar{Y})]\} \tag{3.50}$$

where

$$K_p(\omega_Y) = \exp[(-1)^{E-1} ip\Omega n t_r]\, J_p(\tilde{y}\omega_Y) \tag{3.51}$$

$$\hat{y} = V_Y\left(T_Y + \frac{t_Y}{2}\right)$$

$$\tilde{y} = -A_Y\left(T_Y + \frac{t_Y}{2}\right).$$

Note that for E = 1 the above equation reduces to the results of section 3.2.1.2. Calculation of the final image $\hat{m}(x,y)$ proceeds in the normal fashion giving

$$\hat{m}(x,y) = \sum_{p=-\infty}^{\infty} F^{-1}[K_p(\omega_Y)] * m[x,\pm(y - \hat{y} + p\bar{Y})] \tag{3.52}$$

where

$$F^{-1}[K_p(\omega_Y)] = \exp[ip\Omega nt_r]\,\delta(x)\,\frac{(-i)^p T_p(\frac{-\dot{y}}{\tilde{y}})}{\sqrt{\tilde{y}^2 - y^2}} \quad ; y^2 < \tilde{y}^2$$
$$= 0 \quad ; y^2 \geq \tilde{y}^2. \tag{3.53}$$

The artifacts in higher echo images, due to flow in the phase-encoding direction, are virtually identical to those of the first echo image.

3.2.2.4 Pulsatile Flow along the Read-Encoding Direction

For flow along the read-encoding direction only, the x coordinate of a voxel's magnetization may be written as

$$x(t) = x + [V_X + A_X\sin(\Omega t')][t - t_1 + (E-1)T_E], \tag{3.54}$$

if any change in motion during a projection is neglected. The contribution of the x-gradient pulses to the phase of this magnetization is

$$\phi_X = (-1)^{E-1}\int_{t_2-t_1}^{t_3-t_1}\gamma G_{X1}\{x+[V_X A_X\sin(\Omega t')]t\}dt$$
$$+\sum_{k=1}^{E-1}(-1)^{k-1}\left|\begin{array}{l}\displaystyle\int_{t_8-t_1+(E-1-k)T_E}^{t_9-t_1+(E-1-k)T_E}\gamma G_X\{x+[V_X A_X\sin(\Omega t')]t\}dt\\ \displaystyle+\int_{t_8-t_1+(E-1-k)T_E}^{t_9-t_1+(E-1-k)T_E}\gamma G_{X2}\{x+[V_X A_X\sin(\Omega t')]t\}dt\end{array}\right|$$
$$-\int_{t_6-t_1+(E-1)T_E}^{t-t_1+(E-1)T_E}\gamma G_X\{x+[V_X A_X\sin(\Omega t')]t\}dt\ . \qquad (3.55)$$

Adjustment of the pulse sequence assures that the phase contribution of the static terms is zero at the center of the Eth acquisition period, therefore the above expression reduces to

$$\phi_X = \phi_{XV} - \omega_X(x+\hat{x}) - \frac{V_X}{2\gamma G_x}\omega_X^2 + \frac{A_X}{2}K(\omega_X)\sin(\bar{Y}\omega_Y + \Omega n t_r)\ , \qquad (3.56)$$

where

$$\phi_{XV} = \frac{V_X}{2}(K_{XA} - K_{XB})$$
$$K_{XA} = (-1)^{E-1}\gamma G_{X1}[(t_3-t_1)^2 - (t_2-t_1)^2]$$
$$+\sum_{k=1}^{E-1}(-1)^{E-1}\left|\begin{array}{l}\gamma G_X\{[t_8-t_1+(E-1-k)T_E]^2 - [t_6-t_1+(E-1-k)T_E]^2\}\\ +\gamma G_{X2}\{[t_9-t_1+(E-1-k)T_E]^2 - [t_8-t_1+(E-1-k)T_E]^2\}\end{array}\right|$$
$$K_{XB} = \gamma G_X[T_{XE}t_X + \frac{t_X^2}{4}] \qquad (3.57)$$
$$\hat{x} = V_X[T_{XE} + \frac{t_X}{2}]$$
$$T_{XE} = (E-1)T_E + T_X$$
$$t_X = t_8 - t_6$$
$$K(\omega_X) = K_{XA} - K_{XB} - [\frac{\omega_X^2}{\gamma G_X} + 2(T_{XE} + \frac{t_X}{2})\omega_X\ ].$$

Incorporating the above expression into the equation for the acquired signal, we obtain

$$s(\omega_X,\omega_Y) = \exp(i\phi_{XV}) \sum_{p=-\infty}^{\infty} K'(\omega_X)\, K_p(\omega_X)\, F\{m[x-\hat{x},\pm(y+p\bar{Y})]\} \tag{3.58}$$

where

$$K'(\omega_X) = \exp\left[-i\frac{V_X}{2\gamma G_X}\omega_X^2\right]$$
$$K_p(\omega_X) = \exp[ip\Omega n t_r]\, J_p\left[\frac{A_X}{2} K(\omega_X)\right]. \tag{3.59}$$

The final image, calculated in the same manner as before, is

$$\hat{m}(x,y) = \exp(i\phi_{XV}) \sum_{p=-\infty}^{\infty} F^{-1}[K'(\omega_X)] * F^{-1}[K_p(\omega_X)] * m[x-\hat{x},\pm(y+p\bar{Y})]. \tag{3.60}$$

For pulsatile flow in the read direction, artifacts in higher echo images are similar to those for first echo image. However, note that the shift of the flowing voxels in the principal and ghost structures ($\hat{x}$) is dependent on the echo number (E) and will be different for each echo image. For typical flow and imaging parameters, $\hat{x}$ can approach one centimeter for the eighth-echo image. The blurring of the ghosts will also differ for the various echo images.

3.3 Suppression of Pulsatile Flow Artifacts

The data matrix $[s(\omega_X,\omega_Y)]$ obtained from 2DFT NMR imaging is the two-dimensional spatial Fourier transform of the magnetization distribution m(x,y) within a slice: x and y represent the direction of frequency and phase encoding, respectively, with ω_X and ω_Y being the corresponding frequency variables. The data collected during projections (or views) are used to fill in the rows of this matrix. Each row of the data matrix is associated with a fixed value of ω_Y. The matrix is usually filled on a row-by-row basis, starting with the row associated with the most negative value of ω_Y and monotonically incrementing ω_Y by a fixed amount. Data for any given row are collected over a time span of approximately ten milliseconds, during which physiological motion

may be considered negligible. The time between the collection of adjacent rows of data is the repetition time, t_r, during which significant motion can occur.

The monotonic manner in which rows of the data matrix $s(\omega_X,\omega_Y)$ are filled establishes a linear correspondence between physical time and the spatial frequency variable ω_Y. Therefore, the coordinates describing the location of spins that either move periodically or flow in a pulsatile fashion become periodic functions of ω_Y. Ghosting artifacts in 2DFT NMR images are a result of the periodicity of this motion with ω_Y. Most artifact suppression techniques attempt to defeat the ghosting artifacts by seeking to eliminate the periodicity of the motion with ω_Y.

To see in greater detail how synchronization removes ghosting artifacts due to pulsatile flow, let us consider the x, y and z coordinates of an elemental volume of spins. When the imaging pulse sequences are unsynchronized to the pulsatile flow, these coordinates are described by equations 3.41, 3.48, and 3.54. In these equations the coordinates depend on t' which in turn depends upon G_Y. Recalling the proportionality between ω_Y and G_Y, it is evident that x(t), y(t) and z(t) are periodic functions of ω_Y. The periodicity of this motion leads to ghosting.

However, if the imaging sequence is synchronized to the cardiac cycle, then equation 3.41, 3.48, and 3.54 may be modified to read

$$\begin{aligned} x(t) &= x + [V_X + A_X\sin(\theta)][t - t_1 + (E\text{-}1)T_E], \\ y(t) &= y + [V_Y + A_Y\sin(\theta)][t - t_1 + (E\text{-}1)T_E], \\ z(t) &= z + [V_Z + A_Z\sin(\theta)][t - t_1 + (E\text{-}1)T_E]; \end{aligned} \tag{3.54}$$

where θ represents the phase of the motion. Notice that in the above equations, x(t), y(t) and z(t) are no longer functions of ω_Y. These equations may be reduced to

$$x(t) = x + [V'_X][t - t_1 + (E-1)T_E],$$
$$y(t) = y + [V'_Y][t - t_1 + (E-1)T_E], \quad (3.55)$$
$$z(t) = z + [V'_Z][t - t_1 + (E-1)T_E],$$

where

$$V'_X = V_X + A_X\sin(\theta),$$
$$V'_Y = V_Y + A_Y\sin(\theta), \quad (3.56)$$
$$V'_Z = V_Z + A_Z\sin(\theta).$$

Equations 3.55 are similar to equations 3.41, 3.48, and 3.54 if we interpret V'_X, V'_Y and V'_Z as representing the constant components of the velocity terms and the amplitude of the oscillating components as zero. In the analysis presented in the previous sections, it was noted that if the amplitude of the oscillating velocity components (A_X, A_Y or A_Z) was zero (steady flow), then no ghosting occurred. Synchronization of the imaging sequence will therefore make the pulsatile flow appear to be steady . There will be no ghosting, and blurring will be present only for flow along the read direction. Voxels whose contents flow in the phase or read directions will also be translated by $\hat{x}$ or $\hat{y}$ in the image. Recall that $\hat{x}$ was dependent upon the echo number E, so that the blurred image of a packet of flowing spins is expected to be at a different location in higher echo images compared to the first echo image.

Fig. 3.5 summarizes the artifacts expected in 2DFT NMR imaging of flowing spins. The sketches portrayed in Fig 3.5 represent modulus images of a single voxel located at the origin. In Fig 3.5A, the spins of the voxel are stationary and the image contains no artifacts. For flow normal to the slice of the plane, steady flow and synchronized imaging result in no artifacts (Fig 3.5B), while unsynchronized imaging results only in ghosting (Fig 3.5C) in the phase-encoding direction. When the flow is in the phase-encoding

direction, steady flow or synchronized imaging result only in the translation of the voxel by $\hat{y}$ in the image (Fig 3.5D), while unsynchronized imaging results not only in this translation, but also in blurring and ghosting in the phase-encoding direction (Fig 3.5E). Lastly, for flow along the read-encoding direction, steady flow and synchronized imaging result in translation of the voxel by $\hat{x}$ and some blurring both of which are in the read direction (Fig 3.5F). Unsynchronized imaging shows a shifting of the voxel by $\hat{x}$, additional blurring in the read direction, and ghosting of these structures in the phase-encoding direction (Fig 3.5G).

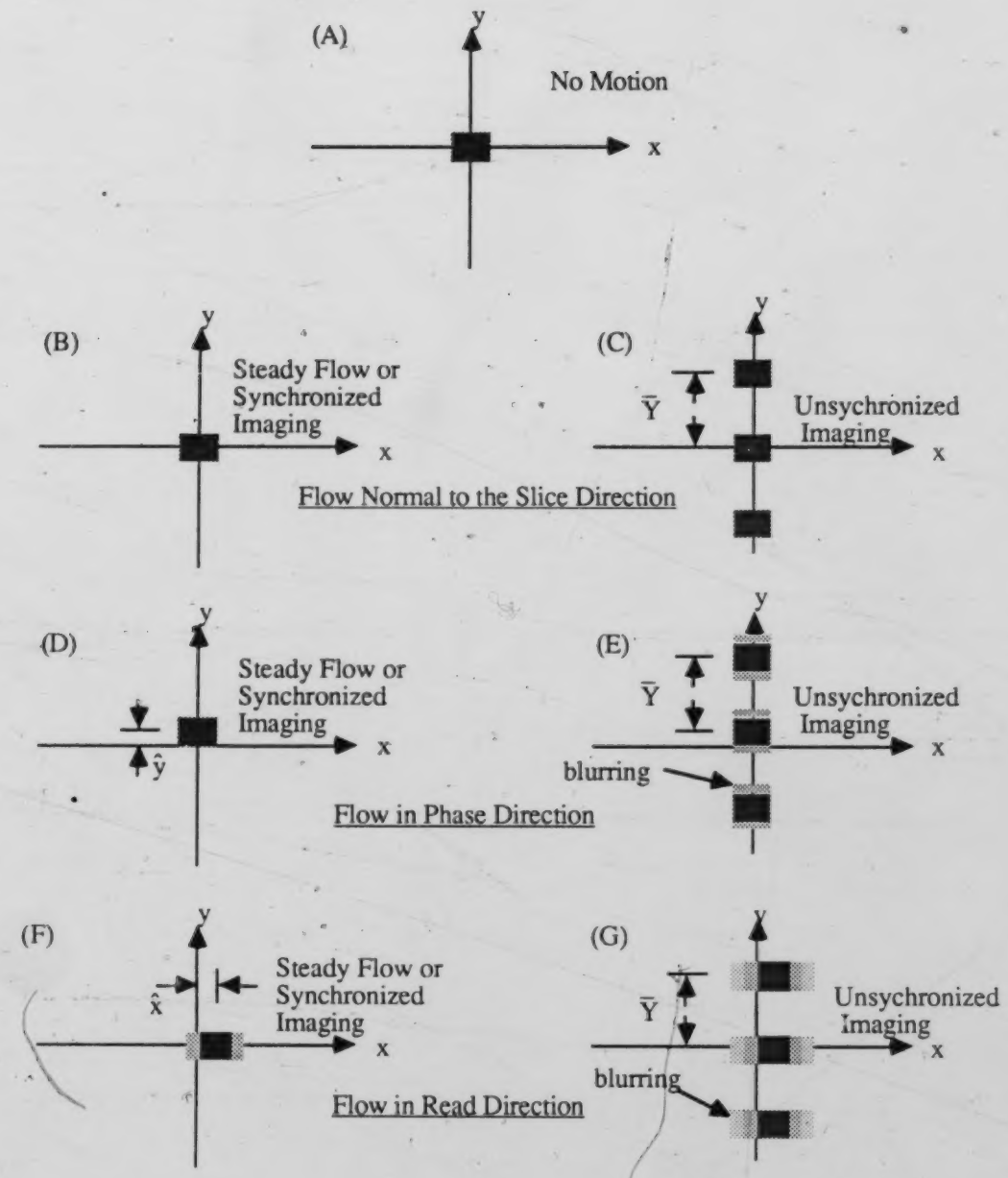

Figure 3.5 Diagrammatic representations of unsynchronized and synchronized modulus images of a voxel experiencing steady or pulsatile flow in each of the three Cartesian directions. In (A) voxel is stationary; (B) and (C) indicate the effect of flow normal to the slice plane. The effect of flow in the phase and read directions are illustrated in (D) and (E), and (F) and (G), respectively. In (C), (E), and (G) only the first order ghosts ($p = \pm 1$), caused by unsynchronized imaging to pulsatile flow, are shown.

CHAPTER 4

CARDIAC SYNCHRONIZATION AND RESPIRATORY GATING SYSTEMS

4.1 Introduction

Reduction of pulsatile blood-flow and cardiac-motion artifacts requires the imaging pulse sequence to be synchronized to the cardiac cycle (Lanzer et al., 1984; Van Dijk, 1984a, b). Similarly, respiratory-motion artifacts can be significantly reduced if the acquisition of image data is gated to a quiescent portion of the respiratory cycle (Lewis et al., 1986; Wood & Henkelman, 1986a). In order to provide the capacity for gating and synchronization, systems capable of measuring the ECG and respiration signals of a subject placed in the magnet bore during an imaging experiment were developed and constructed. It was imperative that these systems not degrade the NMR magnet bore environment. To prevent degrading of the $\mathbf{B}_0$ homogeneity, no ferromagnetic materials were to be introduced into the magnet bore. The quantity and size of metallic components placed in the magnet bore were minimized to prevent compromising the $\mathbf{B}_1$ homogeneity of the RF imaging coil. Lastly, the integrity of the RF isolation between the magnet bore and its surroundings had to be maintained. For reasons of efficacy, economy, and convenience, it was decided to use fiber-optic data-links to transmit the ECG and respiration signals from the vicinity of the magnet to the spectrometer console. The implementation of the ECG synchronization and respiratory gating systems, the multiplexing system required for gated, synchronized, or gated and synchronized imaging, and the pulse-program flow diagram are detailed in this chapter.

4.2 Respiratory Gating System

For respiratory gated acquisitions, it was necessary to design and build a system that would measure the movement of the chest or abdomen due to breathing, and at the same time not degrade the NMR environment inside the magnet bore. The respiratory gating system consists of a rubber bellows connected to a short length of Tygon tubing, a battery powered transmitter unit located inside the screened magnet enclosure, and a receiver unit placed near the spectrometer console (Fig. 4.1). The respiratory signal is transmitted to the receiver unit through a fiber-optic (F/O) cable. Use of the F/O data-link between the transmitter and receiver units prevents the introduction of RF noise into the magnet bore by the respiratory gating system. The bellows and Tygon tubing avoid the use of metallic objects inside the magnet bore.

Figs. 4.1 and 4.2A detail the block and circuit diagrams, respectively, of the respiratory transmitter unit. The bellows is strapped to an animal's chest or abdomen; respiratory motion produces pressure fluctuations inside the bellows that are transmitted along the Tygon tubing to the pressure transducer. This transducer converts these fluctuations into an electrical signal which is amplified and directed to a voltage-to-frequency (V/F) converter whose output drives the F/O transmitter. The block and circuit diagrams of the respiratory receiver unit are shown in Figs. 4.1 and 4.2B, respectively. The F/O receiver converts the light pulses into an electrical signal which is then sent to a frequency-to-voltage (F/V) converter. Next, the reconstructed respiratory signal, after passing through a buffer amplifier, is directed to a gating circuit. In this circuit, the respiratory signal is split into two channels. The circuit is designed such that the signal in the first channel is positive with respect to the signal in the second channel during the inspiration part of the respiratory cycle. During the remainder of the respiratory cycle, the second channel's signal is positive with respect to the first channel's signal. Signals from

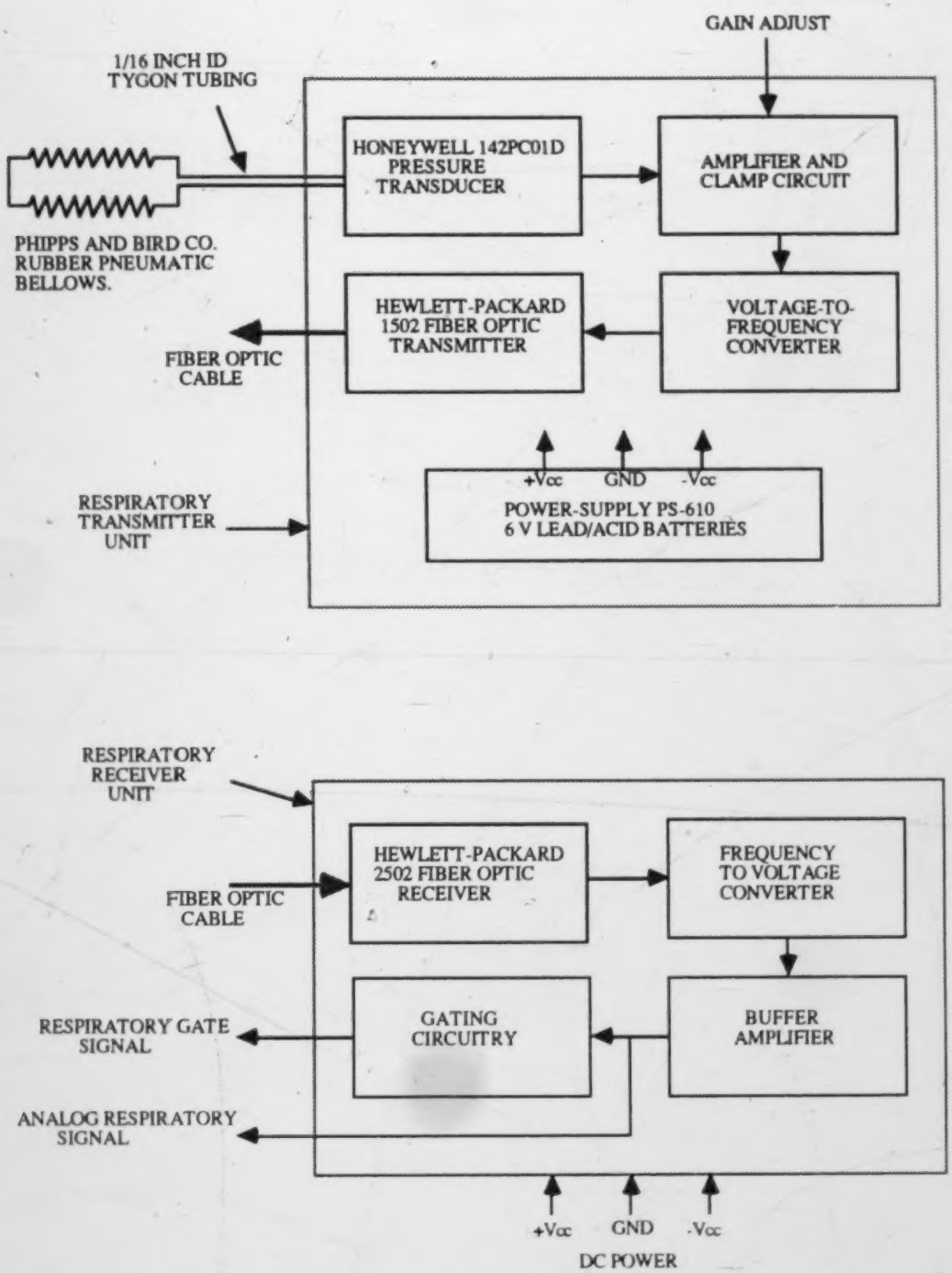

Figure 4.1 Block diagram of the respiratory gating system.

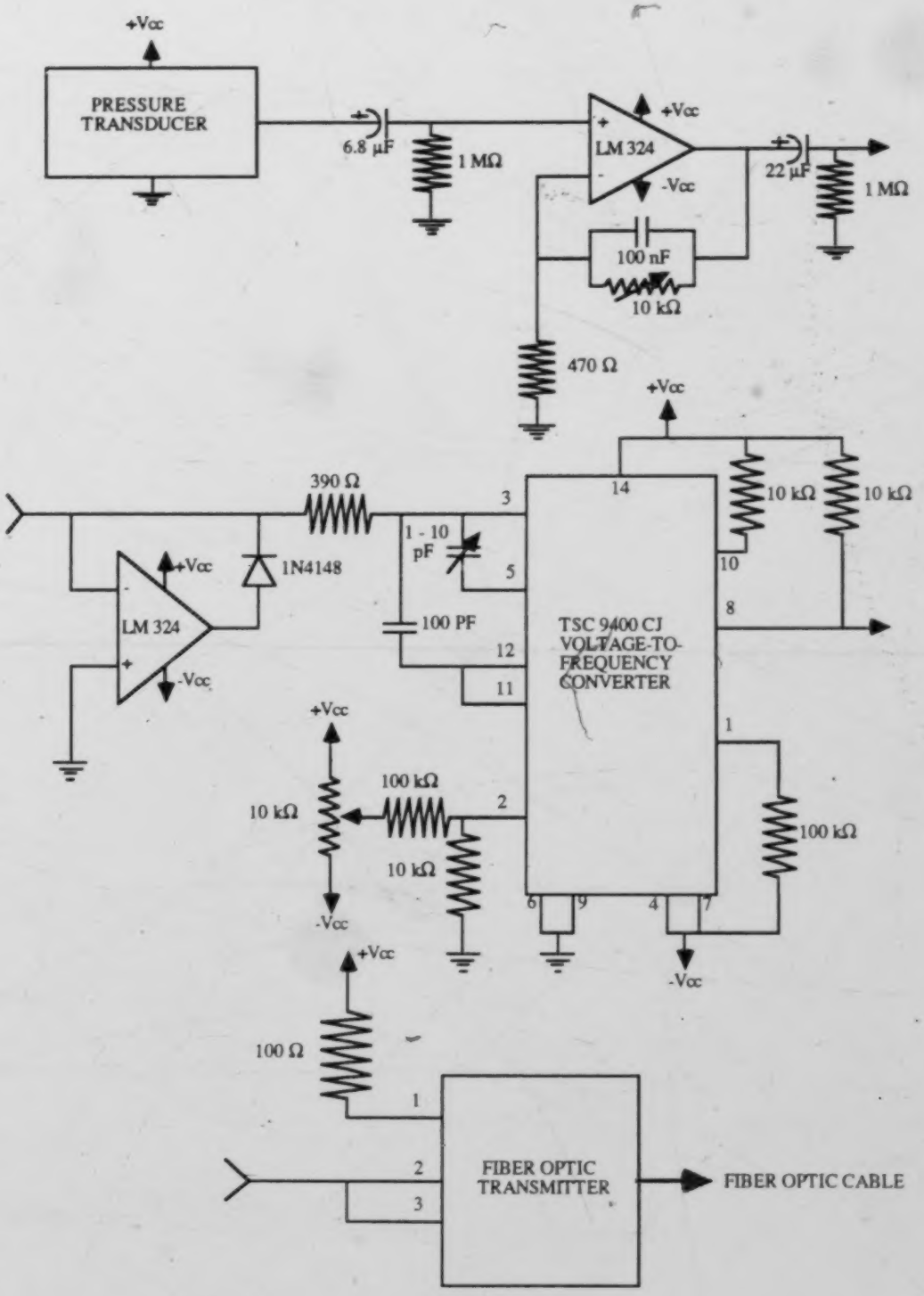

Figure 4.2 A Respiratory transmitter unit circuit diagram.

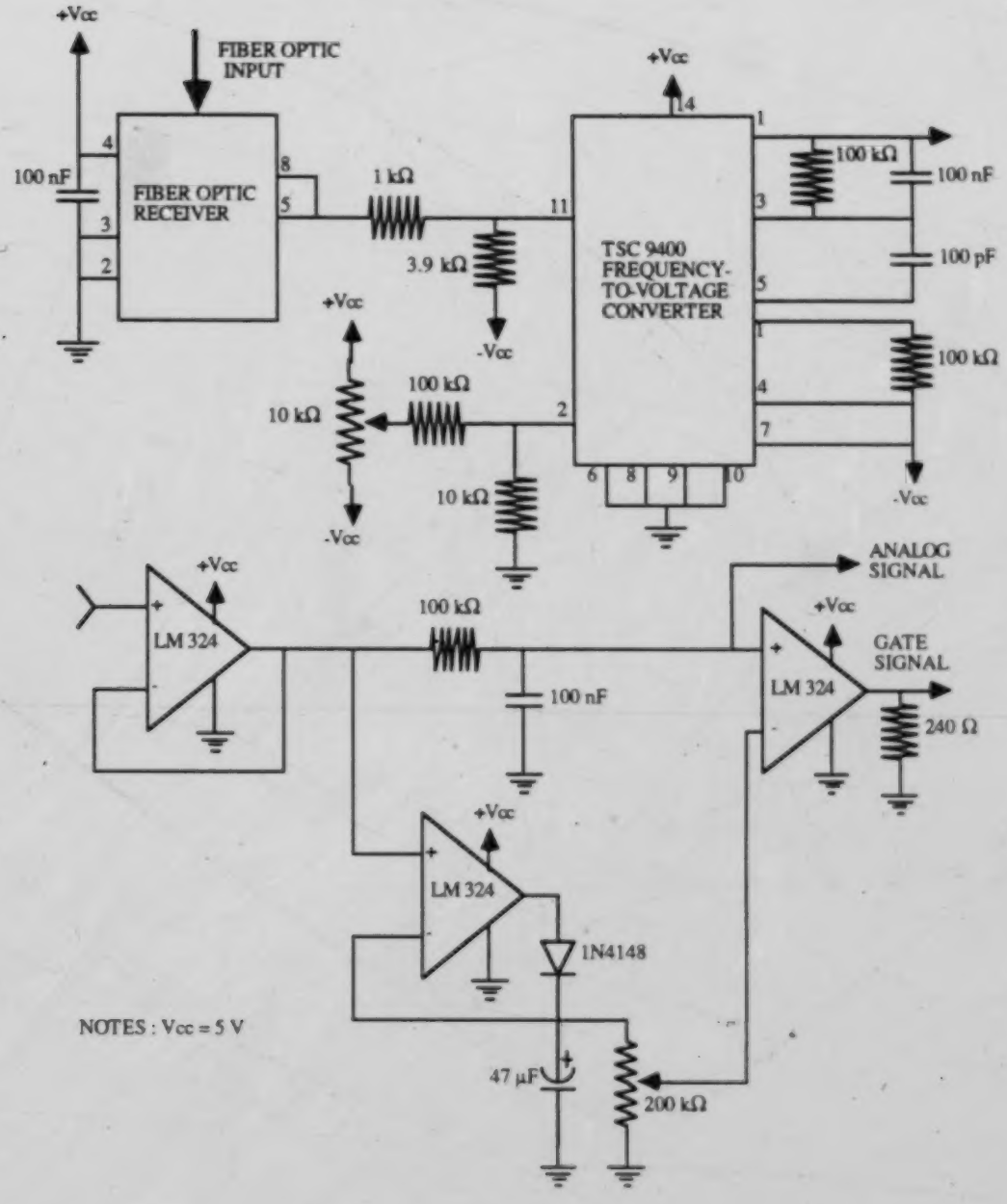

Figure 4.2B Respiratory receiver unit circuit diagram.

these two channels then go to a comparator, whose output constitutes the respiratory gating signal.

4.3 ECG Synchronization System

In order to perform ECG synchronized imaging, a system that is capable of producing the ECG of a subject during an NMR imaging experiment is required. Ideally, the system should not degrade the NMR environment inside the magnet bore. Similar to the respiratory gating system, the ECG synchronization system designed consists of a battery-powered transmitter unit placed inside the screened magnet enclosure and a receiver unit located near the spectrometer console (Fig. 4.3). The F/O data-link between the transmitter and receiver units prevents the coupling of RF noise into the magnet bore by the ECG synchronization system. Use of non-magnetic ECG electrodes, small brass connectors, and non-metallic ECG leads minimizes the amount of metal placed inside the magnet bore.

During the development of this synchronization system, four factors were found to degrade the ECG signal: ECG lead vibrations in the large static magnetic field, the switched magnetic field gradients, the enhanced T-wave height, possibly caused by a Hall effect emf due to blood flow within the static magnetic field (Dimick et al., 1987), and the pulsed RF field. The low-frequency noise due to ECG lead vibrations was eliminated by judicious placement and restraint of the leads. Artifacts caused by the switching magnetic field gradients did not compromise the system's ability to synchronize and were therefore neglected. Filtering was used in the ECG triggering circuitry to suppress the enhanced T-wave height. However, the large-amplitude RF pulses (rectangular 90° and 180°) saturated and disabled the ECG preamplifier for up to several seconds. This effect prevented synchronization of the system to each heartbeat. Lossy transmission line conductors were introduced instead of the normal metallic ECG leads to suppress this RF

interference (Damji et al., 1988). A twin-lead lossy transmission line was used to connect the active (right-arm and right-leg) ECG electrodes to the transmitter unit. In order to reduce the 60 Hz common-mode input voltage to the transmitter preamplifier, a lossy line conductor was used to connect the left-leg electrode to the ECG transmitter unit ground. The lossy line acts as a distributed RC network that severely attenuates RF signals while passing the low-frequency ECG signal. The highly resistive lossy transmission line conductors necessitated the use of a high-input-impedance (FET-input) preamplifier.

The block and circuit diagrams of the ECG transmitter unit are presented in Figs. 4.3 and 4.4A, respectively. Lossy transmission line conductors are used to connect three ECG electrodes placed on a subject to a battery-powered FET-input ECG preamplifier housed inside the transmitter unit. The amplified ECG signal is then converted to an optical signal by a F/O transmitter.

Figs. 4.3 and 4.4B show the block and circuit diagrams of the ECG receiver unit, respectively. The F/O receiver converts the optical signal to its electrical counterpart, which may then pass through a sharp 60 Hz notch filter to remove any power-line noise in the ECG. Next, the filtered ECG is directed to the triggering circuitry. The ECG T-wave contains lower frequencies than those of the QRS complex, so a high-pass filter is used to suppresses the enhanced T-wave while allowing the QRS complex signal to pass relatively unattenuated. The resulting signal is compared to an adjustable dc voltage and the output of the comparator is sent to a TTL one-shot circuit to produce a fixed-duration ECG trigger pulse.

4.4 Combined Cardiac Synchronization and Respiratory Gating System

To obtain images that were cardiac synchronized, respiratory gated, or both, it was necessary to present both the cardiac trigger and respiratory gate signals to the NMR spectrometer. However, the ASPECT 3000 minicomputer used by the Bruker CXP 100

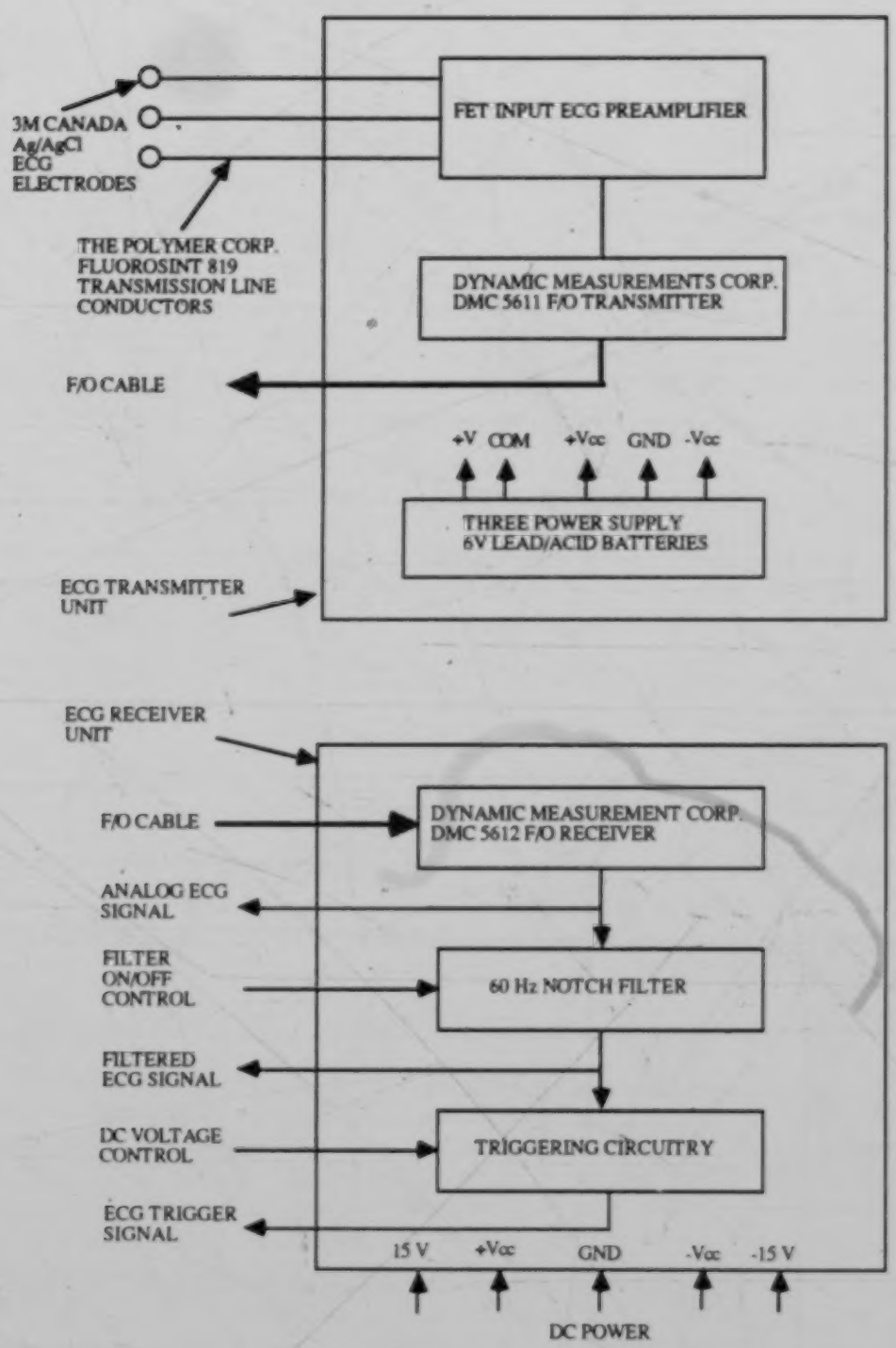

Figure 4.3 Block diagram of ECG synchronization system.

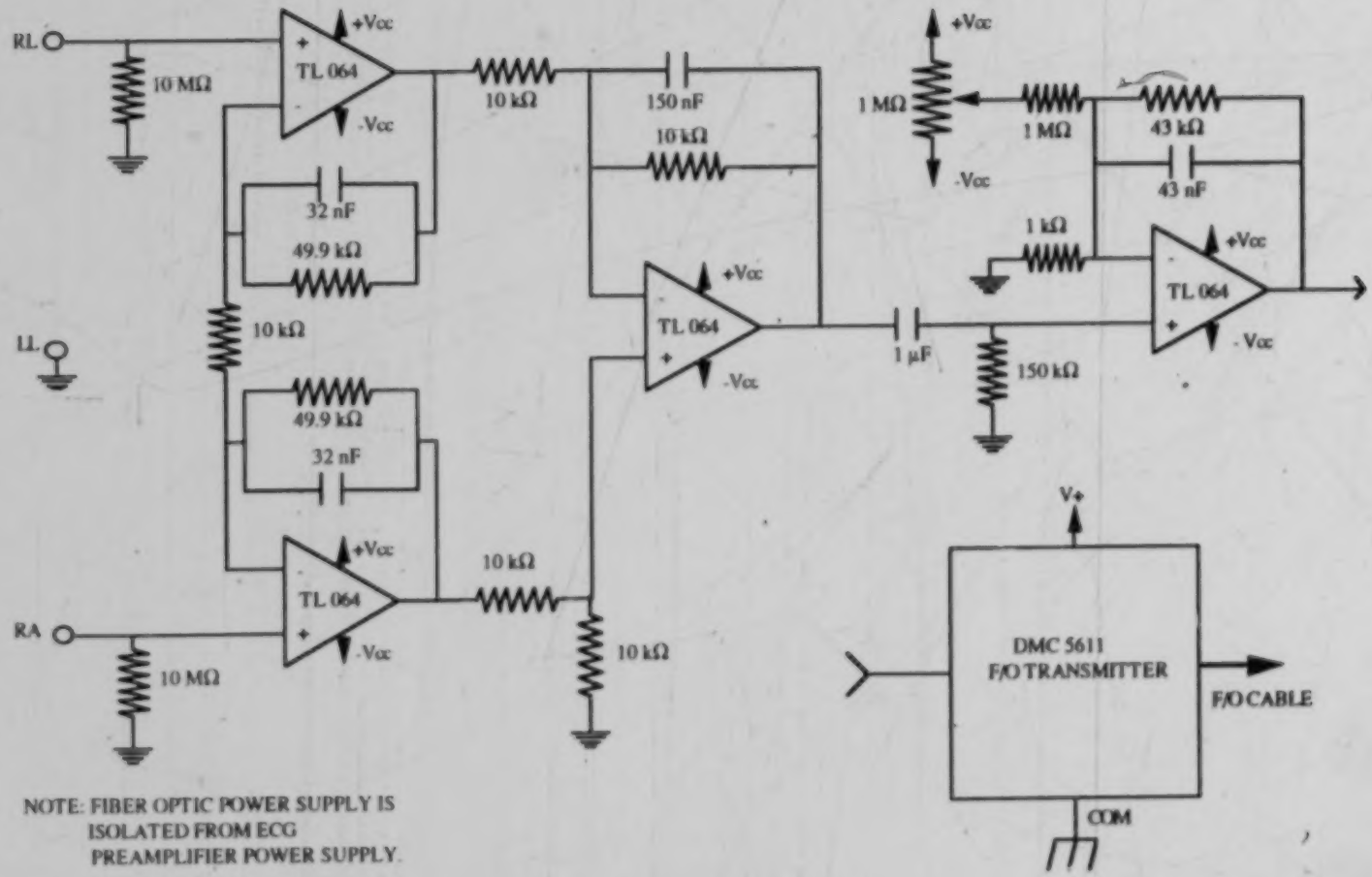

Figure 4.4A ECG transmitter unit circuit diagram.

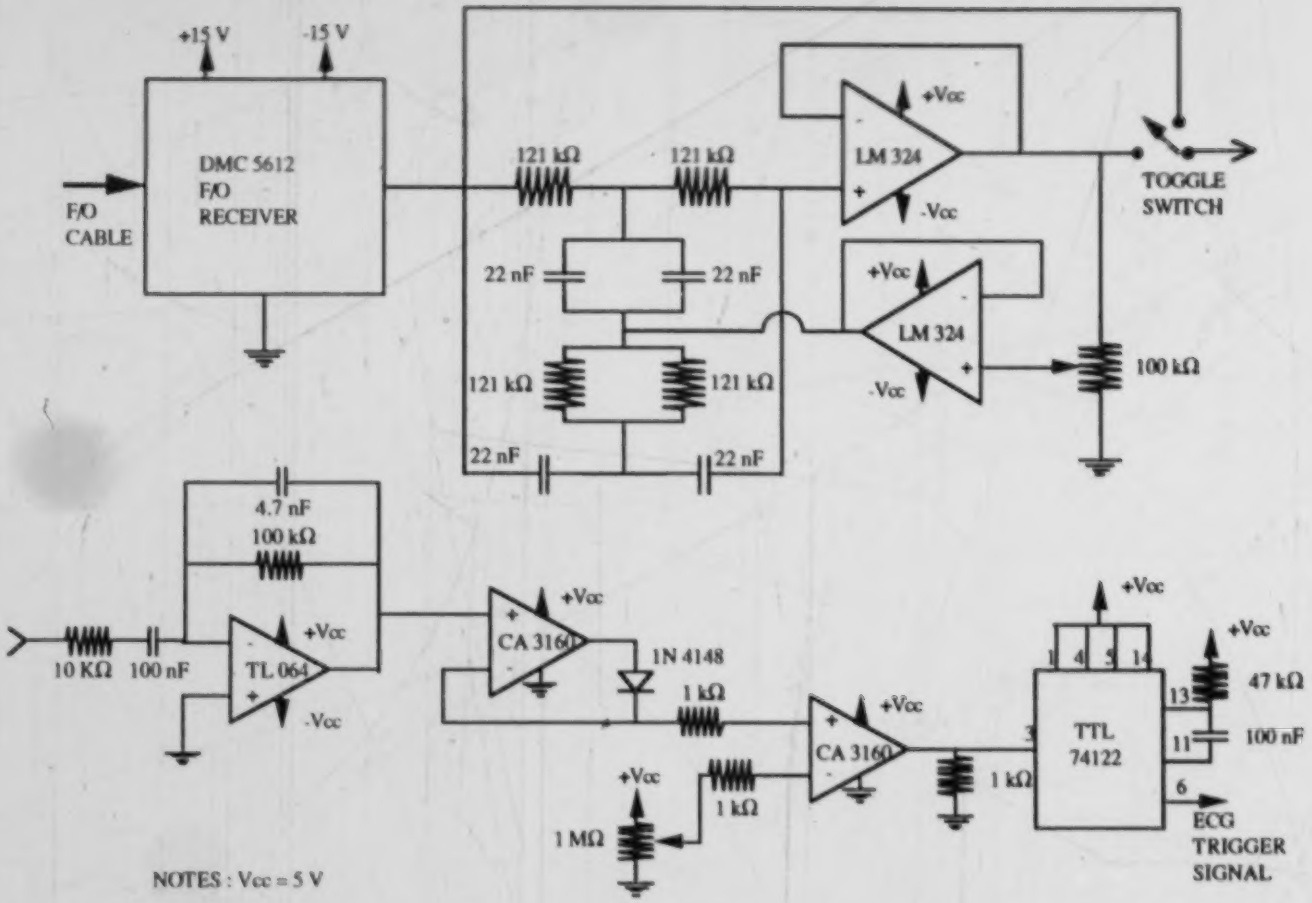

Figure 4.4B ECG reciever unit circuit diagram

spectrometer has only one TTL input line, although it has several TTL output lines. A scheme to multiplex the cardiac trigger and respiratory gate signals onto the single input line of the spectrometer was required. The complete cardiac synchronization and respiratory gating system is illustrated in Fig. 4.5. A pulse issued by the spectrometer to the 'ECG enable' control line of the multiplexer unit causes this unit to route the ECG trigger signal to its output. Likewise, a pulse to the 'respiratory enable' control line causes the respiratory gate signal to appear at the unit's output. The 'ECG enable' and 'respiratory enable' pulses are connected to the set (S) and reset (R) input of an SR flip-flop, respectively, and the output of the flip-flop controls the multiplexer chip's control lines. Thus, the output state of the flip-flop controls which multiplexer input will be routed to the output. In Fig 4.6, the detailed circuit diagram for the multiplexer unit is given.

It was necessary to alter the pulse program normally used for 2DFT NMR imaging to accommodate for synchronized, gated, or synchronized and gated imaging. The flow diagram of the resulting pulse program is shown in Fig 4.7. If the acquisition is to be triggered by the ECG waveform, the multiplexer unit is commanded to transmit the ECG trigger signal to the CXP input line. This input line is then polled until a trigger pulse occurs, after which the program remains idle for a time called the ECG delay. The ECG delay is used to allow the imaging pulse sequence to start at any phase of the cardiac cycle. After this delay, the multiplexer unit is instructed to transmit the respiratory gate signal if the acquisition is also to be gated. The CXP input line is polled again: if the respiratory gate signal is in the appropriate state, a normal imaging scan is acquired, otherwise a dummy scan during which no data collection takes place is executed. It should be noted that the dummy scan consists of only the RF pulses of the normal imaging pulse sequence. Using such dummy scans insures that the same degree of relaxation occurs for all projections. This method of maintaining the dynamic equilibrium of the magnetization is called spin-conditioning (Ehman et al., 1984). After completion of either the normal or

dummy scan, the program waits a minimum period (relaxation delay) to allow for relaxation. The pulse sequence repetition time, t_r, will be the smallest multiple of the cardiac period that is longer than the sum of the relaxation delay and the pulse sequence duration.

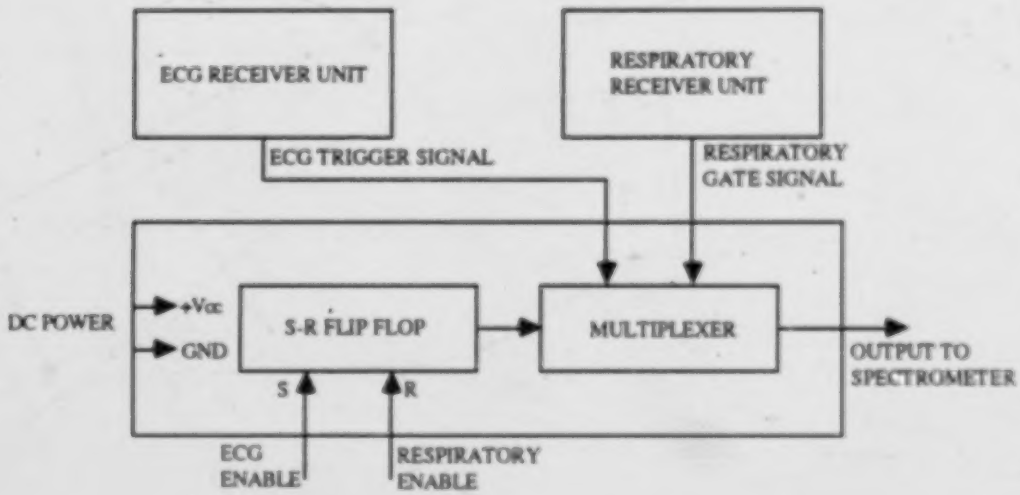

Figure 4.5 Block diagram representation of synchronization/gating system.

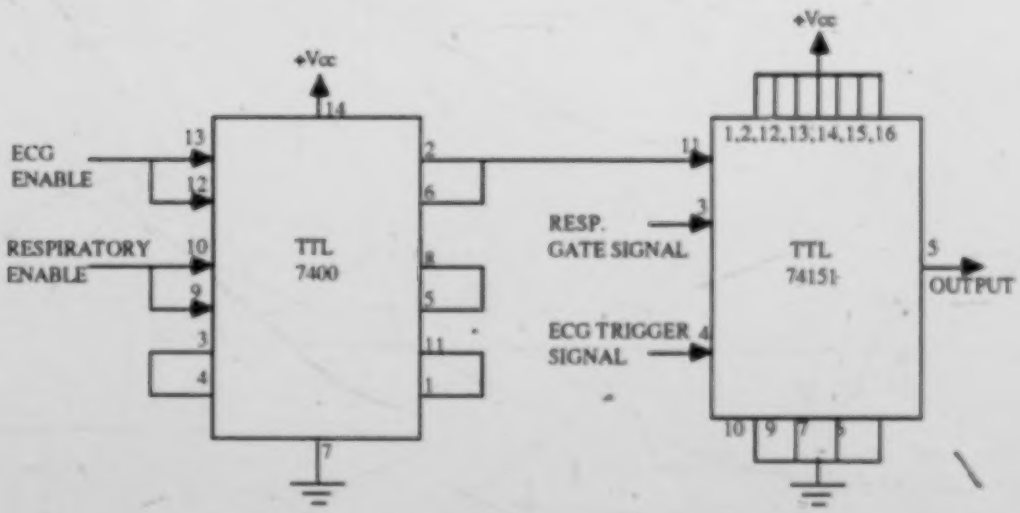

NOTES : Vcc = 5 V

Figure 4.6 Circuit diagram for multiplexer unit.

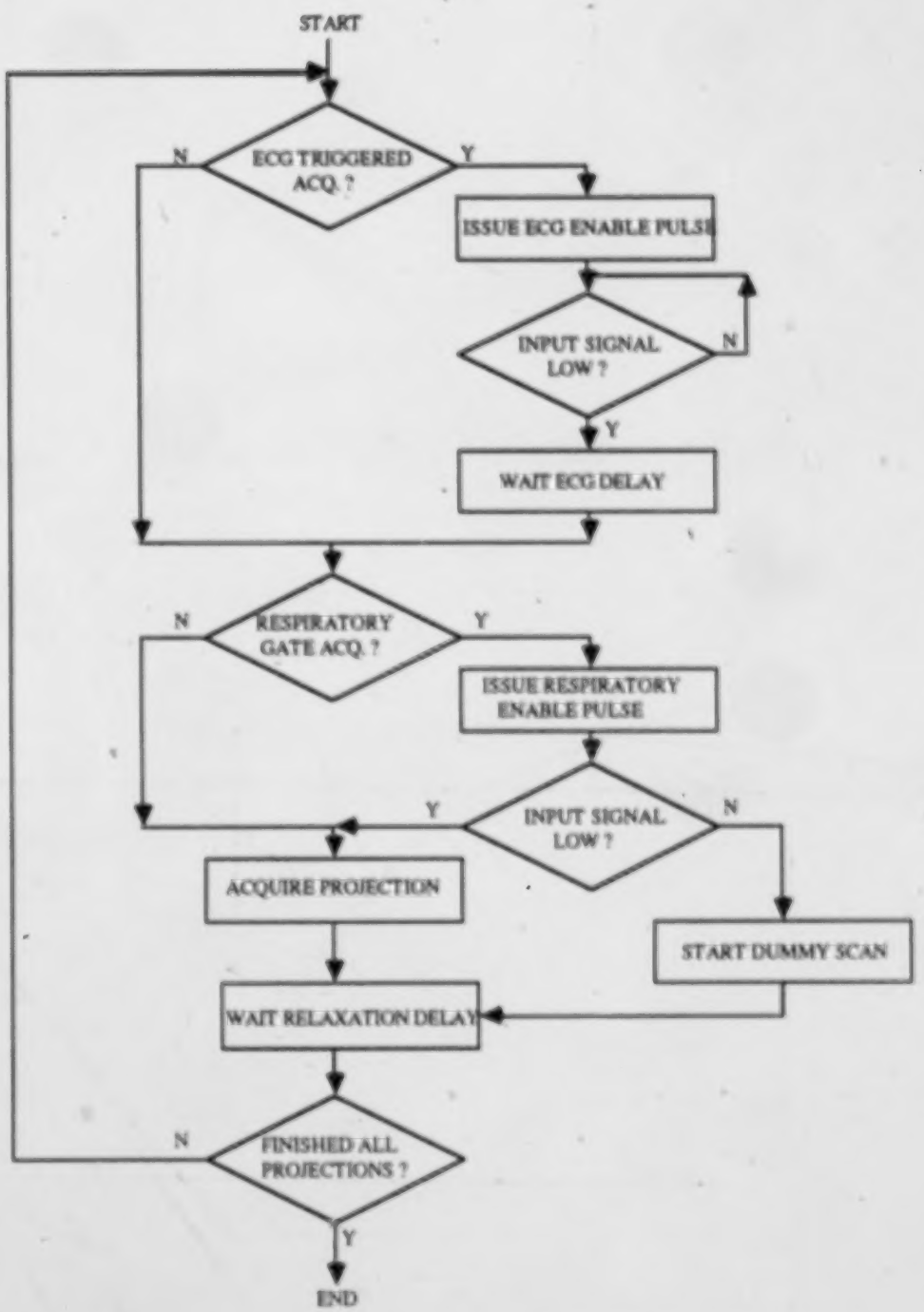

Figure 4.7 Flow diagram of pulse program used for synchronized and gated, synchronized, and gated images.

CHAPTER 5

EXPERIMENTAL RESULTS AND DISCUSSION

5.1 Introduction

This chapter presents details of phantom and animal imaging experiments and discusses the results from these experiments. Using a flow phantom, a set of experiments was conducted to confirm the presence of image artifacts (predicted in chapter 3) due to flow, and to test the effectiveness of synchronized imaging in eliminating ghost artifacts. Next, ECG synchronized images of an adult cat were acquired to evaluate the improvement in image quality due to synchronization. Despite ECG synchronized and respiratory gated data acquisition, significant artifacts were still present in the images. Further experiments identified imperfect 180° RF pulses and variation in the cardiac period during the imaging experiment as factors that contributed to the residual noise.

5.2 Image Acquisition and Reconstruction

Before the acquisition of an image, a cat or phantom was placed in the University of Alberta small animal 2.35-T 40-cm-bore magnet (Bruker Spectrospin, Karlsruhe, West Germany) such that the slice of interest was 57.0 cm from the front face of the magnet housing. The spectrometer (a modified Bruker CXP 100) utilizes an ASPECT 3000 minicomputer to control all the hardware, and to collect and process the acquired data. The spectrometer settings were optimized using a semi-automatic execution sequence. Initially, the slotted resonator RF imaging coil was tuned to 100.19 MHz, matched to 50 Ω, and the input portion of the wideband preamplifier was also tuned to 100.19 MHz. Next, using a simple pulse-acquire sequence, the main magnetic field was shimmed by maximizing the area under a FID signal while keeping the FID envelope as exponential as possible. The RF power amplifier gain and final stage tuning were adjusted to produce a 250 μs, 180°

rectangular refocussing pulse. Then, the offset and gain controls of the pulse shape modulator were set to optimize a 7.68-ms Gaussian-enveloped 90° RF pulse used in the slice-selection procedure. Lastly, the values of the software parameters for the number of echoes, relaxation and ECG delays, and number of averages were selected. To verify that all the component parts of the spectrometer were functioning properly, the central view (phase-encoding gradient disabled) of each echo image was acquired. The Fourier transform of each of these time-domain echo signals yields a projection of the spins within the slice in the read-encoding direction. If acceptable, a 128-phase-encoding-step imaging experiment, with each projection averaged twice, was started.

After completing an imaging experiment, the time-domain data file was transferred from the ASPECT 3000 minicomputer to a Digital Corp. VAX 11/750 computer. The software routine controlling the data transfer automatically converts data from the 24-bit ASPECT format to the 32-bit VAX format. This data file was arranged to form a 128 x 256 complex array of raw data for each echo image. By zero filling, each 128 x 256 raw-data array was expanded to a 256 x 256 array, and a two-dimensional complex Fourier transformation was performed on these latter arrays to yield complex image matrices. For each of the complex image matrices, the modulus of each element in the matrix was calculated with the result stored in a corresponding array of real numbers. These arrays constitute modulus images which were stored permanently in image files. A software package, developed in-house, was used to display the modulus images on a Ramtek Corp. RM 9465 graphics display system and to analyze these images in detail.

5.3 Phantom Study

The flow-phantom imaging experiments were designed to demonstrate the artifacts in 2DFT spin-echo NMR images due to flow along any one of the Cartesian axes, as evaluated analytically in chapter 3. A short summary of this work follows.

Consider a slice consisting of a matrix of elemental volumes of spins, and permit these volume elements to flow along one of the Cartesian axes such that the flow velocity has a fixed time-averaged component (V_X, V_Y, or V_Z) and a sinusoidal component (A_X, A_Y, or A_Z). Let m(x,y) represent the transverse magnetization of a volume element located in the slice at (x,y) at the instant the 90° RF pulse acts. If this volume element moves in a direction normal to the slice plane (along z axis), then its image [$\hat{m}(x,y)$] is given by (equation 3.47):

$$\hat{m}(x,y) = \exp[i\phi_{ZV}] \sum_{p=-\infty}^{\infty} K_p \, m[x,\pm(y+p\bar{Y})]. \tag{5.1}$$

For a given volume element, ϕ_{ZA} (equation 3.44) is proportional to the time-averaged flow velocity V_Z, and K_p (equation 3.46) depends on the amplitude of the sinusoidal component A_Z of the flow velocity. A stationary volume element ($V_Z = 0$, $A_Z = 0$) will result in an image without artifact, that is, $\hat{m}(x,y)$ equals m(x,y). The image of an elemental volume that experiences steady flow ($V_Z \neq 0, A_Z = 0$) is altered in phase by the factor $\exp[i\phi_{ZA}]$, which has no effect on the final modulus image. A volume element flowing in a pulsatile fashion ($A_Z \neq 0$) gives rise to ghosts repeating at intervals of $\bar{Y}$ in the phase encoding direction (y), in accordance with equation 5.1. Note that these ghosts are not blurred, and their intensity is determined by the value of the parameter K_p.

Elemental volumes flowing in the phase-encoding direction (y) image according to equation 3.52:

$$\hat{m}(x,y) = \sum_{p=-\infty}^{\infty} F^{-1}[K_p(\omega_Y)] * m[x,\pm(y - \hat{y} + p\bar{Y})], \tag{5.2}$$

where F^{-1} represents the inverse Fourier transform operator. Recall that $\hat{y}$ (equation 3.51) is proportional to the time-averaged flow velocity V_Y and is independent of the echo

number E, and that $K_p(\omega_Y)$ depends upon A_Y, the amplitude of the flow velocity's sinusoidal component. Again, an immobile volume element is imaged perfectly, and the only effect on the modulus image of a volume element that flows steadily is a shift of $\hat{y}$. Equation 5.2 shows that a volume element flowing in a pulsatile manner generates ghosts that are separated by a distance of $\bar{Y}$ in the phase encoding direction. The intensity and blurring of these ghosts is determined by the convolution with $F^{-1}[K_p(\omega_Y)]$.

The image of a volume element flowing in the read direction is described by

$$\hat{m}(x,y) = \exp[i\phi_{XV}] \sum_{p=-\infty}^{\infty} F^{-1}[K'(\omega_X)] * F^{-1}[K_p(\omega_X)] * m[x - \hat{x}, \pm(y + p\bar{Y})]. \tag{5.3}$$

ϕ_{XV}, $K'(\omega_X)$, and $\hat{x}$ all depend on the time-averaged flow velocity V_X (equations 3.57 and 3.59), and $K_p(\omega_X)$ depends on A_X. Also, $\hat{x}$ is proportional to the echo number E. A stationary volume element will image free of artifact, and the image of an elemental volume that flows steadily is both shifted by $\hat{x}$ and blurred in the x direction due to the convolution with $F^{-1}[K'(\omega_X)]$. An elemental volume that experiences pulsatile flow will produce ghosts separated in the phase-encoding direction by $\bar{Y}$ and further blurred in the x direction by the convolution with $F^{-1}[K_p(\omega_X)]$. The intensity of these ghosts depends, in part at least, on the convolution with $F^{-1}[K_p(\omega_X)]$.

The flow-phantom imaging experiments conducted utilized the normal 2DFT spin-echo pulse sequence (Fig. 3.1). It was desired to establish that unsynchronized imaging led to ghosting, and that the intensity and position of these ghosts were compatible with theoretical expectations. Furthermore, the ability to remove ghosts by synchronized imaging was to be tested. The value of the $\hat{x}$ and $\hat{y}$ shift for elemental volumes having a non-zero V_X or V_Y, and the relationship of these shifts with echo number E, was also to be measured.

To meet the above objectives, several imaging experiments were conducted under different conditions. Initially, the flow phantom (detailed in the following section) was oriented to produce flow normal to the slice plane, and four sets of eight-echo imaging experiments were performed. The first experiment was conducted with the flow phantom tubing plugged downstream of the phantom, thereby restricting flow. Throughout the second experiment, steady flow was maintained through the phantom, and in the third and fourth experiments, the data collection was unsynchronized and synchronized, respectively, to pulsatile flow. An ECG delay of 200 ms was used for the synchronized imaging experiment. These experiments were repeated for two other flow-phantom orientations such that the flow was restricted to the y-z plane at 45° to the z axis and to the x-z plane at 45° to the z axis. In all of these imaging experiments the relaxation delay was fixed at 1.0 s and two averages of each projection were collected. In order to place the first-order ghosts ($p = \pm 1$) at the periphery of the image, the period of the pulsatile flow was chosen to be 1.6 s. To insure that the flowing water produced signal in the final 2DFT modulus images, it was necessary to restrict the average flow velocity of this water to below 10 cm/s.

5.3.1 Experimental Design and Procedure

The flow phantom used in the phantom study consists of two concentric cylinders, sealed at one end and open at the other (Fig. 5.1). The space between the two cylinders was filled with a gel made from a 10:1 (by volume) mixture of tap water and TX-150 powder (Oil Center Research Inc., Lafayette, Louisiana). A nylon cap was used to seal the open end of the phantom. A 1/4 inch inner diameter (ID) Tygon tube, bent in a U shape, was placed inside the smaller cylinder and the ends of the tubing passed through nylon fittings that were screwed into threaded holes in the nylon cap. The space around the Tygon tubing was filled with pure silica sand to prevent movement of the Tygon tubing.

The sand also provided a dark background around the Tygon tubing in the NMR images, thereby facilitating the visualization of artifacts due to pulsatile flow. The TX-150 gel was necessary because it provided signal to permit an optimization of the spectrometer settings.

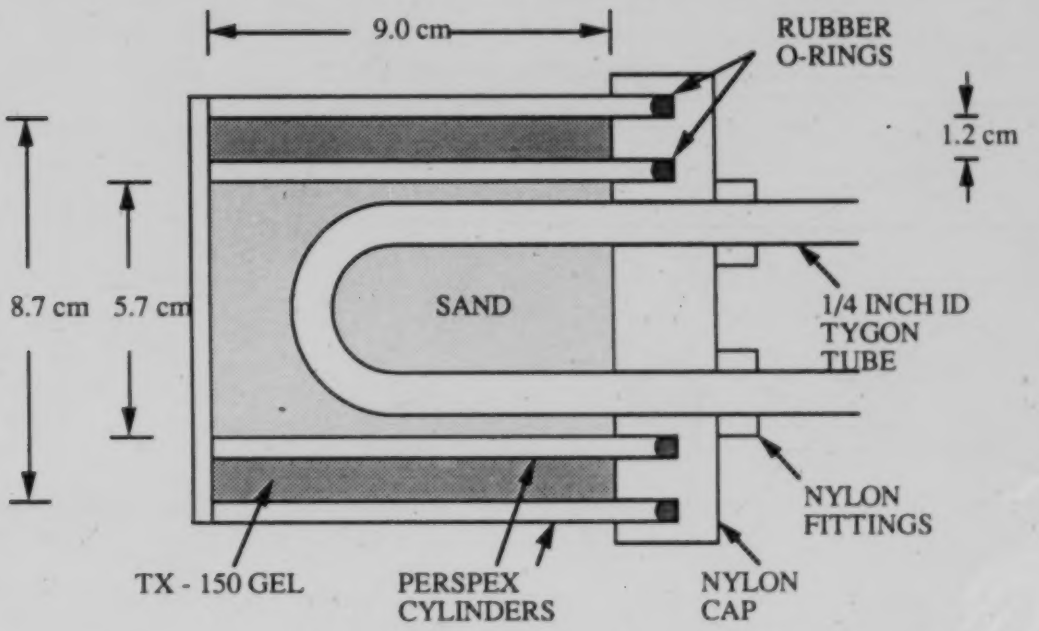

Figure 5.1 Cut-away side view of the flow phantom used in imaging experiments.

A 20-liter reservoir was raised 1 m above the phantom (Fig. 5.2) and filled with tap water. The water level in the reservoir was maintained to within ±1 cm of a reference level throughout all imaging experiments. One-half inch ID Tygon tubing connected the reservoir output to the inflow tube of the phantom, and the phantom outflow tube was connected to port 3 of an Ascolectric 8320A206 3/8 inch solenoid-controlled universal valve with similar tubing. The universal valve was set up as a normally open valve which could be closed by energizing the valve's solenoid. Water flowing from ports 1 and 2 of the universal valve emptied into a collection bucket. A Hofstader clamp attached to the Tygon tubing upstream of the phantom was used to regulate the flow rate during the imaging experiments. Pulsatile flow was generated by periodically interrupting the steady

flow through the phantom. A 100-ms pulse, repeated periodically, was used to drive a power transistor that energized the universal valve's solenoid coil, thereby closing the universal valve intermittently. The same pulse train was used to drive a TTL one-shot chip whose output was sent to the spectrometer to trigger the imaging pulse sequence. The duration between the arrival of the trigger pulse and the initiation of the pulse sequence (ECG delay) was specified in the software.

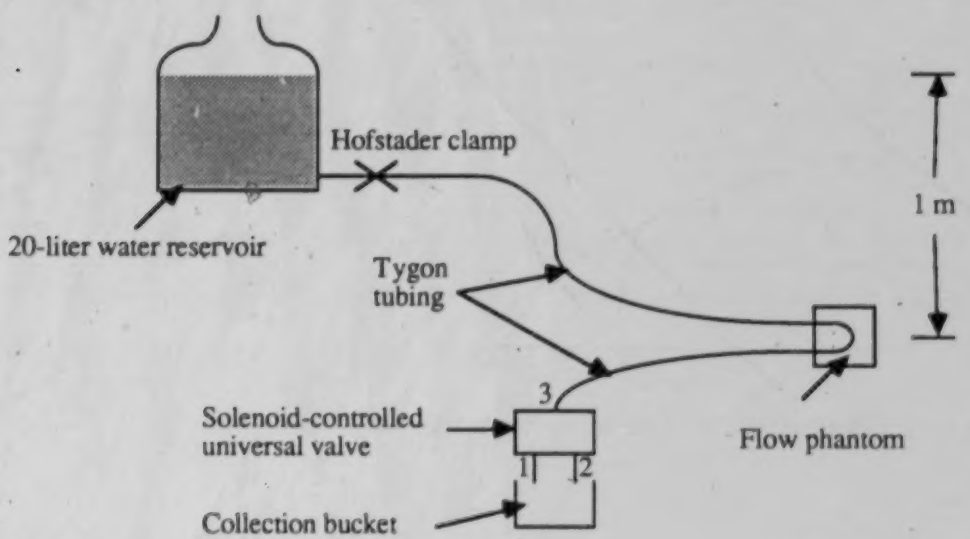

Figure 5.2 Illustration of the experimental setup for flow studies. The solenoid-controlled valve was placed approximately 2 m away from the magnet.

5.3.2 Phantom-Study Results and Discussion

Figure 5.3 displays a selection of unsynchronized and synchronized pulsatile-flow images from the above experiments. Unsynchronized first-echo images for flow in the z, y-z, and x-z directions are shown in Figs. 5.3A, 5.3E, and 5.3I, respectively. Corresponding synchronized images, obtained under similar conditions, are shown in Figs. 5.3B, 5.3F, and 5.3J. Unsynchronized and synchronized fourth-echo images are shown in Figs. 5.3C and 5.3D for z flow, Figs. 5.3G and 5.3H for y-z flow, and Figs. 5.3K and 5.3L for x-z flow. The average flow velocity during each of the above

A

B

Figure 5.3 First-echo images from the flow-phantom experiments with pulsatile flow in the z direction. A) unsynchronized image and B) synchronized image.

C

D

Figure 5.3 Fourth-echo images from the flow-phantom experiments with pulsatile flow in the z direction. C) unsynchronized image and D) synchronized image.

E

F

Figure 5.3 First-echo images from the flow-phantom experiments with pulsatile flow in the y-z direction. E) unsynchronized image and F) synchronized image.

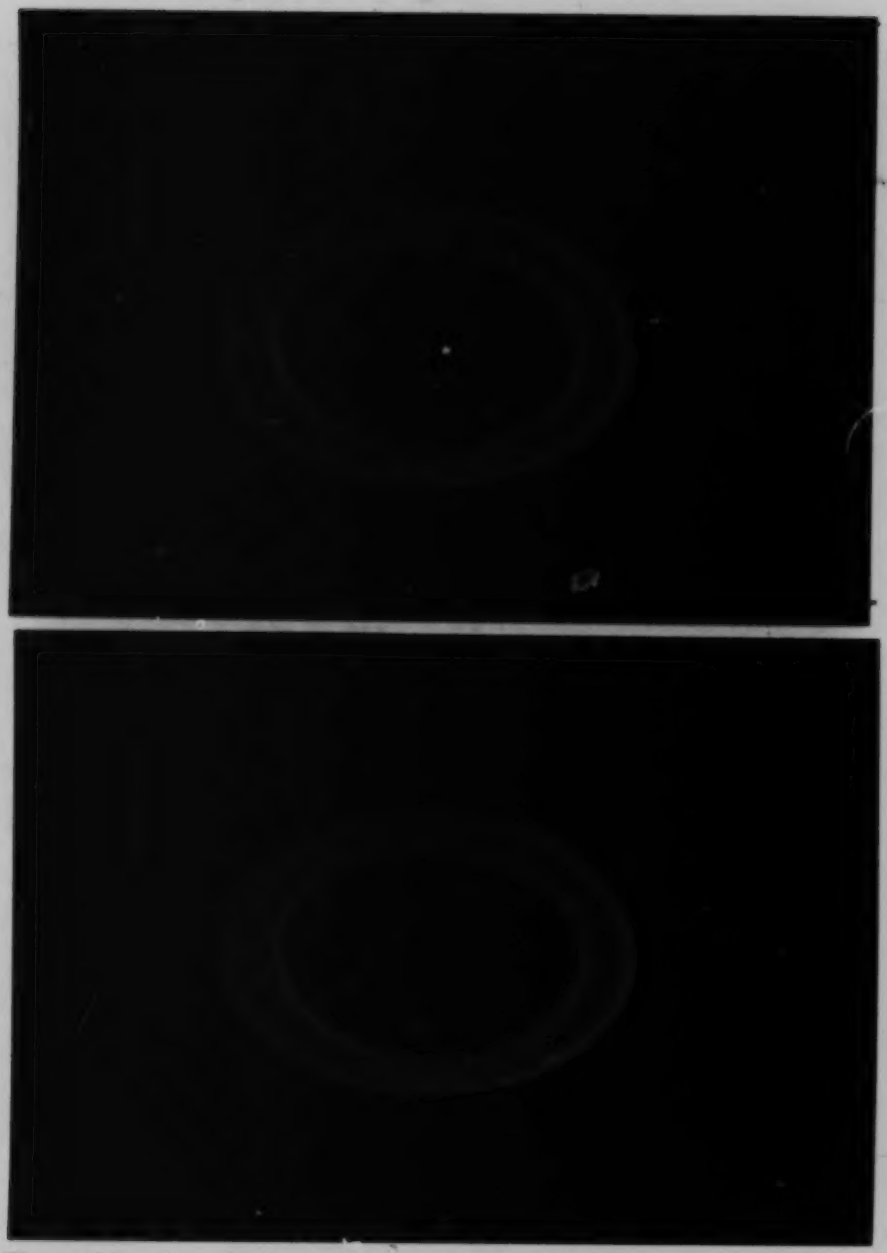

G

H

Figure 5.3 Fourth-echo images from the flow-phantom experiments with pulsatile flow in the y-z direction. G) unsynchronized image and H) synchronized image.

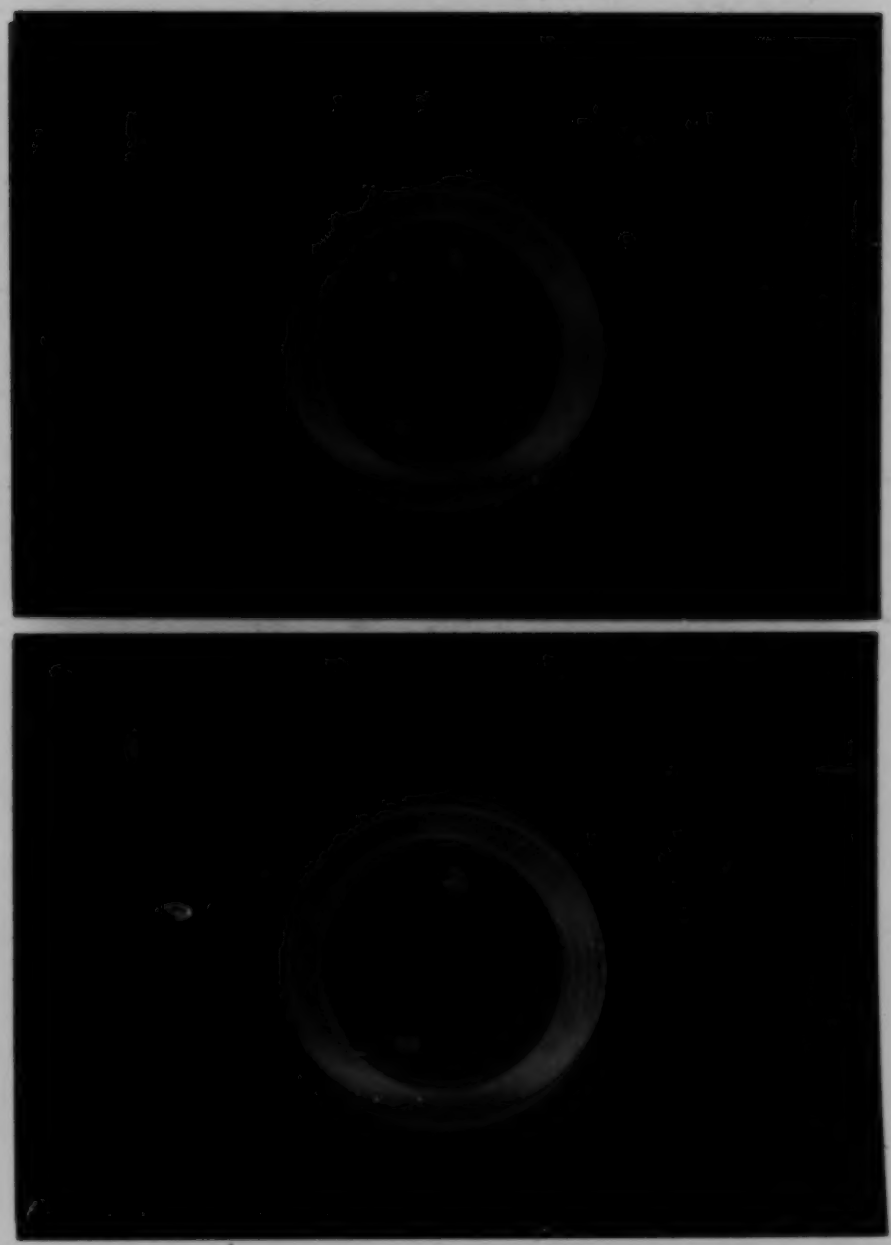

I

J

Figure 5.3 First-echo images from the flow-phantom experiments with pulsatile flow in the x-z direction. I) unsynchronized image and J) synchronized image.

K

L

Figure 5.3 Fourth-echo images from the flow-phantom experiments with pulsatile flow in the x-z direction. K) unsynchronized image and L) synchronized image. All the above images are displayed such that the phase-encoding (y) direction is horizontal and the read-encoding (x) direction is vertical.

experiments was calculated, and found to lie between 5 and 10 cm s^{-1}, which is approximately an order of magnitude smaller than the time-averaged velocities encountered in the major arteries of a cat. It should be observed that ghosts are present in all unsynchronized images, and that the most intense ghosts appear in the first-echo images. Also, note that synchronization of the data acquisition to the pulsatile flow eliminates ghosts in all images (even later echoes) to below the average noise level. In some cases, this translates to a reduction in ghost intensity by an order of magnitude.

The location of the ghost structures in the unsynchronized images is addressed next. It was shown in chapter 3 that pulsatile flow in any direction resulted in ghosts repeating at intervals of $\bar{Y}$ in 2DFT NMR images. Equation 3.13, which defines $\bar{Y}$, may be rearranged to read

$$\bar{Y} = \frac{t_y}{T} L_Y \tag{5.4}$$

where T is the pulsatile flow period, L_Y is the image's field-of-view in the phase-encoding direction, and t_y is the time between the start of two adjacent projections. Note that the pulse-sequence duration, the relaxation delay and the number of averages for each projection will influence the value of t_y. In an image that was acquired for flow perpendicular to the slice plane, the outer diameter of the ring of TX-150 gel was measured in terms of pixel widths. Knowing the size of the ring (8.7 cm), L_Y was calculated by solving

$$\frac{L_Y \text{ (cm)}}{256 \text{ (pixel widths)}} = \frac{\text{dia. of TX-150 ring (cm)}}{\text{dia. of TX-150 ring (pixel widths)}} \tag{5.5}$$

L_Y evaluated to 17.8 cm, with an estimated error of ±3%. Using equation 5.4 $\bar{Y}$ equals 392 pixels, with an estimated error of ±4%.

In the unsynchronized first-echo images for pulsatile flow in the z, y-z and x-z directions, the locations of the centers of the inflow and outflow tubes were determined. The center positions of the three lowest-order ($p = \pm 1, \pm 2$, and ± 3) ghost structures were calculated, keeping in mind aliasing due to a finite L_Y. The center positions of the two most intense ghosts were measured and found to agree very well with the calculated positions of the first-order ghosts (Table 5.1). The measured center positions of the remaining ghost structures, usually two but sometimes only one, coincided with the calculated position of the third-order ghosts (Table 5.1). Taking into account the estimated errors, it can be concluded that the measured ghost positions compared favorably with the calculated ghost positions especially for flow along the z axis. The center positions of the ghosts in the higher-echo images were also measured and found to agree with measurements of the first-echo images to within ±2 pixels.

Ghost	z flow				y-z flow				x-z flow			
	Inflow		Outflow		Inflow		Outflow		Inflow		Outflow	
	Calc.	Meas.	Calc.	Meas.	Calc.	Meas.	Calc.	Meas.	Calc.	Meas.	Calc.	Meas.
p = 1	126	123	-113	-115	125	118	-115	-121	123	116	-112	-121
p = 2	-9	†	7	†	-10	†	5	†	-12	†	8	†
p = 3	110	104	126	120	109	†	124	100	107	82	127	100
p = -1	-112	-113	-96	-96*	-113	-100	-98	-89*	-115	-103	-95	-83*
p = -2	23	†	39	†	22	†	37	†	20	†	40	†
p = -3	-96	-93	-80	-96*	-97	-66	-82	-89*	-99	-65	-79	-83*

† These ghost structures could not be readily identified in the images.
* This single ghost structure of the outflow tube, for each of the z, y-z, and x-z flow experiments, is likely due to the overlap of the p=-1 and the p=-3 ghosts.

Table 5.1 Calculated center locations (in pixels) of the three lowest-order ghosts and the measured locations of the readily identifiable ghosts in the first-echo images for flow in the z, y-z, and x-z directions. The error in the calculated ghost positions were estimated to be ± 16 pixels for the $p = \pm 1$ ghosts, ± 32 pixels for the $p = \pm 2$ ghosts, and ± 48 pixels for the $p = \pm 3$ ghosts. The error in determining the positions of ghost structures in the image is estimated to be ± 2 pixels.

In practice, it is difficult to calculate the average intensity of a ghost structure. To understand why, consider an elemental volume of spins that is flowing in a pulsatile fashion along one of the three Cartesian axes. The analysis of Chapter 3 shows that the intensities of ghosts due to this elemental volume are determined by the functions K_p for flow normal to the slice (z) plane, $K_p(\omega_Y)$ for flow along the phase encoding direction (y) and in part by $K_p(\omega_X)$ for flow along the read direction (x). The values of these functions, in turn, depend upon the amplitudes of the flow velocity's sinusoidal component (A_X, A_Y, or A_Z). If, in the experimental situation, it were possible to cause plug flow to occur, then all elemental volumes of spins within a vessel would have the same flow velocity at any instant of the pulsatile flow period. Therefore, all of these volume elements would share a common A_X, A_Y or A_Z value, and ghost structures due to these mobile volume elements would have uniform intensity. However, in the flow experiments conducted, laminar flow in the Tygon tube resulted in a parabolic velocity profile across the tube's diameter, resulting in a distribution of velocities amongst the volume elements inside this tube. Consequently, each mobile volume element has a unique A_X, A_Y or A_Z associated with it, and the ghost structures due to these elemental volumes will not exhibit uniform image intensity. For this reason, and because A_X, A_Y and A_Z are difficult to measure in practice, calculation of the average intensity of a particular ghost structure was deemed infeasible.

The ability to detect ghost structures is influenced by many factors. For instance, aliasing due to a finite field-of-view can cause two ghost structures to overlap so that only one structure appears. This is probably why, although the inflow tube usually has four ghost structures associated with it, while the outflow tube often has only three ghosts associated with it. No second-order ghost structures were readily identifiable. It is important to note that if the intensity of a particular ghost structure is comparable to the image noise signal, then it is possible for this ghost to be completely obscured. To

appreciate this, recall that initially the elements of an image matrix are complex numbers. In this complex matrix, consider an element whose final signal is a superposition of a ghost signal and a noise signal. If the vectors representing the ghost and noise signals are of comparable magnitude, then their resultant magnitude will not necessarily be larger than either one since vector addition is not, in general, linear. Therefore, the modulus of the resultant may not reflect the presence of the ghost signal. If ghost structures are to be easily discerned, their signal has to be much greater than the noise, and this may not have been the case for the second-order ghosts in these images. Furthermore, the nature of the pulsatile flow in the experimental situation may contribute to brighter third-order ghosts compared to the second-order ghosts. To understand how this may occur, note that the pulsatile flow in the flow-phantom was generated by abruptly stopping the steady flow in the Tygon tubes. The resulting flow is described more accurately by a square wave rather than a sinusoid. This flow will therefore have a fundamental frequency (first harmonic) and odd higher-order harmonics. The third-order ghost of the first harmonic will fall at the same location as the first-order ghost of the third harmonic, possibly reinforcing the ghost structure at this position.

The results of the analysis in Chapter 3 also suggest that the image of an elemental volume of spins having a non-zero average velocity component in the read or phase encoding directions will be shifted by $\hat{x}$ or $\hat{y}$, respectively. It is important to recall that the shift $\hat{x}$ is expected to increase for the later echo images, but that $\hat{y}$ is expected to remain fixed for all echo images. The average flow rate during an imaging experiment was calculated by evaluating the ratio of the volume of water collected during the experiment to the experiment duration. The ratio of the average flow rate to the cross-sectional area of the Tygon tubing gave the average flow velocity. For the steady-flow experiments, the average flow velocities were determined to be 4.9 cm s^{-1} and 5.0 cm s^{-1} for flow in the x-z and y-z directions, respectively. The error in the calculation of the average flow velocity

for an imaging experiment was estimated to be ±15%. This large error is principally due to the presence of air bubbles which made the calculation of the tubing cross-sectional area less certain. For a volume element whose flow velocity has a magnitude equal to the average flow velocity in these experiments , $\hat{x}$ and $\hat{y}$ can then be estimated by evaluating equations 3.51 and 3.57 to give

$$[\hat{x}]_{AVG} \approx 1.4 \text{ pixels} \quad ; (1\text{st echo})$$
$$\approx 11.6 \text{ pixels} \quad ; (8\text{th echo})$$
$$[\hat{y}]_{AVG} \approx 0.9 \text{ pixel},$$

where the angle between the z axis and the axis of the Tygon tubes has been accounted for.

Since, in the experimental situation, flow occurs in a tube whose cross-sectional area (in the image) is equivalent to about 75 pixels, it is not feasible to measure the $\hat{x}$ and $\hat{y}$ shifts of a single mobile volume element directly. To determine if the effects of the $\hat{x}$ shift were measurable in the phantom study images, the x-z 'no-flow' and 'steady-flow' images were analyzed. A column (in the read direction) passing through the center of the inflow tube was selected in these image matrices. At each position along the column, the average intensity of ten pixels, including five on one and four on the other side of the chosen column, was calculated, thereby yielding an average intensity profile in the read direction. The region of the profile coinciding with the vessel exhibited a peak, and the coordinate of this peak's maximum was plotted (Fig. 5.4) for all echoes of the 'no-flow' and 'steady-flow' imaging experiments. It is assumed that there is a correlation between the $\hat{x}$ shift of mobile volume elements and the location of this peak's maximum. A definite trend, showing the movement of the peak's maximum with echo number is evident for the 'steady-flow' images, suggesting that the $\hat{x}$ shift of mobile volume elements increases with echo number. From the straight-line fit of Fig. 5.4, the peak maximum is estimated to shift by about 11.5 pixels for the eighth echo which compares favorably with the $[\hat{x}]_{AVG}$ value of 11.6 pixels calculated previously. At physiological blood flow velocities of 0 to 150

cm s^{-1} (Knudsen, 1987), the increase in the $\hat{x}$ shift, especially for higher-echo images, may compromise the ability to obtain quantitative information from regions of images that are in the vicinity of large blood vessels. The direction of flow during the imaging experiment was such that the $\hat{x}$ shift would cause moving volume elements to be shifted in the positive x direction as is verified by the plot of Fig. 5.4.

For flow in the y-z direction, similar average-intensity profiles were calculated in the phase-encoding direction. An examination of the peak-maximum locations, in these profiles, for all echoes of the 'no-flow' and 'steady-flow' images showed no measurable $\hat{y}$ shift. The same peak-maximum location for all echoes of the 'steady-flow' experiment suggests that $\hat{y}$ is independent of echo number.

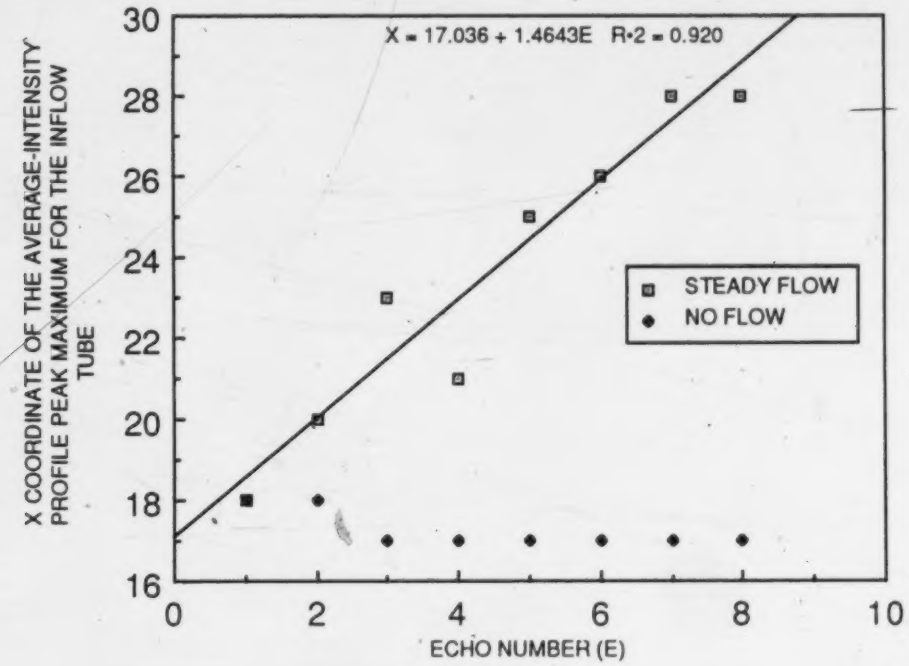

Figure 5.4 The x coordinate of the average-intensity profile's peak maximum plotted against echo number (E) for the x-z 'no-flow' and 'steady-flow' imaging experiments. Note that the location of the peak's maximum is increasing with echo number since $\hat{x}$ increases with echo number.

5.4 Animal Study

The 2DFT pulse sequence used for the animal imaging experiments is shown in Fig. 3.1. Compared to unsynchronized imaging, the improvement in image quality due to cardiac synchronization was to be evaluated by these experiments. Further reduction in artifactual noise due to both cardiac synchronization and respiratory gating was also to be examined.

To satisfy the above objectives, several animal imaging experiments were performed. The experimental setup is described in section 5.4.1. Since the severest motion artifacts are expected to occur in the heart, a transverse slice intersecting the heart was selected for these experiments. Each projection was averaged twice, with the relaxation delay set to 1.0 s. Eight sets of eight-echo images were acquired: the first set was neither synchronized to the ECG nor gated to the respiratory signal, the next set was both ECG synchronized and respiratory gated, and the last six sets were only cardiac synchronized, each with a different ECG delay.

5.4.1 Experimental Procedure

Adult cats were anesthetized with an intramuscular injection of a mixture of xylazine hydrochloride (Rompun^{TM} , Haver-Lockhart, Rexdale, Ont., 0.5 mg kg^{-1}), ketamine hydrochloride (Ketalean^{TM}, MTC Pharmaceuticals, Cambridge, Ont., 5 mg kg^{-1}), and one drop of acepromozine maleate (Altravet^{TM}, Ayerst Laboratories, Montreal, Que.). Half the above dosage was delivered approximately every hour for the duration of the experiment session. On the right fore and both hind limbs of a cat, a small region of skin was exposed by shaving off the fur. Ag/AgCl ECG electrodes, to which the lossy transmission line leads were attached, were applied at these locations. The animal was then placed in a plexiglass tray and restrained by Velcro straps. Significant movement of the ECG leads

was prevented by taping them to the tray. A rubber bellows was wrapped snugly around the cat's abdomen with the aid of another Velcro strap. The animal was then placed in the magnet bore and the ECG leads were connected to the battery-powered ECG transmitter unit placed inside the RF screened magnet enclosure. The right leg ECG leads were used as the active electrodes while the left-leg lead was used as the reference (see Fig. 4.4A). A short length of 1/16 inch ID Tygon tubing connected the rubber bellows to the pressure transducer of the battery-powered respiratory transmitter unit that was placed next to the ECG transmitter unit. These two transmitter units were coupled to their respective receiver units by fiber-optic cables. The value of the adjustable dc voltage in the ECG trigger circuitry was set to produce reliable trigger pulses (see Fig. 4.4B). These pulses and the respiratory gating signal were routed to the multiplexer unit. Two TTL lines from the spectrometer were used to pulse the multiplexer control lines, while the multiplexer output line was directed to the spectrometer input line (see Fig. 4.5). Finally, the spectrometer settings were optimized and the imaging experiments started.

5.4.2 Animal-Study Results and Discussion

Consider Fig. 5.5A, an unsynchronized and ungated transverse image of a cat taken at the level of the heart. There are two principal types of artifacts that degrade this image. The first type of artifact is the ghosting and streaking due to pulsatile flow, and the second type is the broad low-intensity band of artifactual signal, spread in the phase-encoding direction, that overlays the anatomical structures of the cat. Furthermore, this low-intensity artifact spans the entire image field-of-view in the phase encoding direction. It is assumed that motion in the thoracic region of the cat contributes, in part at least, to this broad low-intensity band of signal.

To evaluate the improvement in image quality due to synchronization, one unsynchronized and several synchronized imaging experiments were conducted. The first-echo images

from these experiments are displayed in Fig. 5.5. Figs. 5.5B to 5.5G are synchronized images, each obtained at a different point of the cardiac cycle. The sketch of Fig. 5.5H identifies the major organs in the above thoracic cat images. The points of the cardiac cycle at which the raw data for these first-echo synchronized images were acquired are shown in Fig. 5.5I. Variation in the signal intensity of the thoracic aorta and vena cava in Figs. 5.5B to 5.5G reflects the different instantaneous blood-flow velocities in these vessels at various points of the cardiac cycle. This observation confirms that these images are synchronized to the cardiac cycle.

Consider next the effects of pulsatile flow in unsynchronized imaging. Recall that periodic pulsatile flow leads to ghosting of the moving spins while aperiodic pulsatile flow causes signal from the mobile spins to be streaked in the phase-encoding direction. In Fig. 5.5A, the artifacts due to pulsatile flow are most clearly manifested when blood flow in the thoracic aorta and vena cava are considered. At the edge of the lung tissue (horizontally displaced from the thoracic aorta) there appears a structure whose shape and size resemble the thoracic aorta and vena cava. Note the absence of this structure in all the synchronized images (Fig. 5.5B to 5.5G). It is therefore reasonable to conclude that this structure is a ghost of the thoracic aorta and vena cava. Also, notice the presence of a narrow band of low-intensity signal, intersecting the thoracic aorta and vena cava, and spanning the entire image in the phase-encoding direction. This signal, streaked throughout the phase-encoding direction, is thought to arise due to the small aperiodicity in the pulsatile flow waveform. With the exception of Fig. 5.5D, which will be discussed next, all the synchronized images lack this widespread artifact.

In Fig. 5.5D, there appear signal structures that are located outside the image of the cat and horizontally displaced from the thoracic aorta and vena cava. The shape and location of these structures suggest that they are ghosts of these large blood vessels. A

A

B

Figure 5.5 First-echo images of the cat at the anatomical level of the heart. A) unsynchronized, B) synchronized with an ECG delay of 1 μs. The average artifactual signal and background noise levels are calculated by evaluating the average intensity of the rectangular and square regions shown in Fig. 5.5A.

C

D

Figure 5.5 First-echo images of the cat at the anatomical level of the heart. C) and D) synchronized images with ECG delays of 20 ms and 60 ms, respectively.

E

F

Figure 5.5 First-echo images of the cat at the anatomical level of the heart. E) and F) synchronized images with ECG delays of 120 ms and 180 ms, respectively.

G

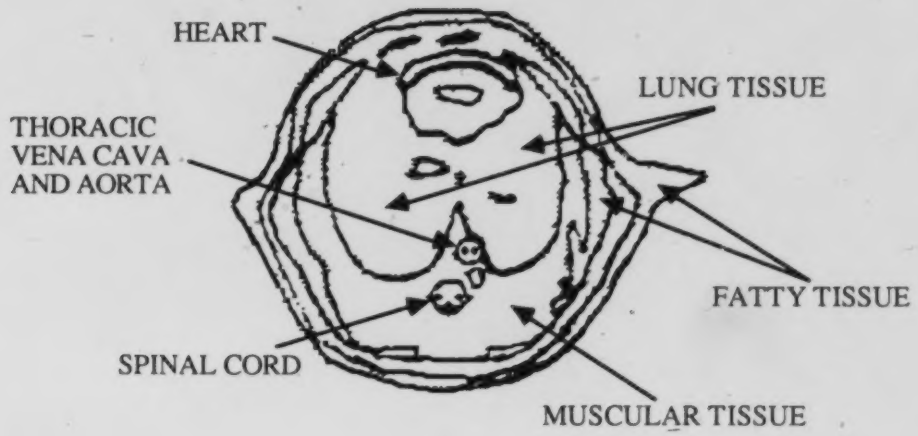

H

Figure 5.5 G) First-echo image of the cat at the anatomical level of the heart obtained with an ECG delay of 250 ms. H) Sketch indicating location of important physical structures in above thoracic cat images.

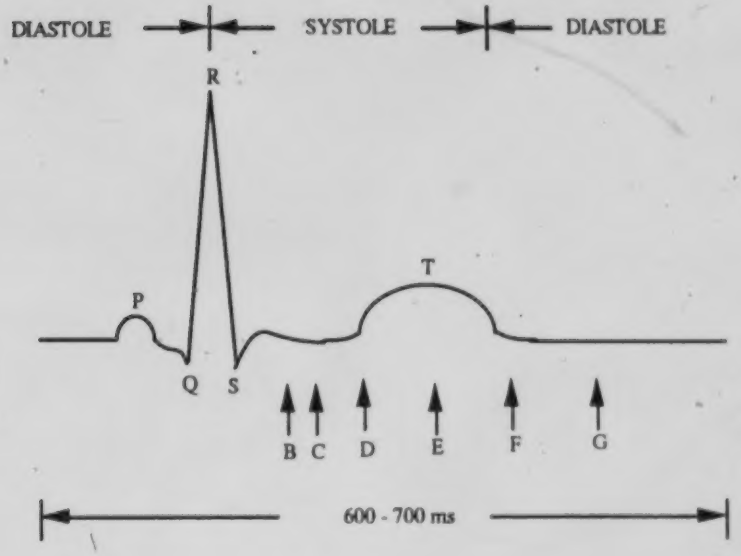

I

Figure 5.5 I) Arrows depict the point in time when data for images of Fig. 5.5B to 5.5G were acquired.

plausible explanation of this phenomenon is that the pulsatile flow in the large thoracic vessels is not perfectly periodic. The raw data of the image shown in Fig. 5.5D were acquired at a point in the cardiac cycle when the flow in the thoracic aorta was close to maximal. If this peak flow velocity was identical from heartbeat of heartbeat, then synchronization would be expected to eliminate ghosting due to pulsatile flow. However, this peak flow velocity is likely to vary with each heartbeat, so that, despite synchronization, the velocity of an elemental volume of spins inside this vessel will vary from projection to projection, leading to ghosting and blurring artifacts. The presence of discrete ghosts suggests that the variation in the peak velocity has a periodic component. If the data are acquired at a point in the cardiac cycle when the blood-flow velocity in the thoracic aorta is minimum, the variation in the instantaneous blood-flow velocity at this point of the cardiac cycle from one heartbeat to the next is also minimized, thereby minimizing ghosting artifacts.

To minimize the effects of pulsatile flow in 2DFT NMR imaging, acquisition of NMR raw data should be synchronized to the cardiac cycle. Furthermore, this data should be acquired when the velocity of the blood in the major vessels within the chosen slice is minimal.

Next, the effect of synchronization in reducing the low-intensity band of signal will be evaluated. To differentiate this low-intensity band of signal from ghosting, it will be referred to as the 'artifactual' signal. In order to compare different cat images, a method of estimating the artifactual signal level of these images was required. The average intensity of a 40 x 140-pixel region adjacent, in the phase-encoding direction, to the cat (see Fig. 5.5A) was used to estimate the artifactual signal level in these images. Obviously, the estimate of the artifactual signal level of an image will be larger than the background noise level of the same image. The average intensity of a 20 x 20-pixel region in the lower right hand corner of the image (see Fig. 5.5A) was used to estimate an image's background noise level. In the images of Fig. 5.5, the typical tissue signal was more than two orders of magnitude more intense than the background noise level.

In each of the images of Fig. 5.5, the artifactual signal and background noise levels were calculated; they are plotted in Fig. 5.6. Clearly, the artifactual signal level is a function of the ECG delay used in the synchronized acquisitions. Compared to the unsynchronized image, images acquired in the early or middle stages of systole exhibit higher levels of artifactual signal, while images acquired during the early or middle stages of diastole show lower levels of artifactual signal. This result is not unexpected because motion associated with ventricular contraction and ejection of blood into the aorta and pulmonary artery, which is expected to contribute to the artifactual signal in images, occurs during systole.

To determine the effect of synchronization on later-echo images, all images from the unsynchronized and the least-noisy synchronized (ECG delay = 250 ms) imaging experiments were analyzed. Second-echo images from these experiments are shown in Fig. 5.7. Using the method previously described, the background noise and artifactual

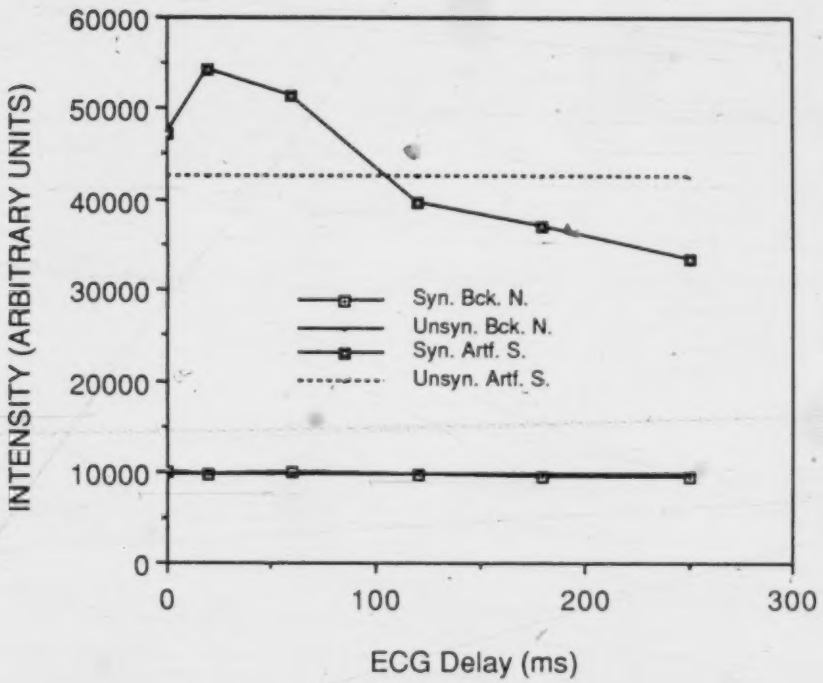

Figure 5.6 Artifactual signal of the first-echo synchronized images plotted as a function of the ECG delay used. Arrows indicate the ECG delays used in the synchronized images presented in Fig. 5.5. For comparison, the artifactual signal in the first-echo unsynchronized image is also shown. Note that the lines indicating the background noise in the unsynchronized and synchronized images overlap.

signal levels of all the images from these experiments were estimated, and are shown in Fig. 5.8. The background noise level of any echo in the synchronized set was 2 - 14% lower than the background noise level of the corresponding echo in the unsynchronized image set. These differences may be due to drifting of the RF coil's tuning frequency in

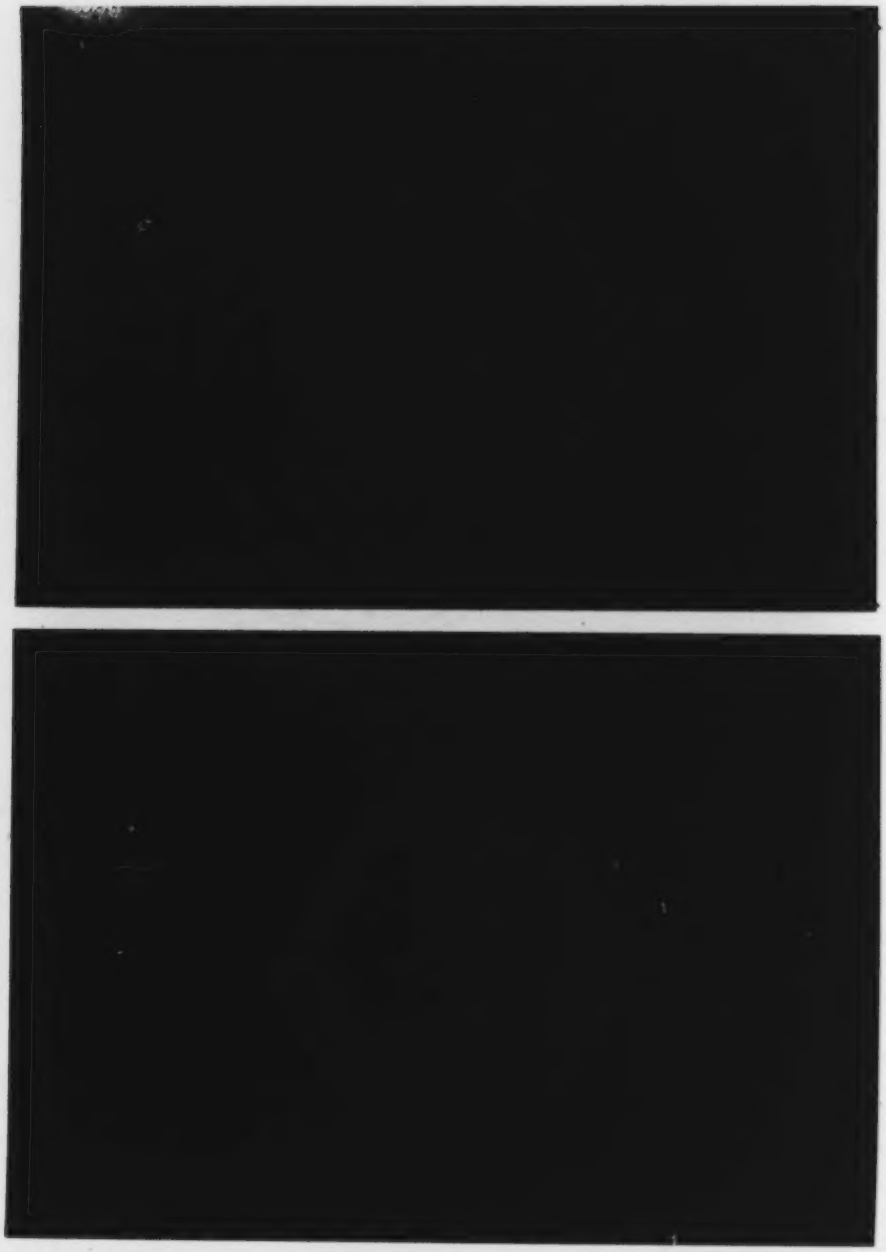

A

B

Figure 5.7 Transverse images of a cat at the anatomical level of the heart. A) shows the second-echo unsynchronized image and B) shows the second-echo synchronized image obtained with an ECG delay of 250 ms.

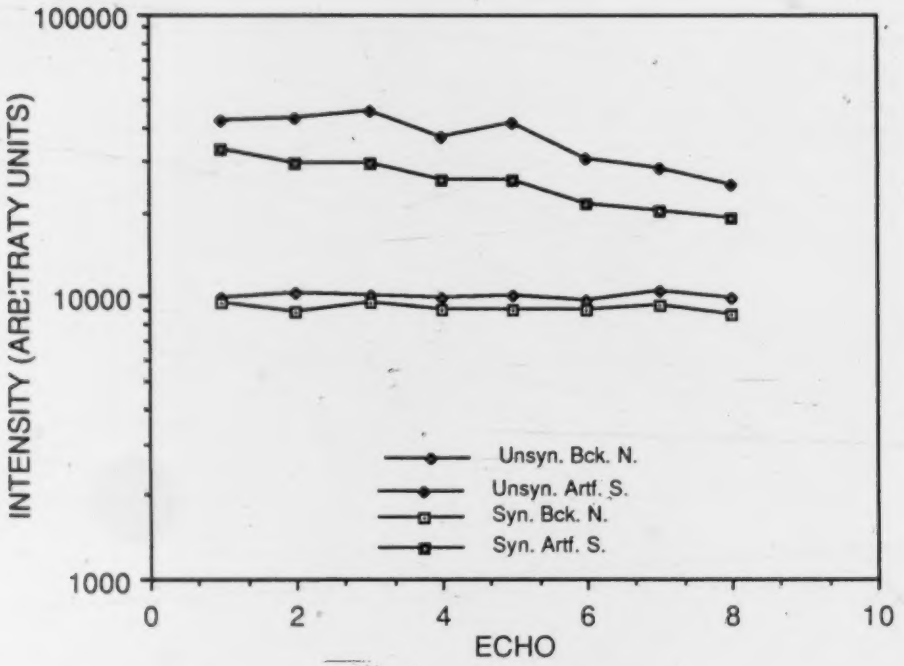

Figure 5.8 Artifactual and background noise levels as a function of echo for the unsynchronized and synchronized (ECG delay = 250 ms) imaging experiments.

the time between experiments. However, for any echo image, the synchronized image has a 25% to 35% lower artifactual signal level compared to the artifactual signal level of corresponding unsynchronized image. Therefore, compared to unsynchronized imaging, synchronization reduces the level of artifactual signal in all echo images, provided data for these images are collected in the diastolic phase of the cardiac cycle. There is, however, a significant amount of artifactual signal still remaining in the synchronized images (Figs. 5.5, 5.7, 5.8).

An important observation concerns the slowly decaying behavior of the artifactual signal (Fig. 5.8). A single exponential fit to this data results in time constants of approximately 325 ms. Thus, a particular region of interest in an image may yield, in

addition to one or more genuine T_2 components, an extra T_2 component due to the slowly decaying artifactual signal. The possible inclusion of this extra component should be born in mind so as to avoid misinterpretation of quantitative T_2 calculations.

It was previously mentioned that, despite synchronization, a significant amount of artifactual signal remains in 2DFT multi-echo images. It was felt that respiratory motion contributed, at least in part, to this remaining signal. The ability to acquire ECG-synchronized and respiratory-gated data was developed and the additional improvement due to gating was evaluated. Two image sets, one synchronized , the other synchronized and gated, were acquired. The ECG delay for both imaging experiments was set to 1 μs and the data acquisition was gated to the expiration part of the respiratory cycle for the synchronized and gated image set. The first- and second-echo images from these experiments are shown in Fig. 5.9

The artifactual signal and background noise levels were estimated in all images of the synchronized, and synchronized and gated sets. Fig.5.10 shows the results of these calculations. The background-noise level in any echo of the synchronized and gated set is 1 - 6% lower than the background noise in the corresponding echo of the synchronized set. However, the artifactual signal in any echo of the synchronized and gated set is 15 - 24% lower than the artifactual signal in the corresponding echo of the synchronized set. Compared to synchronization alone, synchronization and respiratory gating reduces the artifactual signal in all echo images. However, even with synchronization and gating, significant artifactual signal still remains in these images (Figs. 5.9C and 5.9D, Fig.5.10). The artifactual signal is expected to be minimized when raw-data acquisition is synchronized to the diastolic stage of the cardiac cycle and gated to the expiration part of the respiratory cycle.

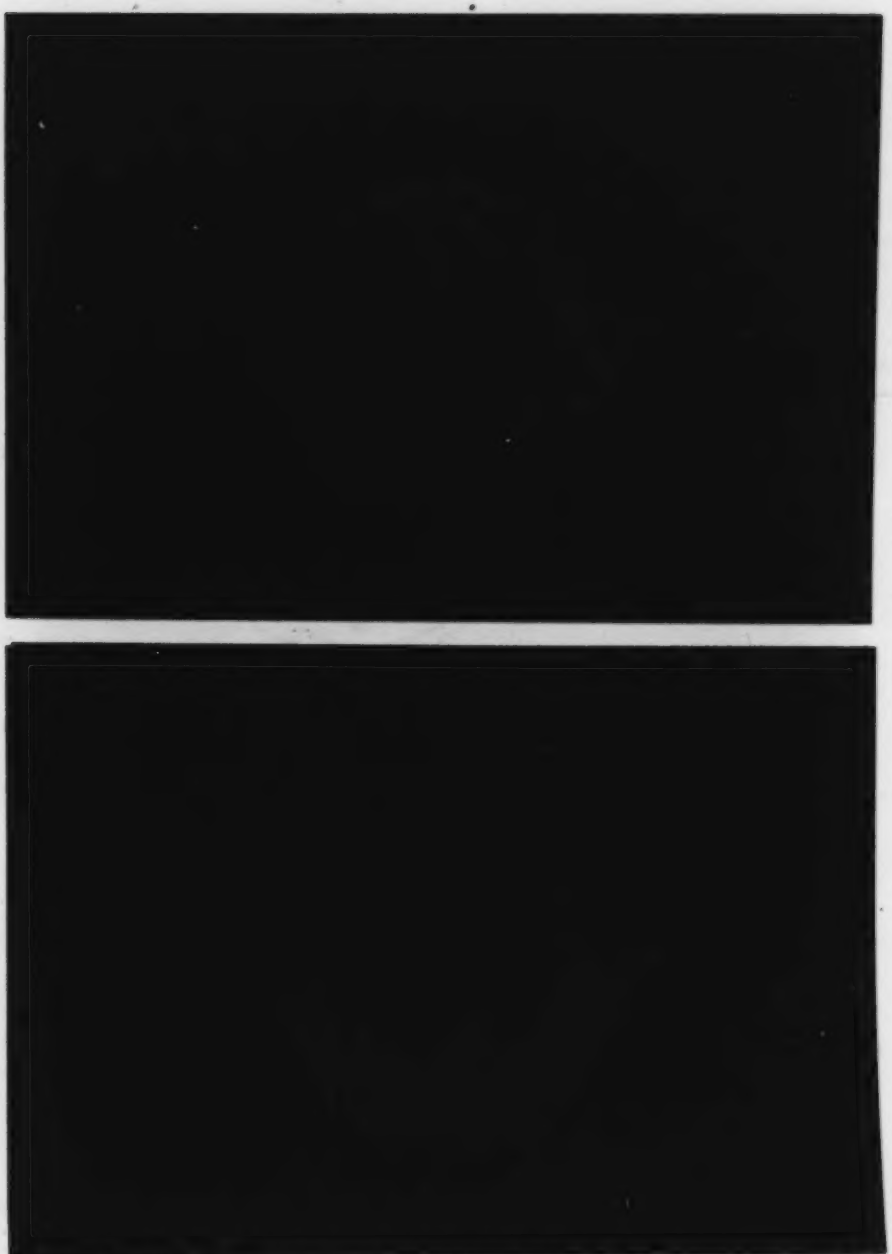

A

B

Figure 5.9 First-echo synchronized (A) and synchronized and gated (B) images of a cat at the anatomical level of the heart. The ECG-delay was set to 1 μs.

C

D

Figure 5.9 First-echo synchronized (A) and synchronized and gated (B) images of a cat at the anatomical level of the heart. The ECG-delay was set to 1 μs.

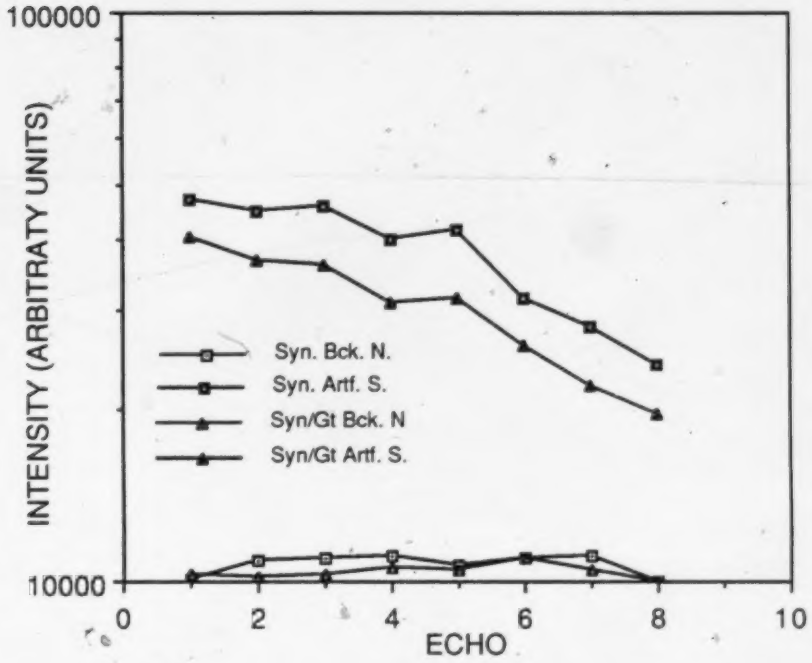

Figure 5.10 Background noise and artifactual signal intensities in the synchronized, and synchronized and gated image sets. In both images the ECG delay used was 1 μs.

To summarize, there is a significant reduction in the artifactual signal level due to synchronization, provided the data acquisition occurs in diastole. Using a relaxation delay of 1.0 s and a cat with a heart-rate of 85-100 beats/minute, synchronization marginally increases the imaging time from 6 minutes to 7-9 minutes. A further reduction in the artifactual signal level can be gained by synchronizing and gating the data acquisition. Unfortunately, the imaging time is increased drastically to a typical value of 30 minutes for the same relaxation delay and heart-rate as above with the cat breathing on its own. This imaging time may be reduced by ventilating the animal, thereby exploiting a controllable breathing pattern. The fact that a significant level of artifactual signal remains despite

synchronization and gating suggests that this residual artifactual signal is not caused by motion in the thoracic region of the cat.

5.5 Additional Causes of the Residual Image Artifacts

Despite synchronization and gating of data collection during animal imaging experiments, images from these experiments still contain some artifactual signal in the phase-encoding direction. Two factors present during these experiments have been identified as contributing to this residual noise: imperfections in the 180° RF pulse and the variation in cardiac period during an imaging experiment.

5.5.1 Imperfect 180° RF Pulses

Consider the effect of imperfect 180° RF pulses. In the ideal situation, transverse magnetization is created only by the selective 90° RF pulses. Non-selective 180° RF pulses have two effects: 1) they refocus spins within the slice to form the echo signal and 2) spins outside the selected slice are tipped from the +z axis to the -z axis or vice versa, and therefore do not contribute to the detected signal. If the strength of the $\mathbf{B}_1$ field is not uniform over the volume occupied by the subject or the 180° pulse is miss-set, then the train of 180° RF pulses will generate transverse magnetization outside the selected slice. This out-of-slice transverse magnetization will contribute to the detected signal, leading to artifactual signal in the final image.

To demonstrate the effect of imperfect 180° RF pulses, the following experiments were conducted. Two eight-echo unsynchronized and ungated imaging experiments of a cat were performed. A transverse slice, intersecting the heart, was selected. The relaxation delay was chosen to be 1.0 s and two averages of each projection were collected. In the first experiment, the pulse shape modulator gain was set to produce a 90° selective excitation pulse. Figures 5.11A and 5.11B show the first- and second-echo images

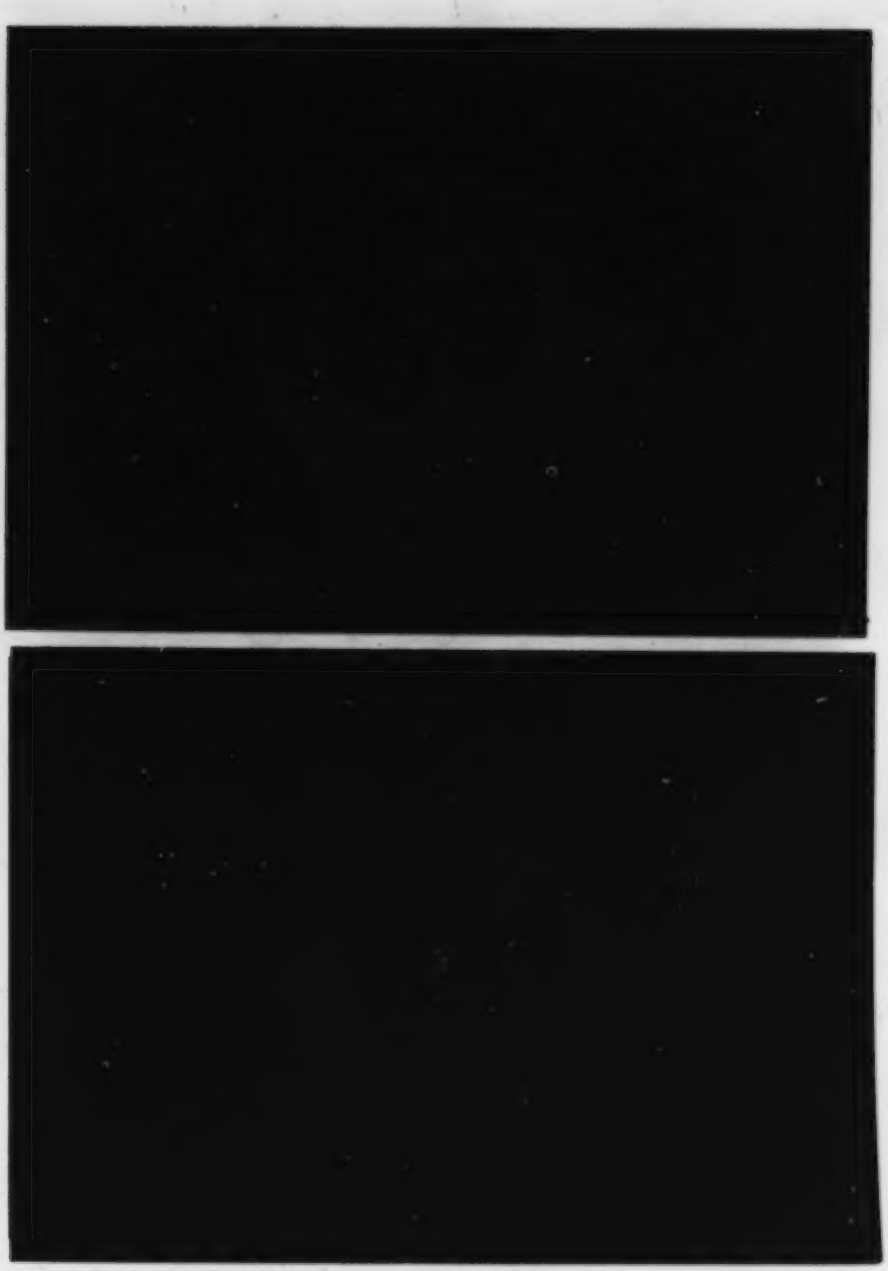

A

B

Figure 5.11 Unsynchronized transverse images of a cat at the anatomical level of the heart. These images were obtained with a 90° selective excitation pulse. A) first-echo image, B) second-echo image.

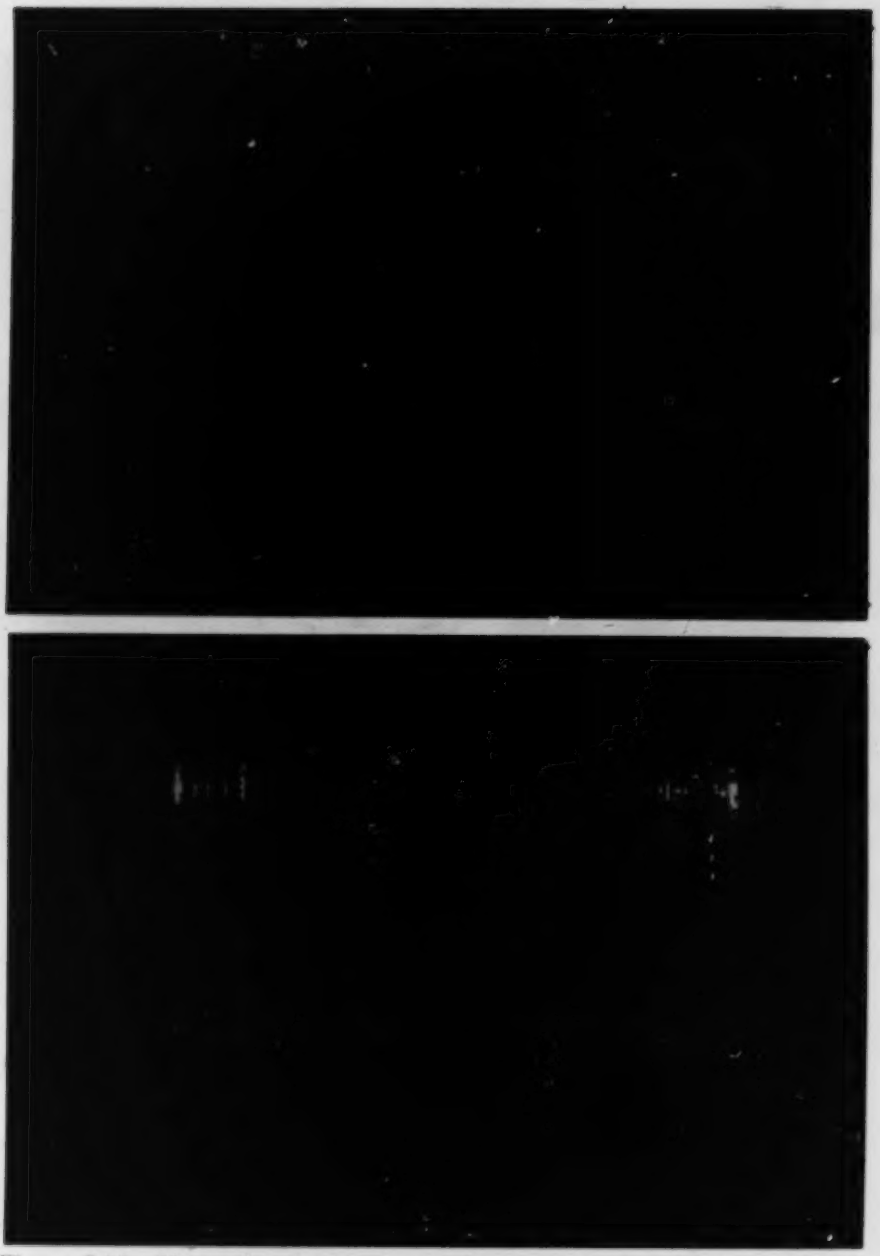

C

D

Figure 5.11 Unsynchronized transverse images of a cat at the anatomical level of the heart. These images were obtained with no selective excitation pulse. C) first-echo image, D) second-echo image.

resulting from this experiment. In the second-echo image, note the artifactual signal in the phase encoding direction. Similar artifacts are present in the other higher-order images of this experiment. The second imaging experiment was conducted with the pulse-shape modulator gain and offset control set to zero, effectively removing the 90° selective excitation pulse from the imaging pulse sequence. The first- and second-echo images from the second experiment are shown in Figs. 5.11C and 5.11D. Notice that, in these images, there is a broad band of artifactual signal in the phase-encoding direction. Furthermore, this band is more uniformly distributed in the first-echo image than in the second- and other higher-order images. The pattern of these artifacts in the higher-echo images of the second (0° excitation pulse) experiment is similar to the artifacts seen in the higher-echo images of the first (90° excitation pulse) experiment.

In order to quantify the intensity of the artifacts due to imperfect 180° RF pulses, the average background-noise and artifactual-noise levels were estimated for all the echoes of the 90° and 0° excitation pulse image sets. These results are displayed in Fig.5.12. The artifactual signal in the images of the first experiment is thought to be a result of physiological motion in the thoracic region of the cat, imperfect 180° RF pulses, and perhaps other factors. In the second experiment images, the artifactual signal band is due solely to imperfections in the 180° RF pulses, since the absence of the selective excitation pulse should have resulted in no transverse magnetization if the 180° pulses were perfect. The presence of the band of artifactual signal in these images suggests imperfections in the 180° RF pulses. Inspection of the results of Fig.5.12 indicates that the artifactual signal in both these image sets declines slowly with echo number. The average background-noise level in any echo of the 0° excitation pulse set was 1 - 15% lower than the background-noise of the corresponding echo of the normal set. Interestingly, there was only a 5 - 23% decline in the artifactual-signal level in any echo of the 0° excitation pulse set compared to

the artifactual-signal level in the same echo of the normal set. Therefore, a large component of the artifactual signal is due to imperfections in the 180° RF pulses.

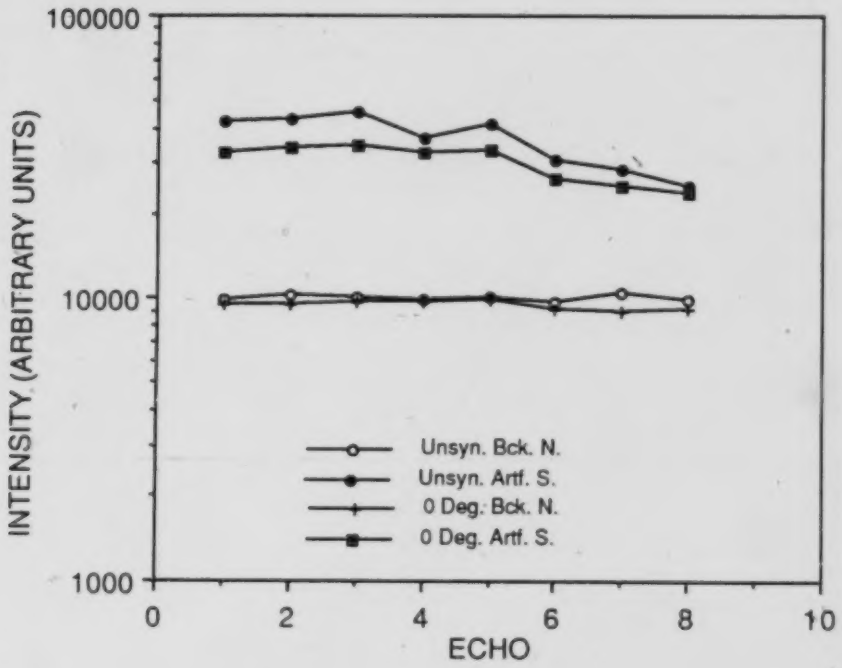

Figure 5.12 Average background and artifactual signal intensities of two sets of cat images at the level of the heart. One image (90°) is a normal image, the other (0°) was acquired using a pulse sequence with the 90° excitation pulse absent.

5.5.2 Variable Cardiac Period

The effect of a variable cardiac period is examined next. If the transverse magnetization distribution m(x,y) within the selected slice is identical for all projections of an imaging experiment, then the raw-data matrix may be written as:

$$s(\omega_X,\omega_Y) = \int\int m(x,y)\, \exp[-i(\omega_X x + \omega_Y y)]\, dxdy. \qquad (5.6)$$

In previous chapters, the effect of longitudinal relaxation was ignored. However, if T_1 relaxation is taken into account, and it is assumed that the repetition time t_r is fixed, then m(x,y) can be reduced to the form

$$m(x,y) = [\ 1 - \exp(-t_r/T_1)]\ m_0(x,y), \tag{5.7}$$

where $m_0(x,y)$ is the transverse magnetization distribution that would result from complete longitudinal relaxation prior to each projection. In synchronized imaging, the repetition time is constrained to be a multiple of the cardiac period. If the period of the cardiac waveform is constant throughout an imaging experiment, then the t_r during this experiment remains fixed, and m(x,y) is independent of time. However, if the cardiac period is variable during an imaging experiment, then t_r is also variable, leading to a time-dependent m(x,y)

$$m(x,y,\hat{t}\ ) = \{1 - \exp [- t_r(\ \hat{t}\ )/ T_1]\}\ m_0(x,y), \tag{5.8}$$

where $\hat{t}$ is the global time variable. Note that if the imaging experiment is set up so that the phase gradient monotonically increases (or decreases) as the experiment progresses, then there is an approximately linear relationship between $\hat{t}$ and ω_Y. Then m(x,y) can be written as

$$m(x,y,\omega_Y) = g(\omega_Y)\ m_0(x,y), \tag{5.9}$$

where

$$g(\omega_Y) = 1 - \exp [- t_r(\omega_Y)/ T_1].$$

Substituting the above expression for the transverse magnetization distribution into the expression for the raw-data matrix gives

$$s(\omega_X,\omega_Y) = g(\omega_Y) \int\int m_0(x,y)\, \exp[-i(\omega_X x + \omega_Y y)]\, dxdy. \tag{5.10}$$

The image matrix $\hat{m}(x,y)$ obtained by inverse Fourier transforming $s(\omega_X,\omega_Y)$ yields

$$\hat{m}(x,y) = F^{-1}[\, g(\omega_Y)\,] * m_0(x,y). \tag{5.11}$$

Note that if $g(\omega_Y)$ is a periodic function, then the convolution in equation 5.11 causes $m_0(x,y)$ to be replicated in the phase-encoding direction . The spacing between these ghosts is equal to the reciprocal of the period of $g(\omega_Y)$. Alternatively, if $g(\omega_Y)$ is not a periodic function, then the final image consists of $m_0(x,y)$ streaked in the phase-encoding direction.

In synchronized imaging, the duration between an ECG trigger pulse and the start of a pulse sequence (ECG delay) is fixed. If the cardiac period is variable, the configuration of the heart will be slightly different at the start of each projection. Since the shape of the heart directly influences the transverse magnetization distribution, m(x,y) becomes time dependent, and it has already been shown that a time-dependent m(x,y) leads to either ghosting or streaking.

A simple experiment was conducted to verify the effect of ghosting or streaking due to a variable t_r. Two eight-echo images of the flow phantom (no flow) were acquired. In the first experiment, the relaxation delay was fixed at 0.5 s and two averages of each projection were acquired. The first-echo image from this experiment is displayed in Fig. 5.14A. Note the lack of ghosting. For the second experiment, the pulse program was set up to perform synchronized imaging. The trigger signal originated from a signal generator which was set up to produce a pulse train (10 ms pulses) whose frequency was swept from 0.4 Hz to 4.0 Hz in approximately 105 s. The relaxation delay was kept at 0.5 s and two

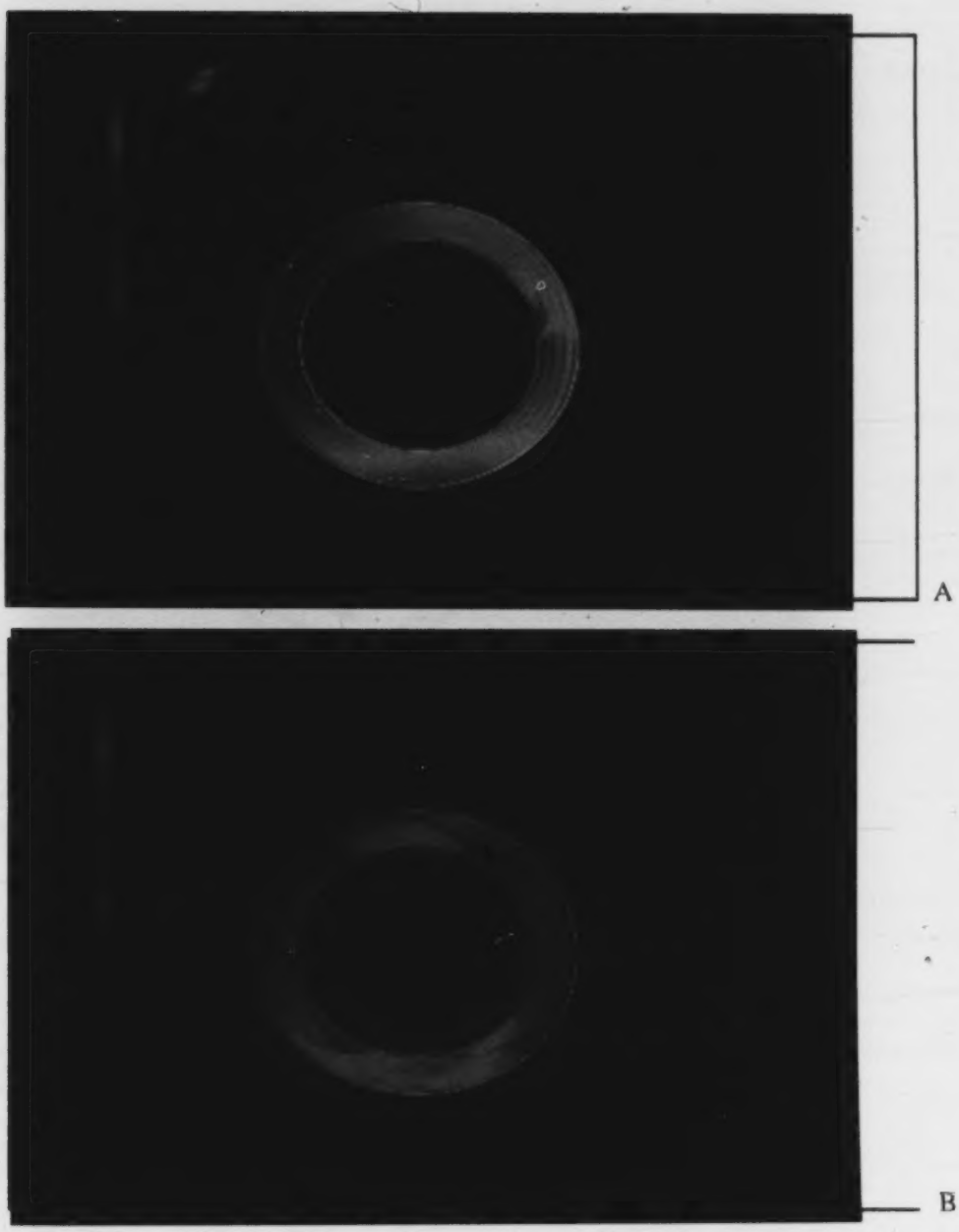

Figure 5.13 Transverse first-echo images of the flow phantom (no flow). A) obtained with the repetition time (t_r) fixed, and B) obtained with t_r varying as detailed in the text.

averages of each projection were collected. Figure 5.13B shows the first-echo image resulting from the second experiment. Note the extensive streaking artifacts. One method of reducing the effects of a variable t_r is to resort to long t_r images. If the t_r used is long enough to ensure complete longitudinal relaxation, then the effect of minor variations in this t_r is minimized.

CHAPTER 6
CONCLUSIONS

A project aimed at studying lung edema and clearance of fluid from the lungs using 2DFT NMR imaging is being evaluated at the University of Alberta in-vivo NMR facility. The presence of motion artifacts in thoracic 2DFT NMR images has hindered progress in certain areas of the project. It is therefore necessary to devise techniques that will minimize motion artifacts while not compromising the objectives of the project.

The principal objective of this thesis was to study motion artifacts due to pulsatile flow in 2DFT NMR images and to develop methods of minimizing these artifacts. In Chapter 3 a simple pulsatile flow model was considered, and the effect of this flow on 2DFT NMR images was evaluated. It was found that pulsatile flow in any direction led to ghosting artifacts. In addition, the images of mobile spins were both blurred and displaced in the direction of the flow when the pulsatile flow direction was parallel to the selected slice. However, no ghosting resulted when only steady flow was present, and blurring occurred for steady flow only in the read-encoding direction. Also, steadily flowing spins were displaced in the direction of the flow when the flow direction was in the selected slice. As expected, images were free of artifact when no flow was present.

Flow-phantom experiments (section 5.3) demonstrated that periodic pulsatile flow during unsynchronized imaging experiments leads to ghosting. Synchronization of the imaging pulse sequence to this periodic pulsatile flow makes it appear as steady flow (see section 3.3). Synchronization therefore effectively eliminates ghosting due to periodic pulsatile flow. However, in cats, the pulsatile blood-flow pattern encountered in the large thoracic blood vessels is not perfectly periodic. Consequently, unsynchronized animal images (section 5.4) show evidence of both ghosting and streaking due to pulsatile flow in

these vessels. Synchronization of the imaging pulse sequence can reduce the ghosting and streaking artifacts due to pulsatile blood flow in these large blood vessels. These streaking and ghosting artifacts are minimized when the NMR raw data is collected at the point of the cardiac cycle when the blood flow velocity in the large thoracic blood vessels is minimal.

A second type of artifact, less serious than ghosting, is the blurring of images of flowing spins in either the read- or phase-encoding direction due to periodic pulsatile flow in the corresponding direction. In addition to eliminating ghosts, synchronization removes all of the blurring due to periodic pulsatile flow in the phase-encoding direction and partially diminishes the blurring caused by similar flow in the read-encoding direction. The remaining read-direction blurring is due to the non-zero velocity of the blood in the read encoding direction during the NMR data acquisition period. This residual blurring can also be minimized by synchronizing the NMR data acquisition to a point in the cardiac cycle when the blood flow velocity in the large thoracic vessels is minimal.

Structures consisting of spins flowing in either the read- or phase-encoding directions are translated by $\hat{x}$ or $\hat{y}$, respectively (section 3.2.1). It was shown in Chapter 3 that $\hat{x}$ and $\hat{y}$ are proportional to the average flow velocity of the spins in the read and phase encoding directions, respectively. Furthermore, $\hat{x}$ is also proportional to the echo number (E). In the phantom experiments (section 5.3), the effect of the $\hat{y}$ displacement was not discernible in images obtained using the normal imaging pulse sequence. However, the effect of the $\hat{x}$ displacement was noticeable, especially in the later-echo images, even at flow velocities considerably lower than those found in the large thoracic blood vessels of cats. Fortunately, artifacts caused by the $\hat{x}$ and $\hat{y}$ displacement do not appear to be a serious problem in thoracic images of cats. Two factors contribute to this fortunate situation: firstly, the major blood vessels in the thoracic region of the cat do not run in the transverse direction for any significant length, and secondly, the high blood flow velocities

encountered in the large thoracic blood vessels results in turbulent blood flow which generally produces little or no signal in 2DFT NMR images. For synchronized imaging, $\hat{x}$ and $\hat{y}$ are proportional to the velocity of the moving spins during the pulse sequence of the imaging experiment. Therefore, synchronizing the NMR data acquisition period to a point in the cardiac cycle when the blood flow velocity in the large thoracic vessels is least will minimize the $\hat{x}$ and $\hat{y}$ translations.

Flowing spins produce ghosting, streaking, blurring and translation artifacts in 2DFT NMR images because gradient pulses impart upon these spins a phase different from that acquired by stationary spins. In principle, it is possible to design pulse sequences with special gradient pulses that serve to equalize the phase acquired by mobile and stationary spins (Joseph et al., 1987; Pattany et al., 1987). Use of such pulse sequences in NMR imaging should result in images with fewer artifacts. However, these schemes suffer from two principal drawbacks. Firstly, the inclusion of extra gradient pulses in these sequences results in a significantly longer echo time T_E. In quantitative pulmonary imaging, where lung tissue has a signal intensity that is lower and decays rapidly, long echo times would result in fewer useful images. Secondly, the amplitude and duration of these extra gradient pulses will have to be correctly adjusted so that no extra dephasing results from these gradient pulses; otherwise, the extra dephasing will compromise the accuracy of T_2 measurements.

The thoracic cat images presented in section 5.4 contain a broad band of low-intensity signal that overlies all the anatomical structures seen in these images. This low-intensity artifact serves to degrade the already poor signal-to-noise ratio (S/N) of lung tissue, thereby degrading the accuracy and precision of T_2 measurements obtained from these images. Furthermore, the intensity of this artifact decays slowly with time. Consequently, quantitative T_2 measurements of lung tissue may indicate the presence of a small slowly-

decaying component that is due to this artifact and not a genuine T_2 decay of lung-tissue signal.

It was assumed that physiological motion in the thoracic region of cats during the imaging procedure contributed to this low-intensity artifact. Cardiac synchronization of the NMR pulse sequence to diastole reduced the intensity of this artifact, as did respiratory gating of the NMR pulse sequence (section 5.4). It is expected that simultaneous respiratory gating and cardiac synchronization of the NMR pulse sequence to diastole will further minimize this low-intensity artifact. However, when an image acquisition is both cardiac synchronized and respiratory gated, the imaging time is increased drastically.

Experimental results presented in section 5.5 suggest that imperfect 180° RF pulses contribute significantly to the above low-intensity artifact. Further effort should be placed into identifying the cause (or causes) of the imperfect 180° RF pulses and, if feasible, rectifying this problem. Some factors that may contribute to imperfect 180° RF pulses include: an inhomogeneous $\mathbf{B}_1$ field in the volume occupied by the cat, drifting of the tuning frequency of the RF coil, arcing of the RF coil capacitors, and drooping of the RF amplifier output. Alternatively, one may attempt to remove the signal generated by the imperfect 180° RF pulses by using phase cycling or spoiler gradients (Barker & Mareci, 1989). Lastly, imaging pulse sequences that utilize optimal selective 180° RF pulses may prove advantageous.

In the final section of Chapter 5, it is shown that in cardiac synchronized NMR imaging a variable cardiac period led to a changing t_r during the imaging experiment. The resulting inconsistent degree of longitudinal relaxation between projections led to a time-dependent transverse magnetization distribution [$m(x,y,\hat{t})$], which in turn caused streak-like (or ghosting) artifacts in 2DFT NMR images. The severity of this artifact for typical imaging situations should be studied. A simple solution would be to increase the relaxation

delay such that full recovery of the longitudinal magnetization occurs prior to each projection. Alternatively, one could define an acceptable range of t_r values and keep track of the duration of time between the start of the preceding projection and the start of the current one. If a projection's raw data was acquired with a t_r within the acceptable range, the data is retained. Otherwise the projection is repeated until the acquired data are acceptable. However, both these schemes will increase the imaging time.

REFERENCES

Abragam A. Principles of Nuclear Magnetism. Clarendon Press, Oxford. **1961**

Abromowitz M and Stegun IA. Handbook of mathematical functions with formulas, graphs, and mathematical tables. Dover Publications Inc., New York. **1965**

Axel L. Blood flow effects in magnetic resonance imaging. Am J Roent **1984;** 143:1157-1166

Bailes DR, Gilderdale DJ, Byder GM, Collins AG, Firmin DN. Respiratory ordered phase encoding (ROPE): a method of reducing respiratory motion artefacts in MR imaging. Mag Res Img **1985;** 9:835-838

Barker GJ, Mareci TH. Suppression of artifacts in multiple-echo magnetic resonance. J Mag Res **1989;** 83:11-28

Damji AA, Snyder RE, Ellinger DC, Witkowski FX, Allen PS. RF interference suppression in a cardiac synchronization system operating in a high field NMR imaging system. Mag Res Img **1988;** 6:637-640

Dimick RN, Hedlund LW, Herfkens R, Fram EK, Utz J. Optimizing electrocardiograph placement for cardiac gated magnetic resonance imaging. Invest Radiol **1987;** 22:17-22

Edelstein W, Hutchinson J, Johnson G, Redpath T. Spin warp NMR imaging and applications to human whole-body imaging. Phys Med Biol **1980;** 25;751-756

Ehman RL, McNamara M, Pallack M,Hricak H, Higgins CB. Magnetic resonance imaging with respiratory gating: techniques and advantages. Am J Roent **1984;** 143:1175-1182

Farrar TC and Becker ED. Pulsed and Fourier Transform NMR: Introduction to Theory and Methods. Academic Press, New York. **1971**

Gradsteyn IS and Ryzhik IM. Table of Integrals, Series and Products. Academic Press, London. **1980**

Haacke EM, Patrick JL. Reducing motion artifacts in two-dimensional Fourier transform imaging. Mag Res Img **1986;** 4:359-376

Hawkes RC, Holland GN, Moore WS, Roebuck EL, Worthington BS. Nuclear magnetic resonance (NMR) tomography of the normal heart. J Comp Asst Tomgr **1981;** 5:605-612

Henkelman RM, Bronskill MJ. Artifacts in magnetic resonance imaging. Rev Mag Res Med **1987;** 1-126

Hinshaw WS, Andrew ER, Bottomley PA, Holland GN, Moore WS, Worhtington BS. Display of cross sectional anatomy by nuclear magnetic resonance imaging. Br J Radiol **1978;** 51:273-280

Hinshaw WS, Bottomley PA, Holland GN. Radiographic thin-section image of the human wrist by nuclear magnetic resonance. Nature **1977;** 270:722-723

Hoult D. The solution of the Bloch equations in the presence of a varying B_1 field - An approach to selective pulse analysis. J Mag Res **1979;** 35(1):69-86

Joseph PM, Shetty A, Bonaroti EA. A method for reducing motion induced errors in T_2 weighted magnetic resonance imaging. Med. Phys **1987;** 14(4):608-615

Knudsen SK. Fluid flow measurement using NMR imaging. MSc. Thesis : University of Alberta, Edmonton. **1987**

Kumar A, Welti D, Ernst RR. NMR Fourier zeugmatography. J Mag Res **1975;** 18:69-83.

Lanzer P, Botvinick EA, Schiller NB, Crooks LE, Arakawa M, Kaufman L, Davis PL, Herfkens R, Lipton MJ, Higgins CB. Cardiac imaging using gated magnetic resonance. Radiology **1984;** 150:121-127

Lauterbur PG. Image formation by induced local interactions: examples employing nuclear magnetic resonance. Nature **1973;** 242:190-191

Lewis CE, Prato FS, Drost DJ, Nicholson RL. Comparison of respiratory triggering and gating techniques for the removal of respiratory artifacts in MR imaging. Radiology **1986;** 160:803-810

Locher PR. Computer simulation of selective excitation in NMR imaging. Phil Trans R Soc Lond **1980;** 289:537-542

Mansfield P, Grannell PK. NMR 'diffraction" in solids? J Phys C: Solid State Phys **1973;** 6:L422-L426

Mansfield P, Maudsley AA, Morris PG, Pykett IL. Selective pulses in NMR imaging: A reply to criticism. J Mag Res **1979;** 33:261-274

Mansfield P, Morris PG. NMR Imaging in Biomedicine. Academic Press, London. **1982**

Mansfield P, Pykett IL, Morris PG, Coupland RE. Human whole body line-scan imaging by NMR. Br J Radiol **1978;** 51:921-922.

Meiboom S, Gill D, Modified spin echo method for measuring nuclear relaxation time. Rev Sci Instr **1958;** 29:688

Morris PG. Nuclear Magnetic Resonance in Medicine and Biology. Clarendon Press, Oxford. **1986**

Pattany PM, Phillips JL, Chiu LC, Lipcamon JD, Duerk JL, McNally JM, Mohapatra SN. Motion artifact suppression technique (MAST) for MR imaging. J Comput Asst Tomgr **1987;** 11(3) 369-377

Perman WH, Moran PR, Moran RA, Bernstein MA. Artifacts from pulsatile flow in MR imaging. J Compt Asst Tomgr **1986;** 10(3):473-483

Phillips D. The quantification and description of pulmonary edema with NMR imaging. MSc. Thesis: University of Alberta, Edmonton. **1987**

Runge VM, Wood ML. Fast imaging and other motion artifact reduction schemes: a pictorial overview. Mag Res Img **1988;** 6:595-608

Shultz CL, Alfidi RJ, Nelson AD, Kopiwaoda SY, Clampitt ME. The effect of motion on two-dimensional Fourier transformation magnetic resonance images. Radiology **1984;** 152:117-121

Slichter CP. Principles of Magnetic Resonance. Harper and Row, New York. **1963**

Sutherland RJ, Hutchinson J. Three dimensional NMR imaging using selective excitation. J Phys E: Sci Instr **1978;** 11:79-83

Van Dijk P. ECG triggered NMR Imaging of the heart. Diag Imag Clin Med **1984a;** 53:29-37

Van Dijk P. Direct Cardiac NMR imaging of heart wall and blood flow velocity. J Compt Asst Tomgr **1984b;** 8(3):429-436

Wood ML, Henkelman RM. MR image artifacts from periodic motion. Med Phys **1985;** 12(2):143-151

Wood ML, Henkeman RM. Suppression of respiratory motion artifacts in magnetic resonance imaging. Med Phys **1986a;** 6:794-805

Wood MJ, Henkelman RM. The magnetic field dependence of the breathing artifact. Mag Res Img **1986b;** 4:387-392

Zimmerman JR, Brittin WE. Nuclear magnetic resonance studies in multiple phase systems: lifetime of a water molecule in an adsorbing phase on silica gel. J Phys Chem **1957;** 61:1328-1333